Resonant laser ionization and mass spectrometry imaging for the study of geochemical interactions of actinides

---

Dissertation
zur Erlangung des akademischen Grades
"Doktor der Naturwissenschaften"

im Promotionsfach Chemie
am Fachbereich Chemie, Pharmazie, Geographie und Geowissenschaften
der Johannes Gutenberg-Universität
in Mainz

Felix Berg
geboren in Wiesbaden-Dotzheim

Mainz, den 3. September 2025

1. Gutachter: Prof. Tobias Reich

2. Gutachter: Prof. Klaus Wendt

Tag der mündlichen Prüfung: 31.10.2025

"Enjoy the three years of PhD:
These four years are going to be the best six of your life!"

- Note in an office at the University Medical Center Mainz

Contents

Abstract

Resonant laser ionization is a versatile analytical technique that is highly element selective and therefore in combination with mass spectrometry an excellent tool for the trace and ultra-trace analysis of radionuclides in the environment. Time-of-flight secondary ion mass spectrometry (TOF-SIMS) is a spatially resolved mass spectrometry imaging method for the investigation of surface compositions. But, as many other mass spectrometry techniques, it can be hampered by isobaric interferences. Therefore, by combining resonance ionization mass spectrometry (RIMS) with TOF-SIMS, a new spatially resolved, highly element selective technique is created, that addresses the shortcomings of either method. This technique is called resonant laser secondary neutral mass spectrometry (rL-SNMS). In this work, the combined approach of rL-SNMS and TOF-SIMS was developed and applied for the investigation of the (geo-)chemical behaviour of plutonium in the context of long-term nuclear waste disposal in a deep geological repository (DGR). This is documented in the first and second publication that are part of this dissertation. Due to the abundance and long half-life of the radioisotope ^{239}Pu in high-level waste from spent nuclear fuel, plutonium is of special interest for the safety case of a DGR. Therefore, it is the subject of laboratory studies that aim to investigate the chemical interactions with the barrier materials considered for a DGR and also yield parameters and constants that can be used to model the behaviour of plutonium. For the analysis of such experiments, the combined approach of TOF-SIMS and rL-SNMS can deliver new insights. In this thesis it was successfully demonstrated that it is possible to use TOF-SIMS and rL-SNMS for the observation of the diffusion of plutonium in Opalinus Clay, a potential host rock material for a DGR, and to model the resulting diffusion profile. At the same time, specific correlations and colocations with the elements of the host rock material were observed, hinting at the involvement of specific clay minerals in the retention of plutonium. This would not have been possible with abrasive peeling in combination with classical radioanalytical techniques, which is usually applied for the study of the migration of radionuclides. Furthermore, the time necessary to retrieve the diffusion profile was reduced. While it often takes multiple weeks to analyse the sanded samples via α- or γ-ray-spectroscopy, it was possible to already obtain the diffusion profile via TOF-SIMS and rL-SNMS in just a few days.

The other three publications included in this thesis focus on the investigation and development of the excitation schemes necessary for RIMS or rL-SNMS measurements. In the third publication, a newly published excitation scheme for plutonium was investigated. Here, previously unknown isotope shifts for the plutonium isotopes $^{238-240,244}$Pu were measured and the efficiency of this new scheme compared

to the established scheme usually applied in RIMS and rL-SNMS measurements in the Nuclear Chemistry. Here, no improvement was observed. However, based on this work it is now possible to apply the new scheme for measurements of the mentioned Pu isotopes and their ratios.

The fourth and fifth publication are documenting the development of novel excitation schemes for neptunium as well as their application in spectroscopic investigations. Due to its long half-life, the neptunium isotope ^{237}Np is of similar interest for the safety case of a DGR like ^{239}Pu. This collaborative effort with the LARISSA workgroup of the Institute of Physics of the Johannes Gutenberg-Universität Mainz was undertaken to develop more efficient excitation schemes for RIMS and rL-SNMS measurements of neptunium. These novel schemes are the basis for the translation of the migration studies conducted in this thesis with plutonium to neptunium. Furthermore, the ionization potential of neptunium was remeasured as well as the hyperfine structure and isotope shift of ^{237}Np and ^{239}Np investigated. This delivers new insights into fundamental nuclear properties of neptunium and makes it possible to test the use ^{239}Np as an isotopic spike for the quantification of ^{237}Np in RIMS measurements of environmental samples.

Zusammenfassung

Resonante Laserionisation ist eine vielseitig einsetzbare analytische Technik, die elementselektiv ist und aus diesem Grund in Verbindung mit Massenspektrometrie eine exzellente Methode für die Spuren- und Ultraspurenanalyse von Radionukliden in der Umwelt ist. Flugzeitsekundärionenmassenspektrometrie (engl. *time-of-flight secondary ion mass spectrometry*, TOF-SIMS) ist eine ortsaufgelöste Methode für bildgebende Massenspektrometrie für die Untersuchung der Zusammensetzung von Oberflächen. Jedoch, wie viele andere massenspektrometrische Methoden, kann sie durch isobare Interferenzen gestört werden. Durch die Kombination von Resonanzionisationsmassenspektrometrie (engl. *resonance ionization mass spectrometry*, RIMS) mit TOF-SIMS ergibt sich die Möglichkeit einer neuen, ortsaufgelösten und elementselektiven Technik, welche die Nachteile der jeweils anderen Methode behebt. Diese Technik heißt resonante Laser Sekundärneutralteilchenmassenspektrometrie (engl. *resonant laser secondary neutral mass spectrometry*, rL-SNMS). In dieser Arbeit wurde der kombinierte Ansatz von rL-SNMS und TOF-SIMS entwickelt und für die Untersuchung des (geo-)chemischen Verhaltens von Plutonium im Zusammenhang mit der Endlagerung von nuklearen Abfällen in einem tiefengeologischen Endlager verwendet. Aufgrund der Menge und der langen Halbwertszeit des Radioisotops ^{239}Pu in hochradioaktiven Abfällen aus abgebrannten Brennelementen ist Plutonium von besonderem Interesse für die Sicherheitsanalyse eines tiefengeologischen Endlagers. Daher ist es Gegenstand vieler Studien, die zum Ziel haben die chemischen Wechselwirkungen mit den geplanten Barrierenmaterialien für das Endlager im Labormaßstab zu untersuchen. In diesen Studien sollen ebenfalls Parameter und Konstanten gewonnen werden, mit denen das Verhalten von Plutonium im Endlager simuliert und für den Zeitraum von bis zu einer Million Jahre vorhergesagt werden kann. Bei der Analyse solcher Experimente kann der kombinierte Ansatz von TOF-SIMS und rL-SNMS neue Erkenntnisse liefern. Im Rahmen dieser Promotion wurde gezeigt, dass es mittels TOF-SIMS und rL-SNMS möglich ist, die Diffusion von Plutonium in Opalinus Tongestein, einem möglichen Wirtsgestein für ein tiefengeologisches Endlager, zu beobachten und darüber hinaus das Diffusionsprofil zu modellieren. Gleichzeitig wurden Korrelationen in der Intensität und Verteilung mit Elementen aus dem Wirtsgestein beobachtet, die auf die Beteiligung bestimmter Tonmineralien an der Rückhaltung von Plutonium hinweisen. Dies wäre mittels abrassiver Methoden und der Analyse der Schleifproben mit klassischen radioanalytischer Techniken, die häufig für die Untersuchung des Migrationsverhaltens von Radionukliden eingesetzt werden, nicht möglich gewesen. Des Weiteren wurde der Zeitaufwand um das Diffusionsprofil zu erhalten drastisch reduziert. Während die Analyse der Schleifproben mittels α- or γ-Spektroskopie

oftmals Wochen in Anspruch nimmt, konnte das Diffusionsprofil mittels TOF-SIMS und rL-SNMS in wenigen Tagen erhalten werden.

Die anderen in dieser Dissertation enthaltenen drei Publikationen fokussieren sich auf die Untersuchung und die Entwicklung der für RIMS und rL-SNMS notwendigen Anregungsschemata. Im Rahmen der dritten Publikation wurde ein neu veröffentlichtes Anregungsschema für Plutonium untersucht. Hier wurden die noch unbekannten Isotopieverschiebungen für die Plutoniumisotope $^{238-240,244}$Pu vermessen und die Effizienz des neuen Schemas zu dem in der Kernchemie etablierten Schema verglichen. Es konnte dabei keine verbesserte Effizienz festgestellt werden. Basierend auf dieser Arbeit ist es nun dennoch möglich das neue Schema für Messungen der genannten Plutoniumisotope und ihrer Verhältnisse zu verwenden.

Die vierte und fünfte Publikation dokumentieren die Entwicklung neuer Anregungsschemata für Neptunium und deren Anwendung in spektroskopischen Untersuchungen. Aufgrund seiner langen Halbwertszeit ist das Neptuniumisotop ^{237}Np von ähnlichem Interesse für die Sicherheitsanalyse eines tiefengeologischen Endlagers wie ^{239}Pu. In einer Zusammenarbeit mit der LARISSA Arbeitsgruppe aus dem Institut für Physik der Johannes Gutenberg-Universität Mainz wurden Anstrengungen unternommen effizientere Anregungsschemata für RIMS und rL-SNMS Messungen an Neptunium zu entwickeln. Diese neuen Anregungsschemata bilden die Grundlage dafür die in dieser Dissertation erfolgten Untersuchungen zur Migration von Plutonium auf Neptunium zu übertragen. Des Weiteren wurde das Ionisationspotential von Neptunium neu vermessen und sowohl die Hyperfeinstrukturen als auch die Isotopieverschiebung von ^{237}Np und ^{239}Np untersucht. Dies liefert neue Einblicke in die fundamentalen Eigenschaften des Neptuniumkerns und erlaubt es außerdem in Zukunft den Einsatz von ^{239}Np als internen Standard in RIMS Messungen zur Quantifizierung von ^{237}Np in Umweltproben zu testen.

Included manuscripts

The following five publications are the basis for the thesis presented here.

- Daniela Schönenbach, Felix Berg, Markus Breckheimer, Daniel Hagenlocher, Pascal Schönberg, Raphael Haas, Samer Amayri, Tobias Reich, Development, characterization, and first application of a resonant laser secondary neutral mass spectrometry setup for the research of plutonium in the context of long-term nuclear waste storage. Analytical and Bioanalytical Chemistry, 413, 3987–3997 (2021). https://doi.org/10.1007/s00216-021-03350-3

- Felix Berg, Christopher Sirleaf, Janik Lohmann, Markus Breckheimer, Tobias Reich, Investigation of plutonium diffusion profiles in Opalinus Clay rock via TOF-SIMS and rL-SNMS. Applied Geochemistry, Volume 183, 106332 (2025). https://doi.org/10.1016/j.apgeochem.2025.106332

- Felix Berg, Tobias Reich, Investigating a novel three-step excitation scheme for the ultra-trace analysis of plutonium via RIMS. Analytical and Bioanalytical Chemistry, (2025). https://doi.org/10.1007/s00216-025-06062-0

- Magdalena Kaja, Dominik Studer, Felix Berg, Sebastian Berndt, Christoph E. Düllmann, Nina Kneip, Tobias Reich, Mitzi Urquiza-González, Klaus Wendt, Resonant laser ionization of neptunium: investigation on excitation schemes and the first ionization potential. The European Physical Journal D, 78, 50 (2024). https://doi.org/10.1140/epjd/s10053-024-00833-7

- Magdalena Kaja, Mitzi Urquiza-González, Felix Berg, Tobias Reich, Matou Stemmler, Dominik Studer, Felix Weber, Klaus Wendt. High-resolution laser spectroscopy on the hyperfine structure and isotope shift of Np. The European Physical Journal A, 60, 140 (2024). https://doi.org/10.1140/epja/s10050-024-01362-y

Introduction and Motivation

1.1 Long-term nuclear waste storage

The management and disposal of radioactive waste and spent nuclear fuel is a major challenge for every country with a nuclear program. The current consensus is the final disposal of radioactive waste in deep geological repositories (DGR). The Spent Fuel and Radioactive Waster Information System (SRIS) by the International Atomic Energy Agency lists a total of 4 004 306 m^3 of radioactive waste and 104 382 t of heavy metals in spent nuclear fuel (SNF) globally [1]. However, this list is incomplete and does not include data from all IAEA members, so the real amount is expected to be higher. Furthermore, with many countries and private companies investing heavily into nuclear power and the design of novel reactor types, such as small modular reactors, these numbers are only expected to rise [2]. At the moment, 416 nuclear power reactors are in operation with an additional 62 units under construction worldwide [3].

The situation in Germany differs in this point from many other countries. With the exit from nuclear power and the shutdown of the last nuclear power reactors in April 2023 [4], the total amount of radioactive waste and spent nuclear fuel at least from nuclear power will not increase in the future. Current estimates predict a total of 10 500 t of heavy metals from spent nuclear fuel with a total volume of 27 000 m^3 for Germany that will need to be stored safely for one million years as high-level waste (HLW). Additionally, 300 000 m^3 from low- and intermediate-level waste are expected [5]. However, the latter number is estimated to double due to the dismantling of the former repository site Asse II and waste from uranium enrichment. A report from 2023 states, that the only DGR currently under construction, the "Schacht Konrad", with a total capacity of 303 000 m^3 for low- and intermediate-level waste, is supposed to be completed at the end of 2029 [6].

With the reform of the 2013 repository site selection act in 2017, German regulators decided on restarting the search for a long-term DGR for the final disposal of HLW in Germany [7]. While the act calls for the start of operation of a repository site by 2031, a recent external study predicts the beginning of disposal of HLW to start as late as 2074 [8].

One major challenge for the German search for a suitable site of a DGR for high-level waste is that Germany has access to all three types of host rock material that are considered suitable: argillaceous, salt or crystalline rock Figure 1.1 shows a photograph of the three rock types.

Figure 1.1: Examples for the three host rock systems considered suitable for long-term nuclear waste storage: argillaceous, salt and crystalline rock (left to right).

Many points need to be considered for the evaluation of each material, ranging from the engineering requirements to build a DGR inside this host rock to the fundamental geochemical interactions of the various radioactive elements. Since it is not possible to conduct experiments at the timescale of the one million years of safekeeping mandated, it is necessary to study the processes involved in the laboratory within a comparable short time frame and retrieve parameters that can then be used to model and predict the behaviour of the radioactive inventory. The German site selection act mandates to find the "the best possible site" for a DGR [7]. Consequently, it is also necessary to have the best and most detailed understanding of the underlying (geo-)chemical interactions of the radioactive inventory with the (geo-)technical and geological barriers that make up the multi-barrier system preventing the release of the radioactive inventory into the environment. Since these barrier materials are supposed to prevent the release of radioisotopes into the biosphere and protect its species from harm, the study of their migration and retention is of significant importance. Experiments designed to address these processes are studying for example transport mechanisms such as diffusion, but also sorption or the stoicheometry and formation of complexes with ligands that might alter the migration behaviour of radionuclides. To analyze and to evaluate samples from these experiments in order to gain further insights into the underlying physical and chemical processes, requires sensitive and precise analytical methods.

The actinides plutonium (Pu) and neptunium (Np) play a major role in the safety case of a DGR. Pu is of major interest due to its complex aqueous chemistry and its abundance in SNF. The amount of Pu produced in a power reactor varies with the reactor type and the burnup factor. As a rough estimate a 1 GW electric power light water reactor produces around 300 kg of Pu as SNF per year [9]. The isotope ^{239}Pu ($t_{1/2} = 24\,110$ a), which is present in significant amounts in SNF, will be responsible for most of the radioactive inventory of a DGR for around 2×10^5 a after the decay of the fission products after 1000 a. For Np, the isotope ^{237}Np is the most relevant for the final disposal of SNF. It is also generated as part of the nuclear fuel cycle and the amount produced depends on the reactor type and burnup. As an estimate, around 3 kg of ^{237}Np are produced per year per 1 GW thermal power

[10]. With a half-life of 2.14×10^6 a it will become the main contributor to the radioactive inventory of the DGR after the decay of ^{239}Pu and the total inventory of the disposal site will actually increase in the beginning due to the decay of ^{241}Am that is produced from ^{239}Pu during operation of a nuclear reactor. Due to their long half-life and resulting low specific activity, classical radioanalytical techniques, such as α- or γ-ray-spectroscopy, are not able to detect ^{239}Pu and ^{237}Np in the small amounts expected in the far-field of a DGR. Therefore, other analytical techniques, that do not rely on the radioactive properties, for example inductively coupled plasma mass spectrometry (ICP-MS), thermal ionization mass spectrometry (TIMS) or accelerator mass spectrometry (AMS), are used. However, these mass spectrometry methods can be hampered by isobaric interferences and do not offer spatial resolution, which is of great interest for the study of the geochemical interactions of radionuclides with heterogeneous materials present in a DGR. By investigating which components of the barrier systems are directly responsible for immobilizing the radionuclides in situ at the micro-meter scale, the knowledge of the underlying chemical and physical processes could be extended. Such studies would therefore directly contribute to making an informed decision on the "best possible" DGR.

In the thesis presented here, the spatially resolved analytical techniques time-of-flight secondary ion mass spectrometry (TOF-SIMS) and resonant laser secondary neutral mass spectrometry (rL-SNMS) were developed and applied for the study of (geo-)chemical interactions of Pu with materials relevant in a future DGR (publication I and II). Furthermore, efforts were made to improve resonance ionization mass spectrometry (RIMS) and rL-SNMS measurements by investigating a novel excitation scheme for Pu (publication III). Additionally, by contributing to the development and investigation of new two-step excitations schemes for Np (publication IV and V) the basis for transferring the results for Pu to Np was created.

1.2 Trace and ultra-trace analysis via resonance ionization

Resonance ionization (RI) is a highly sensitive analytical technique that is element selective. The principle of RI is to excite and subsequently photoionize an analyte using laser light tuned to specific electronic transitions of said analyte. The process is illustrated in figure 1.2a. Due to the unique electronic structure of every element, this results in highly efficient suppression of background and isobaric interferences, making RI a great tool for the trace and ultra-trace analysis of elements for both detection and quantification. As stated above, this is especially of interest for the long-lived radioisotopes in the context of a DGR, such as Pu and Np, since classical radioanalytical techniques such as α- or γ-ray-spectroscopy are not able to detect them in small amounts due to the low specific activity. To detect the generated photoions, RI is often paired with mass spectrometry. This combination is called resonance ionization mass spectrometry (RIMS). In case RI is used as post-ionization technique together with time-of-flight secondary ion mass spectrometry (TOF-SIMS), the term resonant laser secondary neutral mass spectrometry (rL-SNMS) has been established. The benefit of using a mass spectrometer as detector is that it allows for the detection of multiple isotopes of the same element since it separates the photoions according to their mass-to-charge ratio (m/Z). Figure 1.2b shows a schematic for the selectivity of RIMS.

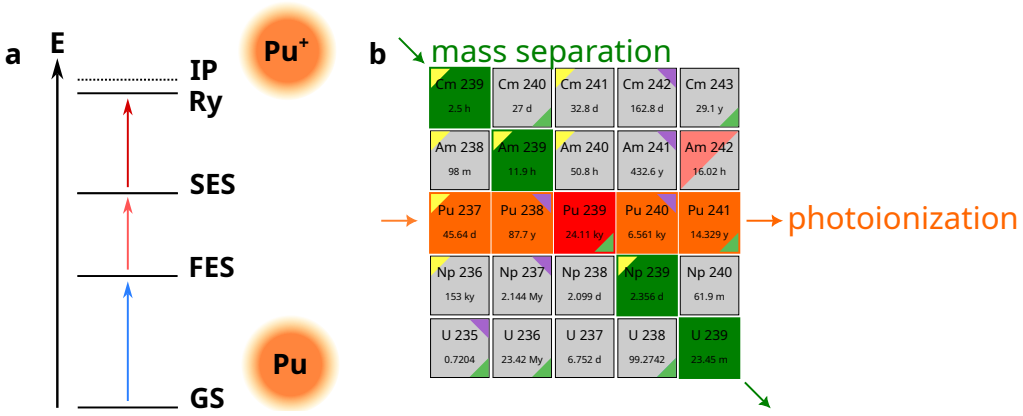

Figure 1.2: (**a**) Illustration of a three-step excitation process for resonance ionization. The electron is excited from the ground state (GS) to the first excited state (FES), to the second excited state (SES) into a Rydberg state (Ry) just below the ionization potential (IP). From there the ionization takes place via an external electric field, collision or black-body radiation. This type of excitation scheme were used in the publications I, II and III. (**b**) Excerpt of the nuclide chart demonstrating the selectivity of the combined approach of resonance ionization (RI) and mass spectrometry (MS).

An important component of using RIMS for the detection of an analyte is the development and characterization of an excitation scheme. They are developed

on the basis of spectroscopic studies that identify suitable electronic levels and transitions in an element. As shown in figure 1.3, which gives an overview of the current amount of laser spectroscopic studies conducted on radioisotopes, such data is readily available and therefore it is possible to use RIMS for the detection and quantification of many radionuclides.

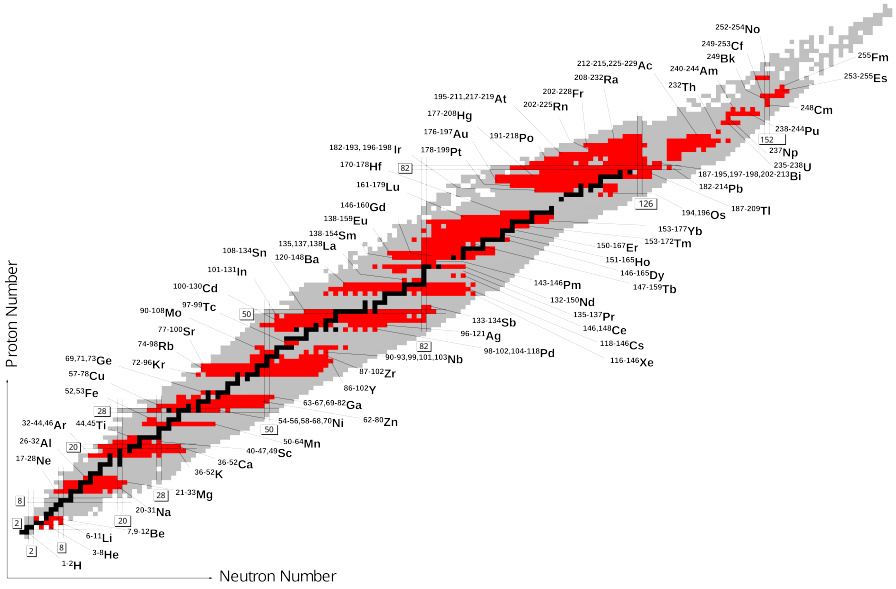

Figure 1.3: Overview of the current status of laser spectroscopic studies of radioactive isotopes. The graphic was taken from the online database of peer-reviewed spectroscopic studies of radioactive isotopes maintained by the group of Prof. W. Nörtershäuser from the TU Darmstadt. Stable isotopes are shown in black, radioactive isotopes in red. Graphic and references are available on the website of the database [11].

In publication I and II, that are investigating the use of rL-SNMS for the study of the geochemical interactions of Pu with materials of a DGR and were focused on the detection of a single Pu isotope, a well established and characterized excitation scheme by Grüning et al. [12] was used. This three-step scheme is also used in routine RIMS measurements of environmental samples from Rhineland-Palatinate for the quantification of ^{239}Pu and ^{240}Pu that are conducted annually in the Nuclear Chemistry and for which the author was responsible from 2019-2023. The absolute quantification via RIMS relies on a pure isotopic spike of known quantity, which is added to the sample and is then used as an internal standard for the other isotopes. The benefit of an isotopic spike is that it behaves just like the analytes during the necessary chemical separation and preparation of the sample as well as during the atomization in the source region of the measurement setup. Since this internal standard should not be present in the sample itself, for the quantification

of ^{239}Pu and ^{240}Pu in environmental samples the rare ^{244}Pu is used, since it was not part of the global nuclear fallout. Due to the atmospheric and exatmospheric tests of nuclear weapons in the 1940s-1960s, man-made Pu is now ubiquitous and the isotopes ^{239}Pu and ^{240}Pu can be found in trace amounts all over the world [13–15]. When measuring these isotopes and their ratios via RIMS or rL-SNMS, whether it is for quantification with the use of an isotopic spike or fingerprinting as part of a nuclear forensic investigation, it is of the utmost importance to ensure all isotopes are photoionized equally. This requires the identification and characterization of the so called optical isotope shift for the energy levels used in an excitation scheme for a certain element.

The isotope shift characterizes small differences in the energy of an atomic level between isotopes of the same element due to differences in mass of the nucleus (mass shift), as well as differences in the charge distribution inside the nucleus (field shift) resulting from the changing number of neutrons. For lighter elements, such as technetium, this difference is negligible compared to the linewidth of the laser light and the isotopes ^{97}Tc and ^{99}Tc can be measured at the same time [16]. For heavier elements, such as Pu and Np, the isotope shift can be multiple GHz and therefore the lasers need to be tuned to the exact resonance of each isotope during a measurement to ensure accurate results. The isotope shifts for the Pu excitation scheme by Grüning et al. are well known. However, for a novel excitation scheme for Pu by Galindo-Uribarri et al., only the resonance wavelengths for ^{242}Pu were reported [17]. In order to be able to apply this scheme for RIMS and rL-SNMS measurements of other Pu isotopes and to measure their isotope ratios accurately, the previously unknown isotope shifts for ^{238,239,240,244}Pu were quantified as part of the investigations reported in publication III. Figure 1.4 displays the big difference of almost 20 GHz between ^{238}Pu and ^{244}Pu observed for the second excitation step.

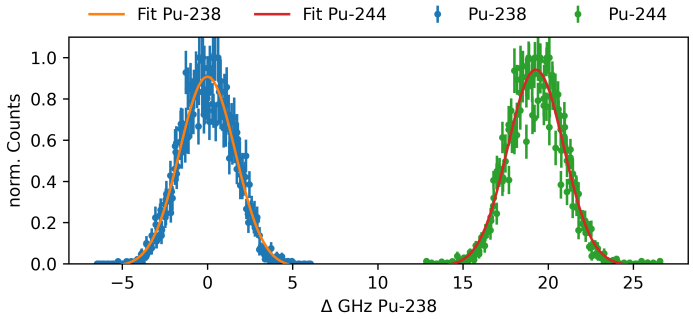

Figure 1.4: Isotope shift for the second excitation step between ^{238}Pu and ^{244}Pu for the scheme developed by Galindo-Uribarri et al. The data for this plot was taken from publication III [18].

That means that even if a laser with a linewidth of multiple GHz is used, it is not possible to pump this transition in both Pu isotopes equally at the same time. Therefore, it is required to adjust the laser wavelength for this excitation step, when

switching between the isotopes.

The results of publication III make it now possible to use the excitation scheme by Galindo-Uribarri et al. for RIMS and rL-SNMS measurements of more Pu isotopes as well as to measure their isotope ratios accurately.

In contrast to Pu, no isotopic spike is readily available for the quantification of ^{237}Np. Due to their half-lives, ^{235}Np or ^{236}Np would be suitable candidates. However, both need to be produced at accelerator facilities and in order to be obtained in sufficient purity, need either highly purified isotopic targets or subsequent extensive isotopic separation [19, 20]. In the course of the author's PhD, efforts were made to use ^{239}Np as an isotopic spike for quantification. ^{239}Np has only a half-life of 2.4 d, but can readily be produced by the irradiation of ^{238}U at the TRIGA research reactor of the Johannes-Gutenberg Universität Mainz and separated by anion exchange chromatography. The excitation scheme used was chosen based on the work of N. Stöbener, who developed with S. Raeder three-step excitation schemes for ^{237}Np [21] and characterized them on the RIMS setup in the Nuclear Chemistry in his thesis [22]. The necessary isotope shift measurements for ^{239}Np were conducted in a collaboration with [redacted] at the RISKIO mass separator of the LARISSA workgroup in the Institute of Physics of the Johannes Gutenberg-Universität Mainz and published as part of the master thesis of Benjamin Holz [23], whose practical work was instructed and supervised by the author. Figure 1.5 displays the results of these measurements.

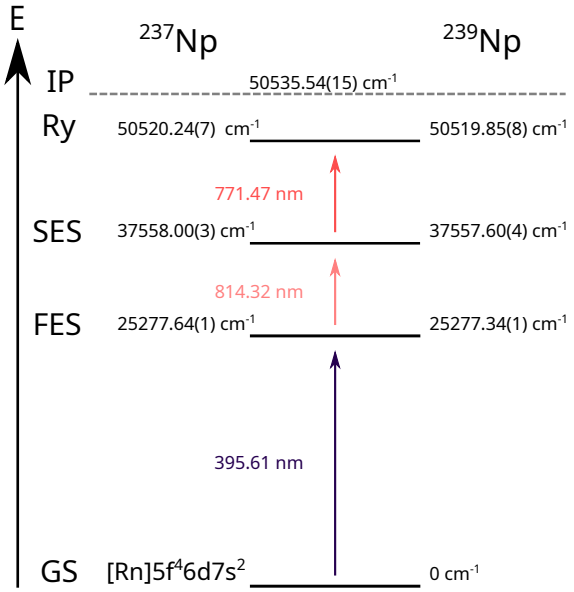

Figure 1.5: Measured resonances for ^{237}Np and ^{239}Np using the excitation scheme for the Np scheme previously investigated by Nils Stöbener [22]. Formal data analysis and visualization by the author of this thesis.

The three-step scheme was then applied to measure a mixed artificial sample of ^{237}Np and ^{239}Np in the RIMS setup of the Nuclear Chemistry.

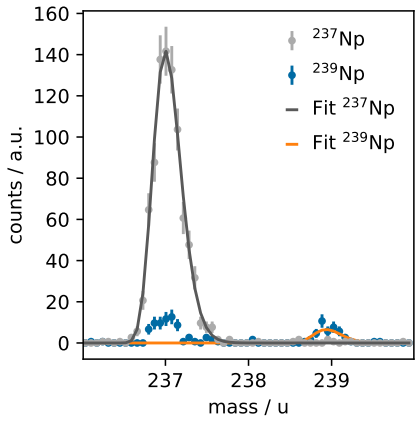

Figure 1.6: Excerpt of a mass spectrum of a mixed ^{237}Np and ^{239}Np sample measured at the RIMS setup at the Nuclear Chemistry using the wavelength and isotope shifts displayed in figure 1.5.

However, as evident in figure 1.6, the overall efficiency of the measurement was lacking and the amount of ^{239}Np detected insufficient to be used as a tracer for ^{237}Np with sufficient statistical reliability. The efficiency was roughly 1-2 orders of magnitude below measurements of Pu. It became clear that a new and more efficient excitation scheme was required for future attempts of the quantification of Np with an isotopic spike. These investigations were conducted in a collaborative effort with Magdalena Kaja from the LARISSA workgroup in the Institute of Physics of the Johannes Gutenberg-Universität Mainz. The results were published in publication IV and V. In publication IV, new two-step excitation schemes for ^{237}Np were developed. The investigations also revealed that the first excitation step used in the three-step scheme by N. Stöbener and displayed in figure 1.5 is inefficient in comparison with other possible transitions. Additionally, the ionization potential of Np was remeasured and the uncertainty of the literature value reduced by two orders of magnitude. For the development of the excitation schemes a special focus was put on the suppression of ^{239}Pu, the daughter of ^{239}Np, to allow accurate isotopic ratio measurements in case ^{239}Np is used as an isotopic spike. Publication V features high resolution spectroscopy of ^{237}Np and ^{239}Np using the novel two-step excitation schemes to measure the hyperfine structure of the first excited step of both isotopes as well as the isotope shift. Based on the results of publication IV and V, together with currently ongoing upgrade of the laser system in the Nuclear Chemistry, which will allow for the application of the novel two-step excitation schemes, the efforts to measure and quantify Np via RIMS and rL-SNMS can be continued in the future.

Another important characterization of an excitation scheme is it efficiency. However, as it was also demonstrated in the publication III for Pu, the efficiency of a RIMS measurement does not only depend on the excitation scheme alone, but on factors such as atomization efficiency of the type of source used, the shape of the

atom plume, the overall atom-photon interaction volume, laser power and the ionization process. Therefore, the overall efficiency of a RIMS measurement is highly setup specific and cannot necessarily be directly compared with others. That also means that the efficiency of the novel excitation schemes developed for Np in publication IV will also have to be tested on the RIMS and rL-SNMS setups in the Nuclear Chemistry and carefully evaluated once the upgrade of the laser system is finished.

1.3 Chemistry and migration behaviour of plutonium and neptunium in Opalinus Clay

Publication I documents the initial setup and development of the rL-SNMS in the Nuclear Chemistry for the study of Pu in the context of DGR materials. Based on this work, in publication II the application of the combined approach of TOF-SIMS and rL-SNMS for the study of the geochemical interactions and migration behaviour of Pu in Opalinus Clay (OPA) was investigated. The study of the migration processes of radionuclides through barrier materials is an important component for the safety case of a DGR. By observing and modelling the spreading of a radionuclide in a medium, it is possible to derive the necessary parameters to predict the propagation behaviour of the radioactive inventory of the DGR during its lifetime.

OPA is a type of clay rock that can be found in the Southern-German and Northern-Swiss Jurassic. It was formed as sediment approximately 1.5×10^8 a to 2×10^8 a ago. The name is derived from the species *Leioceras opalinum*, which can be found as fossil in large quantities in it. Nagra, the Swiss National Cooperative for the Disposal of Radioactive Waste, has proposed OPA as a host rock for the Swiss DGR [24]. In general, clay rock is one of the potential host rock systems that is considered suitable for a DGR for the final disposal of radioactive waste. Therefore, many countries are investigating various types of clay as well, for example: Boom Clay (Belgium), Queenston Formation Shale (Canada), Callovo-Oxfordian (France), Boda Claystone (Hungary), and Wakkanai (Japan) [25]. Favourable properties of clay rock are the large specific surface area, providing sorption sites for the retention of mobilized radionuclides, as well as the vast, but fine porous space. Furthermore, it is largely impermeable to water, providing a natural border for groundwater carrying layers above and below the clay rock, and it displays "self-healing" properties: Cracks and other damages, that would allow water to flow through and mobilize the radioactive inventory, are closed due to the swelling that clay rock displays if it gets in contact with said water [26]. This property derives from swelling clay minerals, such as smectite. Due to this low permeability, diffusion is considered the main transport mechanism for radionuclides, such as Pu and Np, through clay rock.

The OPA samples used in this work are from the Mont Terri Underground Rock Laboratory in Switzerland (URL, St-Ursanne, Switzerland). Figure 1.7 shows a

piece of OPA from which samples for this thesis were produced.

Figure 1.7: Piece of Opalinus Clay rock from the Mont Terri Underground Rock Laboratory used in publication II. From this piece small parts were sawed off and prepared for CNC milling to produce the diffusion cores.

Three main lithostratigraphic units of OPA from the URL can be distinguished: Shaly, sandy and carbonate-rich sandy facies. They originate from variations in the content of clay minerals, quartz and carbonates. However, the overall mineralogical variability of OPA in northern Switzerland is considered small: Typical clay mineral contents (kaolinite, illite, chlorite, smectite, siderite, pyrite) are in the realm of 60(15) %, carbonates approximately 20(15) % and quartz/feldspars circa 20(10) % [27]. The redox properties of the OPA host rock system are dominated by the Fe^{2+}/Fe^{3+} and ${SO_4}^{2-}/S^{2-}$ equilibrium originating from pyrite and siderite [28] with a partial pressure of CO_2 of around 6.31 mbar. Pore sizes of OPA are in the range of 1 nm to 100 nm [28].

In its natural state, OPA is saturated with OPA pore water (pw). Three types of pw can be distinguished: Free, outerlayer and interlayer pw [28]. Figure 1.8 shows a schematic of the pore space and the different types of pw inside OPA.

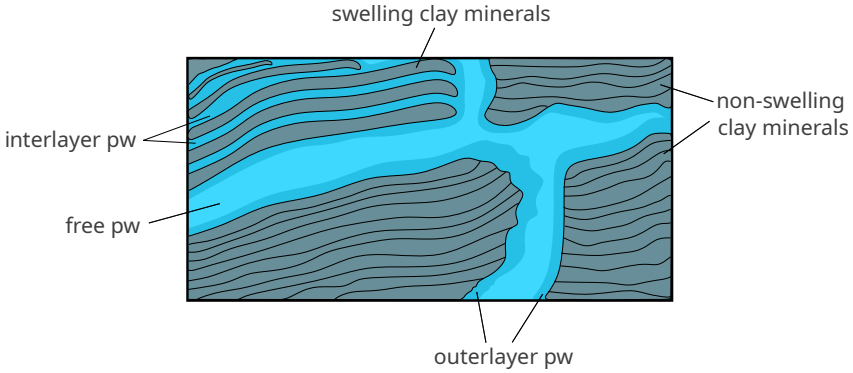

Figure 1.8: Schematic of the pore space filled with different types of pore water (pw): Interlayer pw in between swelling clay minerals and outerlayer pw (darker blue), as well as free pw (light blue).

As the name suggests, free pw is in the interparticle pore space and not or only weakly bound. Outerlayer pw shows less mobility and is bound to the surface of the clay minerals due to electrostatic interactions. Additional pw is present in the interlayer of swelling clay minerals such as illite and smectite. The pw composition and its pH have a major influence on the chemical speciation of the radioisotopes and therefore on their chemical interactions. This needs to be taken into account when designing an experiment.

For example, the initial oxidation state of the ^{242}Pu added to the diffusion experiment reservoir in the study presented in publication II was VI (PuO_2^{2+}), which was confirmed by UV-VIS measurements of the stock solution. However, measurements via capillary electrophoresis coupled to an inductively coupled plasma mass spectrometer (CE-ICP-MS) at the end of the experiment revealed, that Pu is present in the pw reservoir has actually the oxidation state V (PuO_2^{+}).

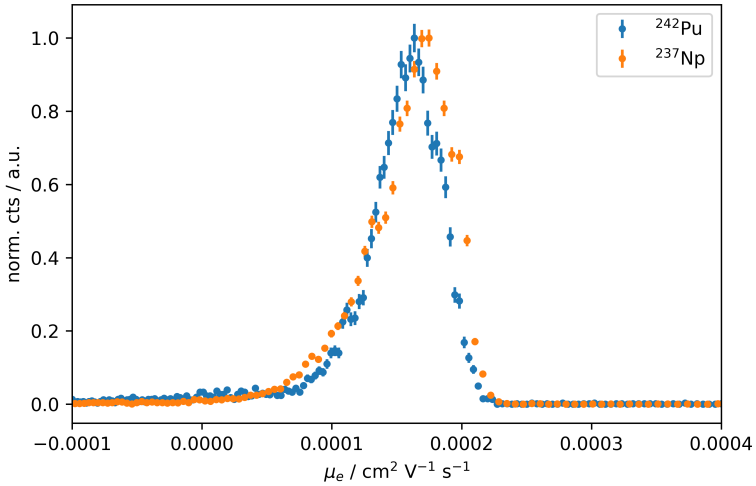

Figure 1.9: Electrophoretic mobility of Pu and Np in OPA pw at pH 7.5 measured by CE-ICP-MS. Since Np is stable as NpO_2^{+} under these conditions and both radioisotopes are showing the same mobility, it follows that Pu must be present as PuO_2^{+} in the OPA pw reservoir. The figure was taken from publication II [29].

Another important variable is the partial pressure of CO_2 in OPA as shown in the Pourbaix diagram of Pu in pw in figure 1.10. Under oxidizing conditions ($c(CO_2)$ = 420 ppm) at pH 7.5, $Pu(OH)_4$ and PuO_2^{+} are the dominating forms of Pu in solution. If the partial pressure of CO_2 is increased to 6.31 mbar as observed in the URL in Switzerland [30], CO_3^{2-} complexes of Pu with different solubility are to be expected. The experiments presented in publication II were conducted under atmospheric conditions as a proof of concept and due to the unavailability of anoxic OPA samples.

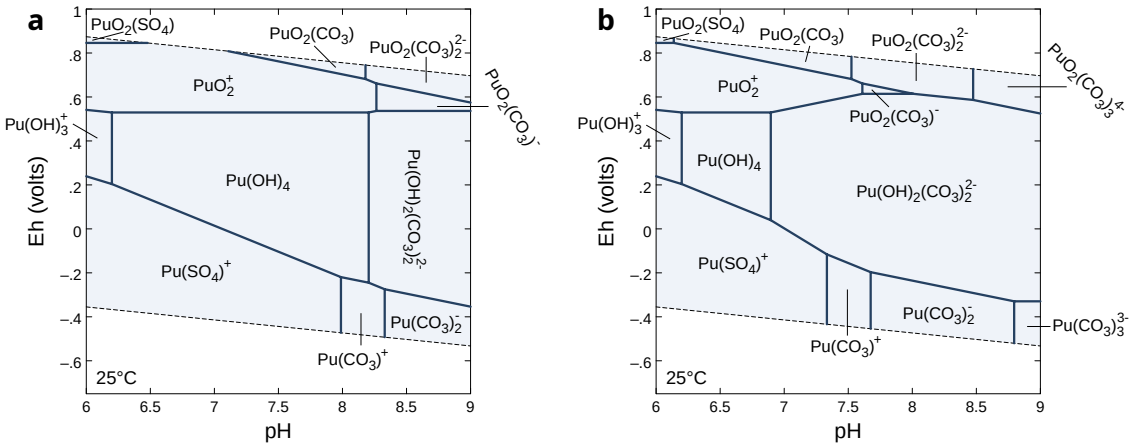

Figure 1.10: POURBAIX diagram of Pu in OPA pw for atmospheric CO_2 pressure (4.2×10^{-3} mbar) (**a**) and for the partial pressure of CO_2 expected in a DGR in OPA (6.31 mbar) (**b**). OPA pw composition after [31]. Calculated with Geochemist's Workbench© [32] and the ThermoChimie database v12a (SIT) [33].

The exact contents of OPA pw may vary depending on the facies found in a certain bore hole or a certain depth [30]. Nevertheless, a recipe for OPA pw from the URL has been established by Pearson et al. [31] and is widely applied in literature for laboratory experiments [34–37], including publication II. The pH value of this artificial OPA pw is adjusted to approximately pH 7.5 to match natural conditions.

As mentioned above, the transport mechanisms of actinides through porous media, such as OPA, is diffusion. It describes the movement of particles along a gradient from higher concentration to lower concentration. Due to the previously discussed self-healing properties of clays, other transport mechanisms such as advective transport are not of relevance for the migration of radioisotopes through OPA [38]. The diffusion takes place through the extensive connected porous space filled with the previously mentioned types of OPA pw.

The counter force of the migration of radionuclides through OPA via diffusion are sorption processes with the clay minerals. The two main mechanisms for sorption are cation exchange and surface complexation [38]. In addition, redox active minerals such as the Fe(II) containing pyrite can change the oxidation state of the radionuclide to a less soluble species and therefore cause retention by precipitation. For example, it has been shown in literature, that Pu(V) is reduced to Pu(IV), which has a decreased solubility, while diffusing deeper into OPA [39]. The same has been demonstrated for Np: During the diffusion process Np(V) is reduced to the less soluble species Np(IV) and here pyrite has been indicated as at least one of the redox-active minerals involved [40]. In the investigations presented in publication II, the distribution of Pu in the OPA diffusion samples was studied via TOF-SIMS and rL-SNMS. The subsequent analysis revealed the presence of "hot spots" of Pu on the sample surface and a colocation and correlation between Fe, Ca and Pu (compare figure 1.11). The colocation of these three elements indicates

the involvement of the mineral pyrite in the retention of Pu described in literature. Since pyrite is often present in OPA as sub-mm aggregates that are held together by a cementitious phase of calcite, this would explain the observed colocation of Fe and Ca in spots of increased Pu signal. Therefore, the findings in publication II are another indicator of the chemical interaction of Pu and pyrite.

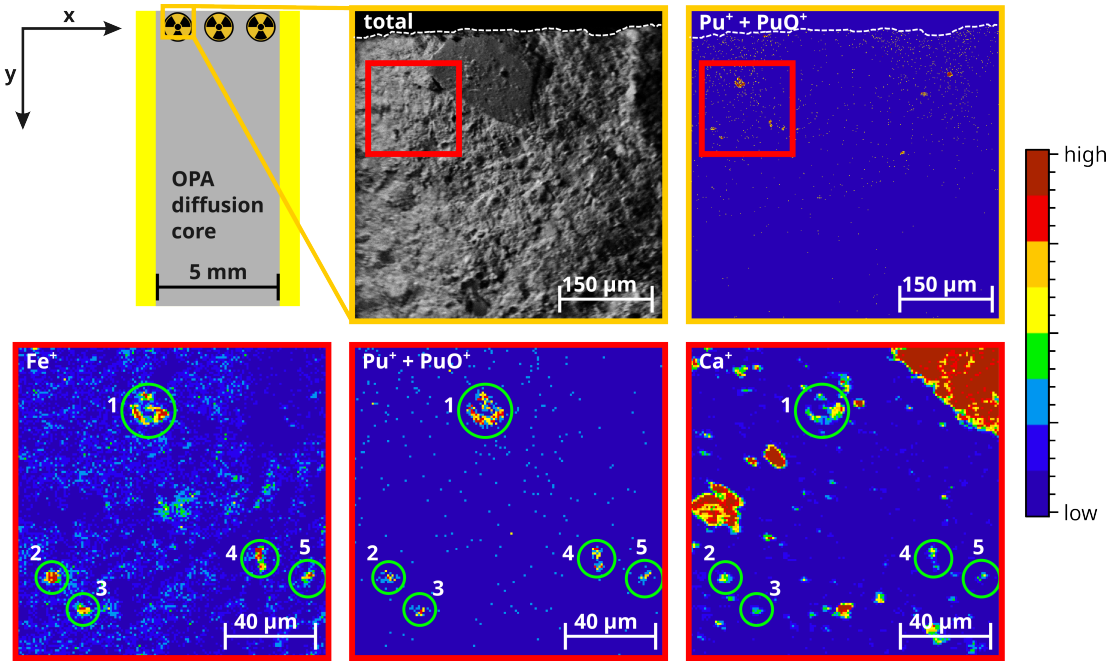

Figure 1.11: TOF-SIMS mappings of an excerpt of the border area of OPA Pu diffusion sample. Shown are the total ion signal, the sum of the Pu^+ and PuO^+ signal, as well as Fe^+ and Ca^+. In the red highlighted area 5 spots can be identified that show a colocation of Fe, Ca and Pu. This hints at a geochemical interaction of Pu and the clay mineral pyrite. The figure was taken from publication II [29].

Due to the negative charge of the clay minerals resulting from the replacement of higher with lower valency cations, e.g. replacement of Si^{4+} with Al^{3+} [38], the sorption and therefore diffusion behaviour of anionic, neutral and cationic species differ. Negatively charged species, such as TcO_4^- are repelled, whereas cationic species, such as NpO_2^+ or PuO_2^+, are attracted by the electrostatic forces. Additionally, the negative surface charge makes the process of surface complexation pH dependent. At a lower pH the negative surface charge of the clay minerals is reduced due to protonation. Therefore, less sorption sites for cationic radionuclides are available. Interestingly, the decreased sorption behaviour of anionic species does not necessarily lead to higher diffusion constants and faster migration compared to neutral species in OPA. A possible explanation is that due to the repellent electrostatic forces anions can not enter smaller pores and therefore have less migration pathways available [41]. Based on the interactions described above, it could be expected that cationic species show a reduced mobility compared to neutral species.

However, when normalized to the diffusion to neutral species such as HTO and the respective diffusion coefficient in bulk water, cationic species show an increased mobility [38]. This phenomenon can not be explained by a concentration gradient driven diffusion in the free pw. If this was the case, a higher mobility for the neutral species compared to the cations would be predicted, since the latter should sorb to the mineral surface. Since this is not the observed behaviour, the existence of a mobile surface species in addition to the species in the free pw has been suggested [38]. To support this, it has been demonstrated that the mobility of a species that interact with the surface by forming chemical complexes, rather than electrostatic interactions, is also highly dependent on the ionic strength of the background electrolyte. Here, a decrease in ionic strength of the electrolyte lead to an increase in diffusion depth [42]. To describe these observations, a model of surface diffusion in the electronic double layer (EDL), which is at the interface between free pw and the negatively charged clay mineral surfaces, has been suggested. Figure 1.12 shows a schematic for this model.

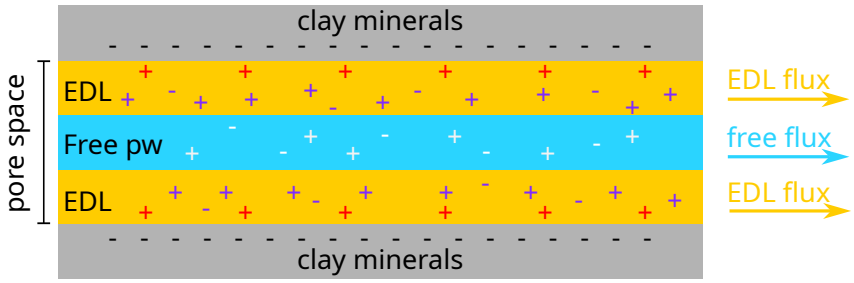

Figure 1.12: Schematic of the combined transport of cationic species in the free pw and the electronic double layer (EDL). Figure adapted from [38].

Accordingly to the model, two type of cations exist in the EDL: One is tightly sorbed to the surface of the negatively charged mineral clay, the other one is present in its vicinity and is still mobile. However, mathematical descriptions of this model are still under development.

Therefore, for the modelling of the diffusion profile of Pu in OPA observed in publication II, the simple description of the diffusion as a concentration gradient driven process was chosen. Mathematical expressions for this diffusion model can be derived from FICK's first or second law. In publication II, a mathematical expression derived by Yaroshchuck et al. [43] for filterless in-diffusion derived from FICK's second law was used. While this mathematical model does not account for processes such as surface driven diffusion, or the redox-activity of Pu, it was still possible to describe the diffusion profile with acceptable accuracy and an apparent diffusion coefficient D_a was retrieved. The resulting fit is displayed in figure 1.13.

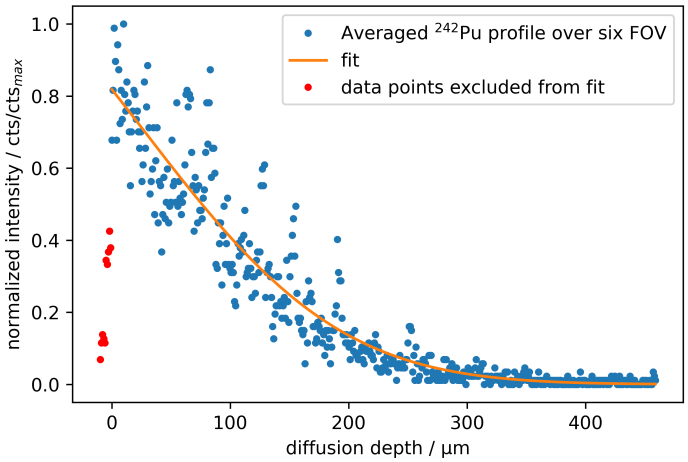

Figure 1.13: Diffusion profile of Pu in Opa obtained via TOF-SIMS. The diffusion time was 35 d. For the model a solution of FICK's second law derived by Yaroshchuck et al. [43] for filterless in-diffusion was used. The figure was taken from publication II [29].

In conclusion, the development of the joint approach of TOF-SIMS and rL-SNMS for the investigation of Pu in the context of a DGR, in combination with the method-tailored sample preparation and novel data analysis workflows presented in publication II, allowed for the study and modelling of Pu diffusion profiles in OPA while retaining the micro-structure of the sample. This is a clear advantage over the traditionally applied method of abrasive peeling, during which the sample is destroyed [34, 36]. Another significant advantage is the reduction of the analysis time of a diffusion profile. To obtain a diffusion profile via abrasive peeling, the sample needs to be sanded approximately 10 µm at a time and each sanding paper measured via classical radioanalytical technqiues. Assuming a diffusion depth of 300 µm and in case of radionuclides with low specific activity, such as ^{239}Pu or ^{237}Np, this can accumulate to total measurement times of multiple weeks. By using TOF-SIMS and rL-SNMS, the diffusion profile of a sample as it was used in publication II can be obtained within a single day. In combination with the newly developed highly automated analysis workflow, the profile can then be modelled and diffusion constants obtained almost instantly. Furthermore, some of the referenced literature studies were conducted using synchrotron radiation at a designated facility. To obtain beam time at such a research institution can be a difficult and time consuming process. With the development and demonstration of the capability of the combined approach of TOF-SIMS and rL-SNMS, it is now possible to perform spatially resolved analysis of DGR materials in the Nuclear Chemistry. This opens the possibility of sample pre-screening "in-house" which safes beam time during the development phase of new sample preparation methods or can provide already strong preliminary data for the beam time application. Currently, experiments and measurements are ongoing to conduct diffusion experiments with Np in OPA based

on the developments and results presented in publication II. With the ongoing setup of a new laser system, it will also be possible to apply the new schemes developed as part of publication IV for rL-SNMS of these samples.

Experimental instrumentation

2.1 Tunable Ti:Sa laser system

The laser system for RIMS and rL-SNMS measurements deployed for most of the measurements presented in the publications I-III consisted of three, so called "standard" titanium-doped sapphire crystal solid-state lasers (Ti:Sa) jointly pumped by a frequency doubled solid-state neodymium doped yttrium aluminum garnet laser (Nd:YAG) at 532 nm with 10 kHz with a total of 45 W laser power and ca. 150 ns to 200 ns pulse width [18, 29, 44].

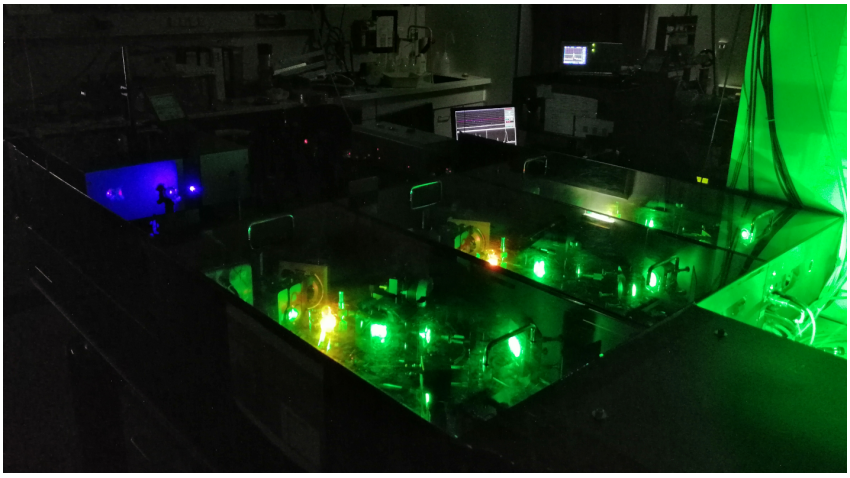

Figure 2.1: Photo of the Ti:Sa laser system in operation in the configuration mostly used in this thesis. In the center are the three Ti:Sa laser with the red fluorescence of the Ti:Sa crystal visible. The green light is emitted by the Nd:YAG pump laser. In the top left the blue light of the external second harmonic generation (SHG) of one Ti:Sa can be seen.

Towards the end of this thesis, the process of upgrading and modernizing the laser system was begun in close collaboration with the LARISSA work group from the Institute of Physics of the Johannes Gutenberg-Universität Mainz, that is specialized in designing and building Ti:Sa. The upgrade includes an additional Nd:YAG pump laser as well as two "grating" and a newly designed "standard" Ti:Sa. Since the upgrade is still ongoing, of these new units only the new pump laser and the new generation "standard" Ti:Sa were used for measurements presented in publication III [18]. However, the "grating" type lasers were already used to great extend for

the work presented in publication IV for the wide range scans of resonances of Np in the laser lab of the LARISSA workgroup [45].

In general, Ti:Sa are tunable in the range from approximately 700 nm to 1000 nm [46]. This property is the result of the strong interaction of the doped Ti^{3+} ions inside the sapphire crystal lattice which broadens the energy levels and leads to a continuous fluorescence spectrum. A schematic of such a tunable four level laser, like a Ti:Sa, is shown in figure 2.2.

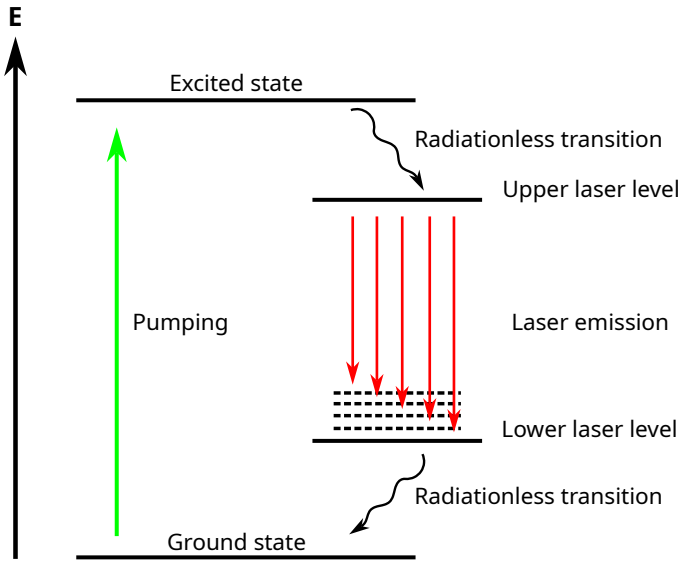

Figure 2.2: Schematic of a tunable four-level solid state laser.

In such a system, a short lived excited state is populated by optical pumping. From here a radiationless transition through coupling of phonons populates the longer-lived upper laser level. Either through spontaneous or stimulated emission the system then relaxes into the lower laser level which is broadened by the interaction of the ion with the doped crystal lattice. This results in the emission of a spectrum since transitions of different energies are possible. From the lower laser level the system once again relaxes without radiation into the ground state from which the cycle can start again.

For tuning the laser to a specific wavelength different optical components are placed inside the laser cavity depending on the laser design and application. The "standard" Ti:Sa features a Z-shaped cavity and uses a Lyot filter consisting of three birefringent crystals in combination with an Fabry-Pérot etalon for wavelength selection. Figure 2.3 shows schematics for the old generation, as it was used for almost all measurements in this thesis (**a**) and the current generation design (**b**).

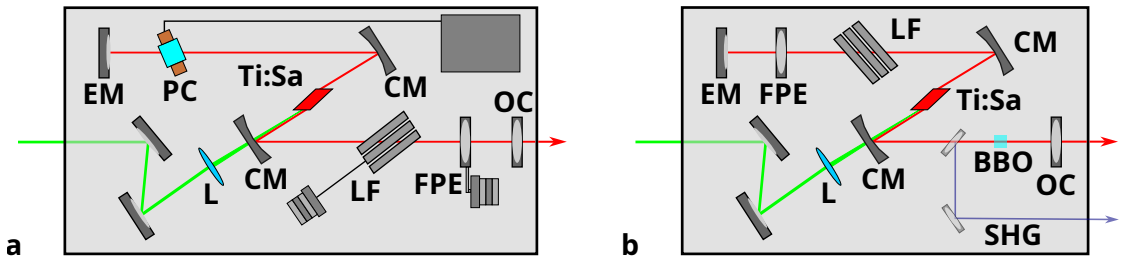

Figure 2.3: Schematic of the old (**a**) and new generation (**b**) "standard" Ti:Sa cavity. Both desings feature a focusing lense (L) for the pump beam, the curved mirrors (CM) around the Ti:Sa crystal (Ti:Sa), an end mirror (EM), Lyot filter, Fabry-Pérot etalon and an output coupler (OC). The old design included a Pockels cell (PC) for temporal synchronisation which is not required in the new design. The new generation unit features optional IC-SHG for which the OC is replaced with an end mirror and a beta-barium borate crystal (BBO) is placed inside the cavity. Not to scale.

The biggest difference between the old and current generation "standard" Ti:Sa, beside a significant reduction in size, is the lack of a Pockels cell in the modern units. In the old design, the Pockels cell functions as a q-switch in the resonator and prevents the laser from oscillating when a high voltage is applied to it and the laser pulse can be delayed with respect to the pump pulse of the Nd:YAG. If the Ti:Sa lasers are operated at different frequencies the resulting laser pulses are not emitted at the same time, due to the difference in energies of the oscillating waves in the resonator. In the modern units small adjustments to the pulse timing can be done by adjusting the focus of the pump beam into the Ti:Sa crystal and for larger adjustments, by changing its position with respect to the curved mirrors. This eliminates the need for a high voltage supply and the necessary adjustments of the laser cavity during setup. This simplifies the operation of the laser. Additionally, the new design provides ca. 33 % higher output powers at the same wavelength and pump laser power using broadband mirrors.

Another benefit of the new generation Ti:Sa is the ability for intra-cavity second harmonic generation (IC-SHG). In general, higher harmonic generation, i.e. the generation of multiples of the fundamental Ti:Sa wavelength, is necessary to provide photons with enough energy to access the first excited states of many elements, that require blue, or even ultraviolet wavelength. An additional benefit is the potential to reduce the number of lasers required to photoionize an element, therefore simplifying the setup and measurement. For example, Pu has an ionization energy of 6.025 76(25) eV [47]. It requires two frequency doubled Ti:Sa or one frequency doubled and two fundamental Ti:Sa to reach ionization potential of Pu. However, depending on the element and excitation scheme, factors such as efficiency, element selectivity and non-resonant ionization have to be considered whether a two- or three-step scheme is appropriate. Doubling of the frequency, i.e. second harmonic generation (SHG), was only possible with the old generation Ti:Sa in the Nuclear Chemistry by passing the fundamental wavelength through a beta-barium borate

(BBO) crystal outside of the cavity. The efficiency of this single-pass geometry is around 10 % and results in an oval beam shape. The loss of power is the reason why so far only three-step schemes have been accessible with the laser setup, since usually only transitions into the first excited state could be saturated. With IC-SHG laser powers of up to 550 mW will be possible and the emitted beam shape significantly improved.

The "grating" Ti:Sa was developed to allow the continuous scanning of the full Ti:Sa range without the need to adjust the laser mode via the LYOT filter or the FABRY-PÉROT etalon. Like the "standard" Ti:Sa, it makes use of a Z-shaped cavity with the Ti:Sa crystal, the two curved mirrors and two parallel arms. However, the end mirror is replaced with an optical grating (GR) in LITTROW configuration which replaces the LYOT filter and the FABRY-PÉROT etalon. Figure 2.4 displays a schematic of a "grating" Ti:Sa.

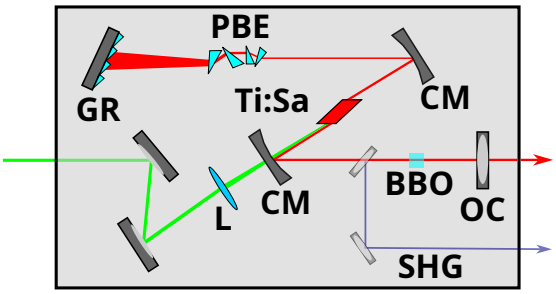

Figure 2.4: Schematic of the "grating" Ti:Sa featuring an optical grating mounted on a motorized rotating stage for wavelength selection (GR), a prism beam expander (PBE) to prevent damaging the GR. Other components, such as the curved mirrors (CMs) and the output coupler (OC) and the Ti:Sa crystal (Ti:Sa) as well as the pump beam focusing lens (L) are similar to the "standard" Ti:Sa. IC-SHG is available by replacing the OC with an end mirror and placing a beta-barium borate crystal (BBO) inside the cavity. Schematic not to scale.

The GR is mounted on a rotary motorized stage to scan seamless over the Ti:Sa range. This makes this Ti:Sa type an excellent tool for spectroscopic studies and allows for fast switching between excitation schemes for different elements. The output wavelength of the "grating" Ti:Sa is adjusted by rotating the GR. The GR has groves which causes phase shifts in the reflected light depending on the wavelength and the incident angle and therefore constructive and destructive interference. To prevent damaging the GR, a set of four prisms is installed into the cavity as prism beam expander (PBE) that widens the beam before the optical grating and collimates it after the diffraction. Also the "grating" Ti:Sa is designed to allow for IC-SHG. To guarantee a stable laser power output, the BBO crystal mount can also be motorized to allow necessary adjustments for optimal output power when scanning over a wide wavenumber range.

Depending on the application, the laser system of the Nuclear Chemistry can

either be coupled with the RIMS setup for environmental samples or the TOF-SIMS III via a respective multimode optical fiber, or, for the former, also directly. The wavelengths of the lasers are monitored via a wavemeter (WS6-200, Highfinesse) equipped with a switch that allows for the quasi-simultaneous monitoring of four Ti:Sa at 200 MHz accuracy. At the time of writing, two of the three old generation Ti:Sa have been replaced with the new "standard" and one "grating" Ti:Sa without IC-SHG. Once the second "grating" Ti:Sa is deployed and IC-SHG is implemented, the new configuration will allow for the use of novel excitation schemes [45, 48] as well as the simultaneous operation of the two mass spectrometers for RIMS and rL-SNMS measurements with two-step excitation schemes. In summary, in combination with higher harmonic generation, Ti:Sa are an excellent tool for RI application since they can cover a wide variety of excitation schemes for the vast majority of elements in the periodic table.

2.2 Resonance ionization mass spectrometry setup

The RIMS setup of the Nuclear Chemistry is used for spectroscopic measurements of radionuclides and the quantification of radioisotopes in environmental samples. The setup can be divided into two parts: A source region and the TOF-MS. A schematic is shown in figure 2.5 and photos of the source region and the TOF-MS section in figure 2.6.

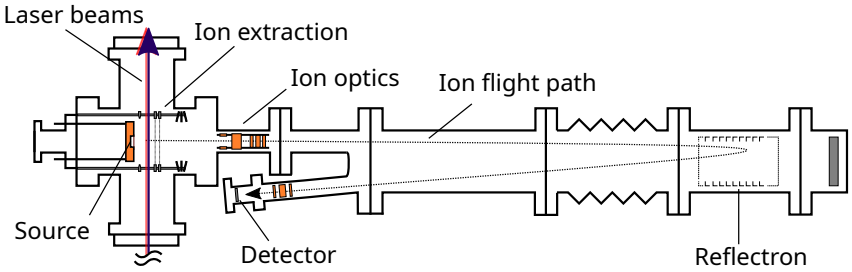

Figure 2.5: Illustration of the RIMS setup for spectroscopic studies and routine measurements on environmental samples. Not to scale. The figure was taken from publication III [18].

The atoms necessary for RIMS measurements are generated in the source region by resistively heating a tantalum filament on which the sample has been electrodeposited up to 1250 °C. This produces an atomic plume inside the source region, in which then the laser beams are shown. In case of Pu or Np, these electrodepositions are additionally coated with an approximately 1 µm thick layer of titanium before the measurement in a custom sputter setup. The titanium serves as a reducing agent and increases the atomization efficiency since both Pu and Np are deposited as ionic species during the electrodeposition. The source region is equipped with two electrodes, one copper and one corrosive resistant steel, to suppress thermal ions and electrons. The laser beams for RIMS can be introduced through view

ports of the source region either via a multimode optical fiber or directly. In both cases the beams are shown into the atomic cloud perpendicular to the ion extraction. This geometry on one side eliminates effects such as DOPPLER broadening and therefore improves the resolution for spectroscopic measurements, on the other side, it reduces the ionization volume compared to a co-linear arrangement which decreases efficiency. The photoions are extracted into the TOF-MS with an extraction electrode operating at ca. 1.3 kV. The source region is connected to the TOF-MS via a vacuum shutter. This allows to change the sample in the source region without having to vent the whole apparatus. The TOF-MS is equipped with two ion lenses to focus the beam and deflectors to guide it along the drift-path onto the detector. A reflector extends the total drift path to approximately 215 cm while keeping the setup's footprint small and furthermore enhances the temporal of the MS resolution by compensating for small deviations in the kinetic energy between ions of the same mass. At the end of the drift path, the ions are detected using a multi-channel plate detector (MCP). The vacuum for measurements is $<2 \times 10^{-6}$ mbar. The instrument was used for the spectroscopic investigations and efficiency measurements for publication III.

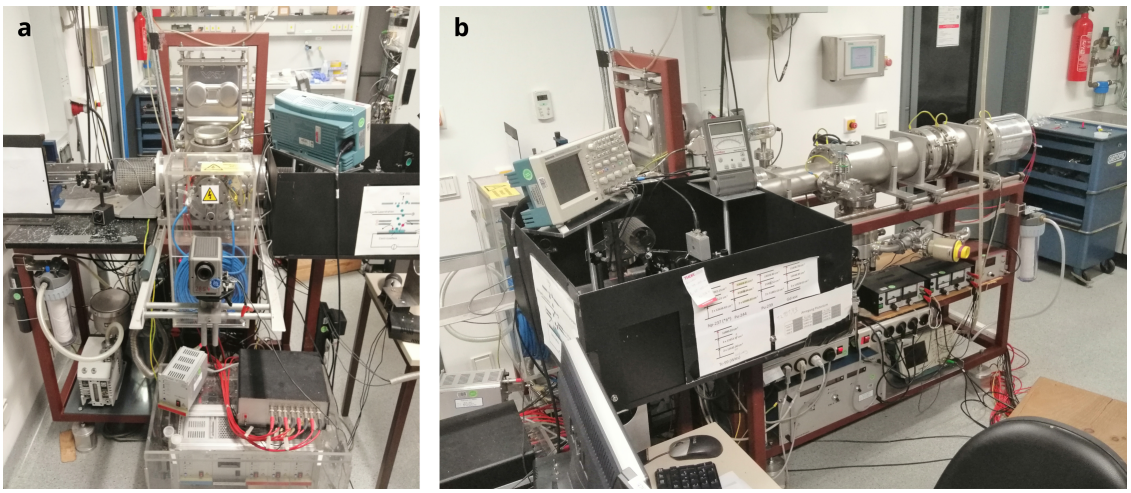

Figure 2.6: Photos of the source region (**a**) and the TOF-MS section (**b**) of the RIMS setup for environmental samples and spectroscopic investigations in the Nuclear Chemistry Mainz. In the source region the lasers can be introduced via an optical fiber from the left, or directly from the right.

2.3 Time-of-flight secondary ion mass spectrometry

The TOF-SIMS in the Nuclear Chemistry is the commercially available TOF-SIMS III (iontof GmbH, Münster, Germany). It features a double lens liquid metal ion gun (LMIG) with $^{69}Ga^{+}$ as primary ion (PI) source for sputtering the sample, a TOF-MS with a reflectron and an electron floodgun for charge compensation. A schematic is shown in figure 2.7.

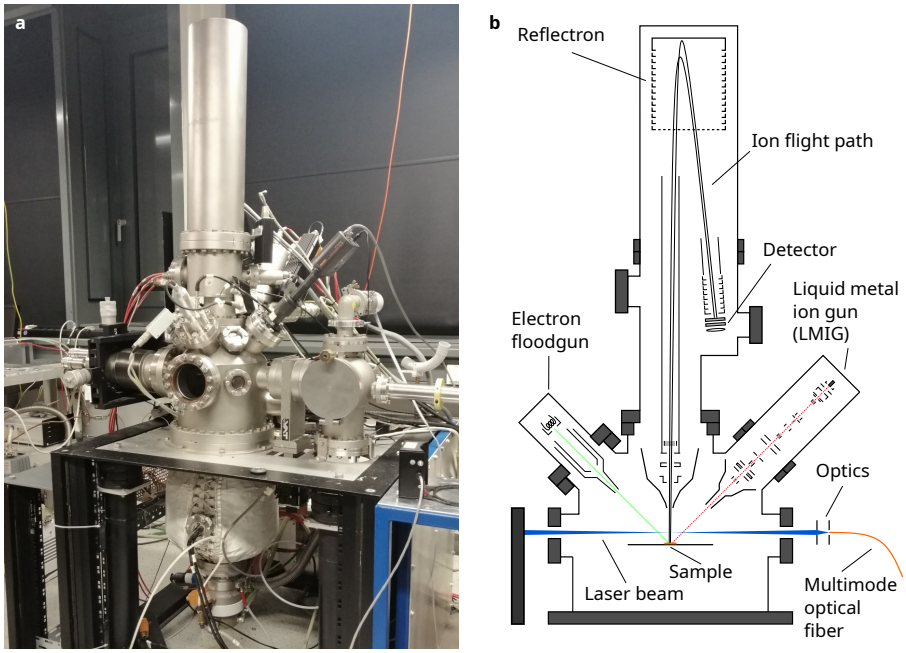

Figure 2.7: Photo (**a**) and schematic (**b**) of the ToF-SIMS III in the Nuclear Chemistry Mainz. The illustration was adapted from [49]. Not to scale.

The instrument's components were overhauled in 2016 and the experiment control system upgraded to TOF-SIMS V level. This included a new measurement PC for the measurement and analysis Software SurfaceLab 6.6 and a time to digital converter connected via USB (USB-TDC). The USB-TDC is also used as the master clock for the temporal synchronization of the TOF-SIMS III with the laser system. Further details of the upgrade and the components can be found in [50] and [51]. Measurements are conducted at pressures $<1 \times 10^{-7}$ mbar. Samples are introduced via a separate loading chamber that is separated from the analysis chamber via a shutter. The maximum field of view (FOV) of the TOF-SIMS III is 500 µm × 500 µm. Measurements are usually conducted at resolutions of 256 px × 256 px or 512 px × 512 px

Time-of-flight secondary ion mass spectrometry (TOF-SIMS) is a spatially resolved surface analysis technique. A pulsed beam of PIs is scanned over a sample and erodes material in the form of cations, anions as well as neutral particles and molecules. Figure 2.8 displays a schematic of this process.

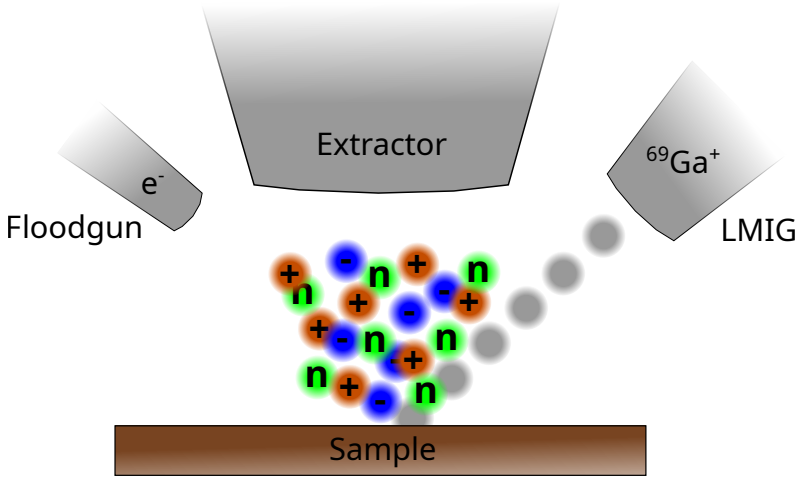

Figure 2.8: Graphical representation of the TOF-SIMS sputtering process. $^{69}Ga^{+}$ pulsed primary ions (PIs, gray) are scanned from a liquid metal ion gun (LMIG) over a sample where surface material is eroded as cations (brown), anions (blue) and neutral species (green). Depending on the polarity, cations or anions are then extracted into the mass analyzer. An electron floodgun is available for charge compensation.

By extracting the secondary ions (SIs) into a TOF mass analyzer, a mass spectrum is recorded for every sputtered position. Depending on the polarity of the extraction voltage, either a cationic or anionic spectrum is accessible. Through comparison of the relative intensity for an analyte's mass within the total field of view (FOV) for each sputtered position, the distribution of said mass on the surface can be observed. This is called mass spectrometry imaging (MSI). Since the TOF-MS allows for the simultaneous observation over a wide mass range, the composition of the sputtered surface is accessible.

There are a broad spectrum of theoretical descriptions for the interaction between a sample and the PIs leading to the generation of SIs and neutral species [52]. In a simple manner the sputtering process can be described as single knock-on sputtering: Here, the kinetic energy of the PIs is insufficient to start a cascade in the sample. Usually the kinetic energy of the PIs is in the eV to low keV regime. If the transferred energy in a direct collision is bigger than the binding energy, the bumped particle has a chance to leave the sample. For TOF-SIMS, the PI source usually operates in the linear-cascade regime [53], with acceleration energies around 25 keV. Here, the energy of the PI is sufficient to induce primary recoils in the sample which still have sufficient energy to induce secondary recoils. Through this cascade, the sample gets eroded and material released. Figure 2.9 displays a schematic representation of the two processes.

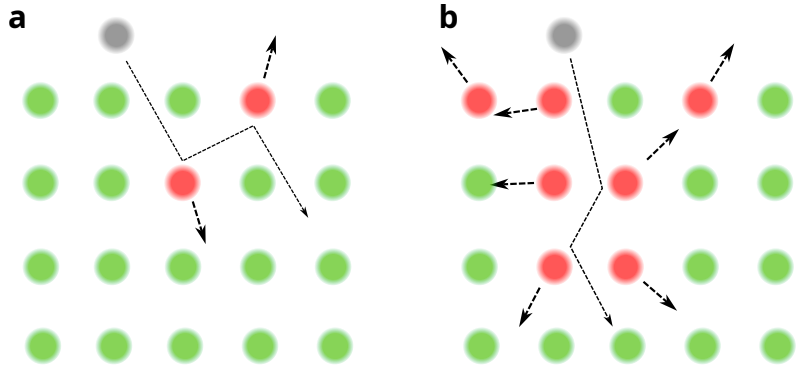

Figure 2.9: Illustration of single knock-on (**a**) and linear cascade (**b**) sputtering. The primary ion (gray) collides with atoms of the sample (green). Only for **b** the PI has enough energy to start a cascade inside the sample.

The PI beam has a significant influence on the amount and composition of the sputtered material [54]. Depending on the size and acceleration of the PIs, the sputtered material may contain more single elements, fragments of larger molecules or even whole molecules. Therefore, a wide range of PI sources has been developed. The most commonly used are Ga^+, Bi^+, $Bi_3{}^+$, $C_{60}{}^+$ and Ar-cluster. The latter can produce up to Ar_{1000} cluster and is able to sputter complete ions with masses >1000 u [55].

Although TOF-SIMS is a very sensitive analytical technique with a wide range of applications, it has a few disadvantages: Especially when analyzing surfaces with a complex composition, isobaric interferences can not be excluded. Additionally, the sputter rate of the ions depends heavily on the chemical environment. This phenomenon is known as the *matrix effect* and is in some studies actively used to enhance the signal by introducing additional chemical compounds [56]. Furthermore, absolute quantification is not possible via TOF-SIMS unless a reference with a known amount of analyte identical to the sample is available for direct comparison of signal intensities. In absence of such a standard, only relative comparisons between samples of the exact same composition can be made. The addition of rL-SNMS presented in publication I as a method of post-ionization addresses the disadvantage of isobaric interferences.

2.4 Resonant laser secondary neutral mass spectrometry

As mentioned in the introduction, resonant laser secondary neutral mass spectrometry (rL-SNMS) is the combination of TOF-SIMS and RIMS. Using multi-step element selective RI via lasers on the sputtered neutrals (SNs) produced by the PI beam of the TOF-SIMS results in an enhanced signal of a selected element. The feasibility of using the TOF-SIMS III in the Nuclear Chemistry for rL-SNMS

measurements was demonstrated by Erdmann et al. [57]. The development process and first applications of the post-ionization of Pu via RI have been documented in publication I. In combination with suppression of the SIs, this method of post ionization allows for effective suppression of isobaric interferences and isolation of an analyte signal in the TOF-SIMS, as demonstrated for a pyrite particle contacted with Pu in publication I. This is especially useful in case the sample contains only trace amounts of the element of interest that otherwise would disappear in the background [58]. Furthermore, by detuning the lasers used for the excitation, it is possible to directly quantify the background and the selectivity of the RI serves as proof for the attribution of a signal observed on a certain mass to a specific element. The suppression of SIs is achieved by applying an additional voltage to the tip of the mass analyzer's extractor in combination with a delay of the extraction which allows the SNs to move into the laser interaction volume above the sample surface. The resulting photoions are then simply extracted into the mass analyzer and separated according to their mass-to-charge ratio. A schematic of the process is displayed in figure 2.10.

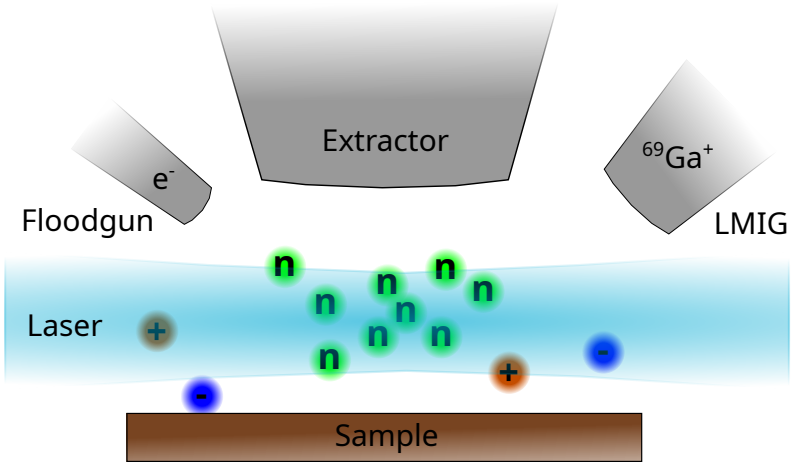

Figure 2.10: Schematic of the rL-SNMS post ionization process. The resonant ionization of neutral species takes place above the sample surface after the suppression of the secondary ions. Crucial for this process is the timing of the primary ion and laser pulse with reference to the delay of the extraction.

As shown in figure 2.7 and described further in publication I, the laser beams required for rL-SNMS measurements are transported via a multimode optical fiber to the TOF-SIMS III and then introduced into the analysis chamber via a view port. This setup ensures consistent beam alignment below the mass extractor, but limits the beam shape and diameter as well as the laser power available. The transmission loss depends on the wavelength, but can be up to 60 % for blue light. While this is still sufficient to saturate the FES in three-step schemes, it might cause issues with novel blue-blue two-step schemes. In order to achieve higher laser powers in the future, the laser beams could also be directly introduced into the TOF-SIMS III.

At the current state of development of the rL-SNMS setup in the Nuclear Chemistry it is possible to study the geochemical interactions of Pu with DGR materials as showcased in publications I and II. However, depending on the sample type, rL-SNMS shows in some cases a reduced signal for Pu compared to TOF-SIMS. One possible explanation is that only Pu^+ photoionized from the ground state of atomic Pu is observed. If Pu is present as Pu(V) or Pu(IV) as in OPA [39], the amount of atomic Pu produced in the sputter process might be smaller compared to Pu^+ or PuO^+. Nevertheless, despite the reduced signal, it was possible to verify the spatial Pu distributions measured by TOF-SIMS with rL-SNMS and support the findings. With the ability to apply novel excitation schemes and higher laser powers due to the new laser system, this is expected to improve in the future.

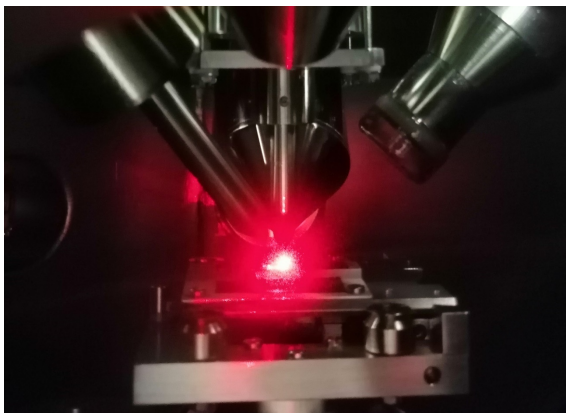

Figure 2.11: Photo of the red alignment laser in the TOF-SIMS during setup. The laser is directly positioned under the extraction electrode of the TOF-MS above the sample. Behind the extraction electrode is the LMIG, on the left the electron flood gun. On the right is the video camera for the observation of the sample during moving and adjustment of the distance to the extractor.

Publication I: Development, characterization, and first application of a resonant laser secondary neutral mass spectrometry setup for the research of plutonium in the context of long-term nuclear waste storage

Contribution statement

The measurements of Pu electrodepositions and pyrite particles presented in this publication were originally conducted as part of the diploma thesis of the author in 2018 in collaboration with [redacted]. An original draft of this publication was written by [redacted], who measured the hardened cement paste and Macor© samples as part of her PhD, with contributions by the author in the first year of his PhD. However, this draft was not finalized and submitted by [redacted]. For the submission in 2020, the author repeated the formal analysis of all datasets, amended the visualizations and prepared the final manuscript for publication. He was also responsible for the revision.

Copyright

Analytical and Bioanalytical Chemistry
https://doi.org/10.1007/s00216-021-03350-3

RESEARCH PAPER

Development, characterization, and first application of a resonant laser secondary neutral mass spectrometry setup for the research of plutonium in the context of long-term nuclear waste storage

Daniela Schönenbach[1] · Felix Berg[1] · Markus Breckheimer[1] · Daniel Hagenlocher[1] · Pascal Schönberg[1] · Raphael Haas[1,2,3] · Samer Amayri[1] · Tobias Reich[1]

Received: 13 November 2020 / Revised: 21 March 2021 / Accepted: 14 April 2021

Abstract
Plutonium is a major contributor to the radiotoxicity in a long-term nuclear waste repository; therefore, many studies have focused on interactions of plutonium with the technical, geotechnical, and geological barriers of a possible nuclear waste storage site. In order to gain new insights into the sorption on surfaces and diffusion of actinides through these complex heterogeneous materials, a highly sensitive method with spatial resolution is required. Resonant laser secondary neutral mass spectrometry (Laser-SNMS) uses the spatial resolution available in time-of-flight secondary ion mass spectrometry (TOF-SIMS) in combination with the high selectivity, sensitivity, and low background noise of resonance ionization mass spectrometry (RIMS) and is, therefore, a promising method for the study and analysis of the geochemical behavior of plutonium in long-term nuclear waste storage. The authors present an approach with a combined setup consisting of a commercial TOF-SIMS instrument and a Ti:sapphire (Ti:Sa) laser system, as well as its optimization, characterization, and improvements compared to the original proof of concept by Erdmann et al. (2009). As a first application, the spatial distributions of plutonium and other elements on the surface of a pyrite particle and a cement thin section were measured by Laser-SNMS and TOF-SIMS, respectively. These results exemplify the potential of these techniques for the surface analysis of heterogeneous materials in the context of nuclear safety research.

Keywords Plutonium · Laser-SNMS · Resonant laser ionization · Ultra-trace analysis · TOF-SIMS · Nuclear waste

Introduction

Due to the long half-lives of its isotopes, such as ^{239}Pu (2.41×10^4 a) and ^{242}Pu (3.75×10^5 a), plutonium is considered one of the major contributors to the long-term radiotoxicity of nuclear waste. Its complex aqueous chemistry makes the study of its geochemical interactions with technical and geotechnical barriers, as well as the host rock system, vital for the safety assessment of possible sites for long-term storage of nuclear waste [1]. The current plans for a future German nuclear waste repository involve a multi-barrier concept in a deep geological formation storing high-level nuclear waste for one million years, with the possibility of retrieval for 500 years. Among others, clay rock is considered as a possible host rock, and cementitious materials will be part of the technical barrier [2]. Migration and sorption studies evaluating clay rock and cementitious materials as geological and technical barriers for long-term nuclear waste storage are conducted using environmentally relevant actinide concentrations (10^{-7} to 10^{-9} mol/L) [3–6]. Investigating the interactions of radionuclides with these exceedingly heterogeneous materials requires an analytical method with both high spatial resolution and sensitivity. Due to the long half-lives of the aforementioned plutonium isotopes, common radiometric analytical tools, such as alpha-spectroscopy, do not provide sufficient sensitivity. Several mass spectrometric methods adequate for a limit of detection (LOD) of 10^5 to 10^8 atoms, such as thermal ionization mass

✉ Tobias Reich
tobias.reich@uni-mainz.de

[1] Department of Chemistry, Johannes Gutenberg-Universität Mainz, 55099 Mainz, Germany

[2] Helmholtz-Institut Mainz, 55099 Mainz, Germany

[3] GSI Helmholtzzentrum für Schwerionenforschung GmbH, 64291 Darmstadt, Germany

Published online: 10 May 2021

spectrometry (TIMS) [7] or inductively coupled plasma mass spectrometry (ICP-MS) [8], suffer from isobaric interferences. While accelerator mass spectrometry (AMS) and resonance ionization mass spectrometry (RIMS) [9, 10] are able to address this problem and provide the necessary sensitivities, they require extensive sample preparation and are only used for bulk analysis without any spatial information. Secondary ion mass spectrometry (SIMS) is a spatially resolved method, but it can be hampered by isobaric interferences and matrix effects [11].

The analytical method described here aims to combine the spatial resolution of SIMS with the highly selective resonant photoionization applied in RIMS. RIMS requires the analyte in an atomic state. During the sputtering process in SIMS, the vast majority of the eroded surface material is not ionized and, therefore, lost for detection. Different approaches to make these so-called secondary neutrals (SNs) available for mass spectrometry via post-ionization and to overcome the disadvantages of SIMS were developed in the past. Electron beam and plasma secondary neutral mass spectrometry (SNMS) [12, 13] both make use of ionization through electron impact. Electron beam SNMS has been shown to provide useful SN yields around 10^{-8} [14]. For plasma SNMS, a useful yield of around 10^{-5} has been reported [15, 16]. Furthermore, several attempts using non-resonant laser ionization of SNs have been made, which resulted in useful yields of 1% [17] or more [18, 19]. Nevertheless, these methods also suffer from isobaric interferences. Resonant photoionization suffers from a loss in analytical flexibility since it is element and even isotope specific, but due to higher cross sections it results in even higher useful yields compared to the non-resonant process [15]. Resonant Laser-SNMS has already been successfully applied to various sample types such as crystalline materials, doped semi-conductors, ocean sediments, and organic polymers [20–25], and has proven to be adequate for the analysis of radioactive samples [26–30] using fully custom-built TOF-MS as well as adapted commercially available TOF-SIMS instruments in combination with a wide range of laser systems.

For the initial tuning of the system for conducting and non-conducting sample types, samples with electrodeposited ^{239}Pu on titanium foil and ^{239}Pu(IV) solution dropped onto ceramic platelets were analyzed. In addition, the following two sorption samples were investigated as proof of concept for the application of Laser-SNMS in the context of nuclear safety research: (i) pyrite particles with a challenging topography were extracted from Opalinus Clay rock (OPA) and exposed to ^{239}Pu(VI) solution and (ii) a thin section of hardened cement paste (HCP) was exposed to ^{242}Pu(III) solution. Surface mappings obtained for both systems by TOF-SIMS and Laser-SNMS show the potential of both methods in the context of nuclear safety research.

Experimental section

Experimental setup

The Laser-SNMS setup (Fig. 1) consisted of a commercial time-of-flight secondary ion mass spectrometer (TOF-SIMS III, IONTOF GmbH, Münster, Germany) and a custom-built Ti:sapphire (Ti:Sa) laser system. The TOF-SIMS instrument is equipped with a 25 keV ^{69}Ga liquid metal ion gun (LMIG) as the primary ion source, a reflectron TOF mass analyzer, and an electron flood gun for charge compensation. The instrument control was upgraded to the IONTOF TOF-SIMS V level, including a USB-TDC and IONTOF SurfaceLab 6.6 instrument control and analysis software.

The laser system consisted of three tunable Ti:Sa lasers jointly pumped by a single frequency-doubled Nd:YAG laser (Photonics Industries International Inc., Gröbenzell, Germany, model DM532-60) at 532 nm, with 45 W of total output power at 10 kHz. The TOF-SIMS instrument and the laser system were synchronized by feeding the TOF-SIMS master timing signal into a pulse generator (BNC, San Rafael, USA, model 577). This device generated the trigger signal for the laser system which allowed for a variable delay of the laser pulses with reference to the TOF-SIMS duty cycle. Laser wavelengths were monitored using an LM007 Wavemeter (ATOS). The laser system was described in greater detail in previous publications [31, 32].

The excitation schemes for resonant ionization used in this work are presented in Fig. 2 [33]. The laser light was transmitted to the TOF-SIMS instrument via an optical fiber and introduced into the photon-SN interaction region through a CF viewport. A telescope on a 5-axis translation and rotation stage was used for focusing and positioning the beam directly under the extraction electrode of the TOF-SIMS. The use of an optical fiber allowed for reproducible beam positioning, but limited the minimum focus diameter to approximately 1 mm due to the beam divergence at the end of the fiber. During standard SIMS operation, the distance between the sample surface and the extraction electrode is 1.5 mm. This distance was increased to 2.5 mm for both TOF-SIMS and Laser-SNMS in order to prevent the diverging laser beam from hitting the sample and sample holder. In addition, a newly designed pedestal sample holder allowed for samples to be positioned and moved safely under the laser interaction volume.

Samples and preparation

Different samples were prepared and analyzed with TOF-SIMS and Laser-SNMS to account for the various types of materials encountered in the context of a long-term nuclear waste repository. This approach considers influences from conducting and non-conducting surfaces, as well as sample

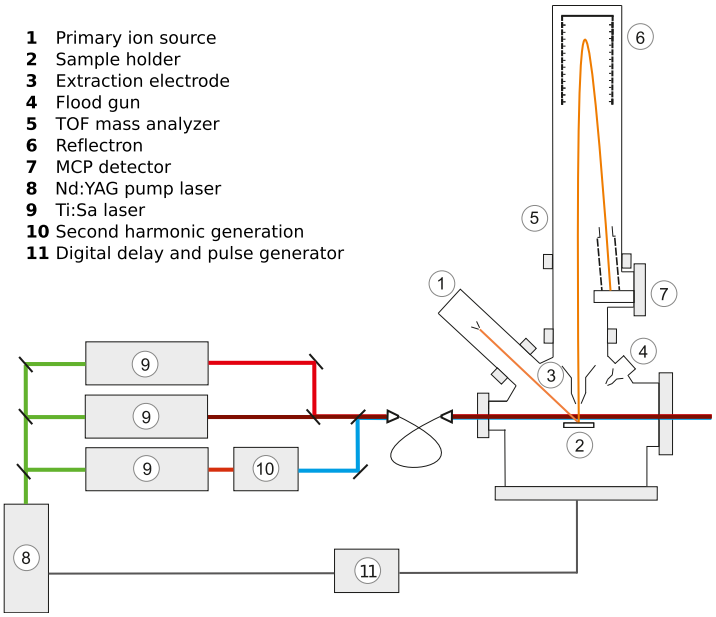

Fig. 1 Schematic illustration of the laser secondary neutral mass spectrometry (Laser-SNMS) set-up: laser system and time-of-flight secondary ion mass spectrometer (TOF-SIMS) III

topography. The respective preparation methods are described below. All samples were attached to the pedestal sample holder using conducting double-sided adhesive carbon tape.

Conducting samples

Synthetic, electrodeposited sample

For the purpose of adapting and optimizing the measurement parameters of the TOF-SIMS instrument for Laser-SNMS on the conducting samples, ^{239}Pu was electrodeposited as a 5-mm diameter spot onto Ti filaments. For the electrolysis, 0.2 g/mL of aqueous $(NH_4)_2SO_4$ electrolyte solution was used, and a current of ~250 mA at 17 V was applied for 1.5 h. Under these conditions, Pu is deposited as a hydroxide. An efficiency for the electrolysis of around 86% was determined via alpha-spectroscopy (partially depleted silicon detector, CR-SNA-450-100, 450 mm^2, 20 keV resolution at 5.486 MeV, Ortec, Germany) for a sample prepared with 10^{11} atoms of ^{239}Pu in the electrolyte solution. Assuming a homogeneous distribution of the Pu layer, the surface loading of a sample can be estimated. The custom electrolysis setup is described in detail in previous publications [32, 34].

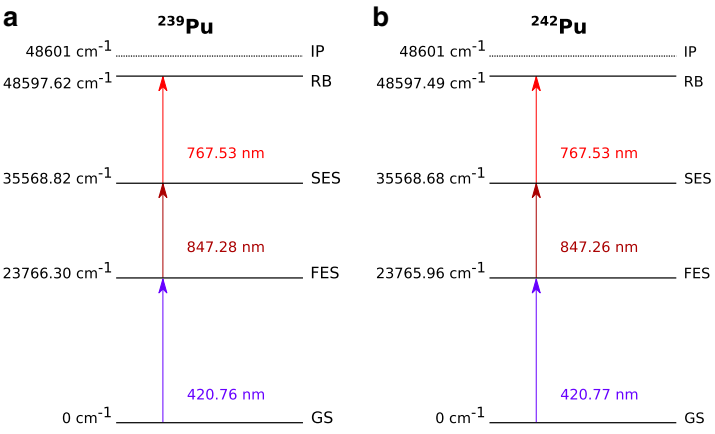

Fig. 2 Excitation schemes for the three-step resonant ionization of ^{239}Pu (**a**) and ^{242}Pu (**b**) [33] from the ground state (GS) using a first and second excitation step (FES and SES) and a Rydberg state (RB) just below the ionization potential (IP)

Semi-synthetic, topographic samples

The Fe(II)-bearing mineral pyrite has been identified in previous sorption experiments as a redox-active component of Opalinus Clay rock (OPA), that is involved in the reduction and immobilization of Pu [3, 35]. Micrometer-sized pyrite particles were extracted from calcite-saturated, aqueous suspensions of OPA and manually sorted under a microscope. The particles were then contacted for 4 days with 1 mL of a ^{239}Pu(VI) solution (2×10^{-5} mol/L, pH 7.8) in OPA pore water [36] saturated with calcite as a background electrolyte. All experiments with wet chemistry were conducted under an argon atmosphere. Afterwards, the particles were extracted from the solution and left to dry on filter paper and their morphology and size characterized via scanning electron microscopy (SEM, Philips XL 30). For TOF-SIMS and Laser-SNMS measurements, the primary ion (PI) beam was rastered in sawtooth movement over an area of 400×400 μm^2 which included the particle at a resolution of 512×512 px and a PI current of 2 μA (LMIG) at a pulse width of 6.5 ns (TOF-SIMS) and 90 ns (Laser-SNMS) with 1 shot/px. The extraction delay was set to 1.165 μs for SIMS and 1.650 μs for SNMS mode with a total duty cycle of 100 μs.

Non-conducting samples

Synthetic, ceramic samples

In order to account for measurements on non-conducting materials encountered in the context of a nuclear waste repository, e.g., clay rock and cementitious materials, specific operational parameters were determined for insulating surfaces. Two microliters of a ^{239}Pu solution (6×10^{-4} mol/L in 6 mol/L HNO_3) were applied in 20 nL droplets on smooth glass–ceramic discs (Macor®, ⌀ = 7 mm, 1 mm thickness) using a drop-on-demand inkjet printing system [37].

Semi-synthetic, non-topographic sample

An HCP sorption sample was produced using Portland cement (OPC, CEM I, Dyckerhoff GmbH, Wiesbaden, Germany), prepared according to DIN EN 196-3 and hardened in water for at least 28 days. A thin section (9 mm × 7.5 mm) was prepared, embedded in epoxy resin (EpoxiCure 2 Resin and EpoxiCure 2 Hardener, Buehler, Lake Bluff, IL, USA), and attached to a glass carrier plate (⌀ = 10 mm). The surface of the thin section was conditioned in a custom sorption cell with artificial cement pore water (ACW) [38] for 24 h. Afterwards, it was contacted with 5 mL of ^{242}Pu(III)-ACW solution (2.13×10^{-5} mol/L, pH 13) for 72 h under an argon atmosphere. This concentration of Pu was well above the solubility limit, but additional experiments with the sample required an excess of the analyte. After drying, around 10^{15} atoms of ^{242}Pu were detected on the surface of the thin section using alpha-spectroscopy. TOF-SIMS and Laser-SNMS measurements were conducted using the electron flood gun for charge compensation and applying a surface potential of −140 V. The HCP sample was rastered in random mode with a field-of-view of 500×500 μm^2 at a resolution 256×256 px with 10 shots/px at 2 μA PI current (LMIG) and a pulse width of 13.5 ns for TOF-SIMS and 150 ns for Laser-SNMS at 10 kHz repetition rate with no extraction delay in case of TOF-SIMS and 1.550 μs for Laser-SNMS.

Results and discussion

Characterization of the Laser-SNMS setup

Settings for conductive and non-conductive samples

The initial adaptation of the system for Laser-SNMS, as well as the laser beam and laser focus positioning and adjustment of timing to retrieve a first resonant signal, was carried out using a Gd foil, and the resonant excitation scheme for Gd described in [27]. After a first resonant signal had been achieved, the operational parameters were optimized for Pu.

Changes to the operational parameters of the instrument included the LMIG ^{69}Ga PI beam focus and position, as well as the mass analyzer to account for the increased distance of 2.5 mm between the sample surface and the extraction electrode and the different points of origin for secondary and laser ions. The PI pulse width for Laser-SNMS measurements was increased compared to 10 ns in TOF-SIMS mode in order to produce more SNs in the laser interaction volume, which resulted in an increase in photo ions, as displayed in Fig. S1 in the Supplementary information (ESM). The timing sequence of primary ion pulse, laser pulse, and laser ion extraction had to be set up for Laser-SNMS operation. Timing schemes for SIMS and Laser-SNMS are displayed in Fig. 3.

In standard SIMS mode, the extraction voltage is applied to the extraction electrode before the PIs hit the sample surface. All subsequently emitted secondary ions (SIs) are immediately accelerated into the mass analyzer, which results in high transmission and increased mass resolution. The extraction voltage is applied for approximately 10 μs. The application of the extraction voltage can be delayed via the SurfaceLab software. In SIMS mode, this is used to delay the extraction of the secondary ions until they have drifted further away from the sample surface. This compensates the distortion of the equipotential lines of the extraction field due to sample topography and the resulting loss of SIs. The principle of delayed extraction was repurposed here for Laser-SNMS operation. In Laser-SNMS mode, the extraction of laser ions is delayed

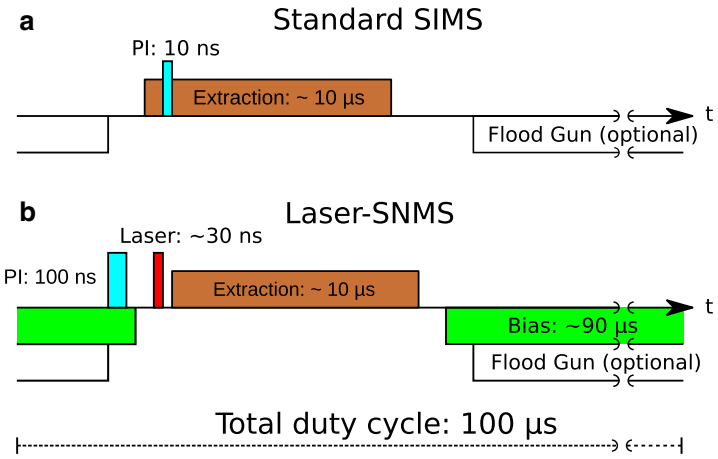

Fig. 3 Timing schemes for non-delayed SIMS (**a**) and Laser-SNMS (**b**) (not to scale)

while a repelling voltage (extraction bias) is applied to the extraction electrode, deflecting SIs from the mass analyzer's acceptance volume while the SNs drift freely into the laser interaction volume. Afterwards, the approximately 30 ns laser pulse is applied after disengaging the bias voltage. The SNs are resonantly photoionized and accelerated into the mass analyzer. The fine-tuning of the laser timings in relation to the extraction of ions is crucial, as displayed by the changes in the ^{239}Pu signal intensity for a conducting sample in Fig. S2 (see ESM). In case of our setup, a laser pulse within a few nanoseconds of the extraction pulse resulted in the highest signal intensity.

The development of new measurement settings for Laser-SNMS described above was carried out for both the electrodeposited ^{239}Pu on Ti foil for conducting samples, and the glass-ceramic discs for non-conducting samples, which were then used for the analysis of the respective semi-synthetic model system. In addition to adapting the operational parameters of the mass analyzer for insulating surfaces, electron flooding using an electron flood gun was deployed for charge compensation, and the raster mode of the LMIG was changed from a sawtooth to a random pattern in order to prevent further local charge buildup. Depending on the sample type, a delay of the laser pulse of −150 to 0 ns in reference to the ion extraction pulse of the mass analyzer was used for subsequent Laser-SNMS measurements.

Table 1 Saturation powers, P_s, and applied powers, P_a, for the three excitation steps of Pu

Step	P_s (mW)	P_a (mW)
First	0.08 ± 0.01	30
Second	14.9 ± 1.3	450
Ionizing	279 ± 26	720

Saturation powers

The saturation powers, P_s, presented in Table 1 were determined using an electrolysis sample with a surface load of 5.6×10^9 atoms per µm^2 of ^{239}Pu. The power of one laser was varied while the other two lasers remained at full power. Despite the third step not reaching saturation, the data were fitted using an extended saturation curve given in Eq. 1 [39]. P_s is the saturation power, A the maximum amplitude of the curve, and I_0 describes the offset caused by the non-resonant ionization generated by other steps, whereas the linear term takes non-resonant ionization and broadening of the beam with increasing laser power into account. Fits and curves are presented in Fig. 4.

$$I = I_0 + A \cdot \frac{P/P_s}{1 + P/P_s} + m \cdot P \quad (1)$$

The measurements in this work were performed using higher laser powers, P_a, in order to maximize the ionization yield. Due to the monoisotopic nature of the samples, saturation broadening can be neglected. However, the first and second excitation steps were attenuated to 30 mW and 450 mW, respectively, to decrease non-resonant ionization and to improve the signal-to-noise ratio. The laser for the ionizing step was usually operated at a power of around 720 mW.

Efficiency of the Laser-SNMS setup

A proof of concept for Laser-SNMS on Pu was presented by Erdmann et al. with the same TOF-SIMS III instrument used in this work before the upgrade in 2009 [27]. Without rastering the PI beam over the sample surface, which ensures complete depletion of Pu in the affected area within a

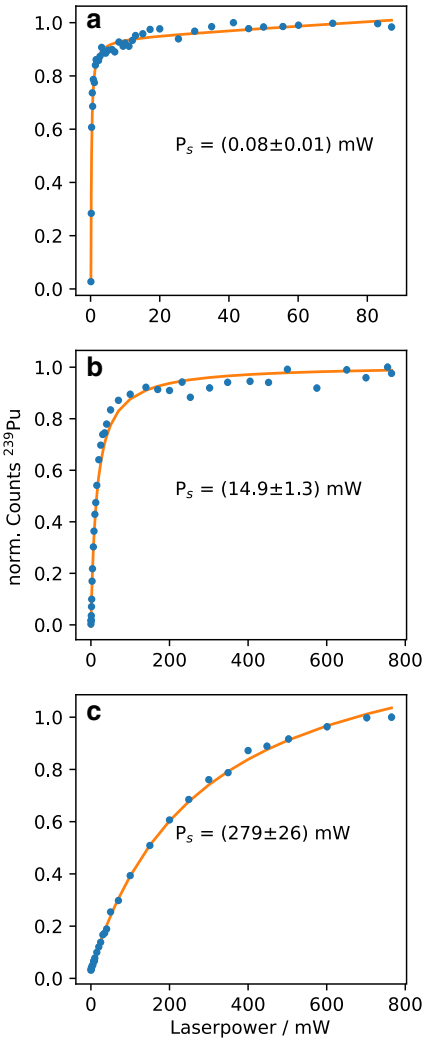

Fig. 4 Saturation curves and fits for the first (**a**) and second (**b**) excitation steps, the ionizing step (**c**), and the respective saturation powers, P_s

reasonable time, an overall efficiency of $\geq 10^{-7}$ was established by Erdmann et al. for a sample with a surface load of 3.5×10^7 atoms per µm^2 of ^{242}Pu and assuming a PI beam focus diameter of 6 µm. Repeating the same experiment twice with the now upgraded setup for an electrodeposition of 7.89×10^3 atoms per µm^2 of ^{239}Pu resulted in an average efficiency of $(7.2 \pm 0.8) \times 10^{-4}$. In an additional measurement, the PI beam was rastered over an area of 18×18 µm^2 of the same sample, and an overall efficiency of $(8.8 \pm 0.3) \times 10^{-4}$ was obtained. This increase in efficiency by three orders of magnitude compared to Erdmann et al. can be attributed to the decreased distance between the extractor electrode and the sample surface (now 2.5 mm compared to 7–8 mm) and the extended optimization of the measurement parameters.

First application

To assess the capabilities of a combined approach of TOF-SIMS and Laser-SNMS for the analysis of Pu in the context of a long-term nuclear waste repository, two semi-synthetic model systems were chosen. Pyrite particles present a very challenging topography, but they can be measured without charge compensation, whereas the HCP thin section has a favorable flat surface but low or no conductivity. The measurements presented here serve as a proof of concept with regard to future experiments.

Figure 5 shows a section of the spectrum with ^{239}Pu contacted pyrite particle in SIMS mode and Laser-SNMS mode. The loss of mass resolution for Laser-SNMS compared to TOF-SIMS is due to an increased extraction delay by 485 ns and the nature of the ionization process. Whereas the SIs are created on PI impact, the photoionization of the SNs takes place in a volume above the sample. When extracted, the increased spatial distribution of the photo ions compared to the SIs results in peak broadening. The strength of Laser-SNMS lies in the reduction of background and, therefore, the increased signal-to-noise ratio by a factor of 15 for this measurement. Detuning the first excitation step allows for background measurements as well as confirmation that the signal observed is indeed the analyte. But this high selectivity also comes with a disadvantage: While with TOF-SIMS it is possible to detect $^{239}Pu^+$, $^{239}PuO^+$, and $^{239}PuO_2^+$ as well as their respective hydrides, this analytical flexibility is lost for Laser-SNMS due to the nature of the ionization process that requires $^{239}Pu^0$. Here, only $^{239}Pu^+$ and non-resonantly ionized $^{239}PuO^+$ are observed. In fact, while TOF-SIMS can detect all components on the sample surface, resonant Laser-SNMS is limited to a single analyte without changing the excitation wavelengths. Furthermore, as Pu is expected to be present as hydroxo species, the majority of the analyte might be sputtered as PuO or PuO_2 and, therefore, not detected using photoionization, as has been demonstrated for uranium [40]. This might also play a role when looking at the differences in the mass images obtained for Pu via TOF-SIMS and Laser-SNMS for the two semi-synthetic model systems. Figures 6 and 7 display the lateral distributions of Pu obtained from TOF-SIMS and Laser-SNMS measurements as well as the total ion distribution in SIMS mode and the SEM images of an area of the HCP thin section and a pyrite particle, respectively. For both samples, SIMS and Laser-SNMS showed a similar distribution of Pu on the sample surface. Areas of increased signal intensity can be identified in both SIMS and Laser-SNMS images, but a significant loss in signal intensity is observed for Laser-SNMS compared to SIMS which can be explained by the aforementioned lack of secondary neutral Pu for photoionization. This results in longer data acquisition times or an insufficient signal for the analysis of the lateral distribution.

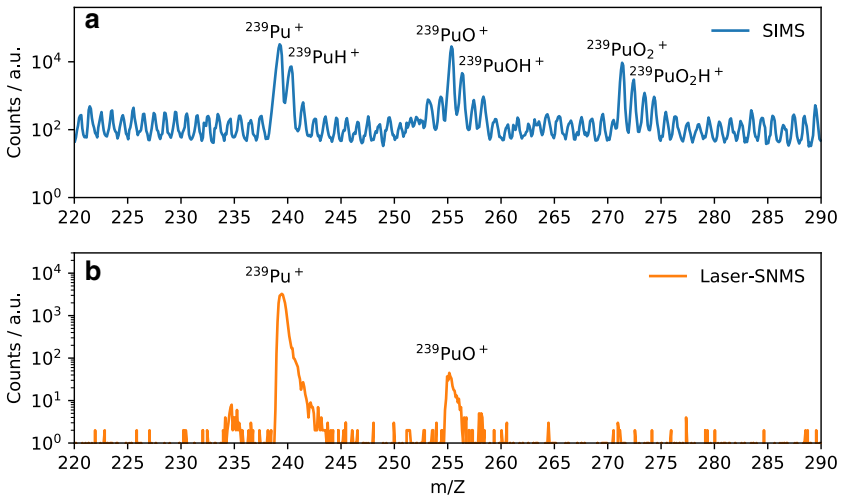

Fig. 5 Sections of spectra obtained in SIMS mode (**a**) and Laser-SNMS mode (**b**) showing the ^{239}Pu signal of a contacted pyrite particle. The SIMS spectrum shows signals for ^{239}Pu, ^{239}PuO, and even $^{239}PuO_2$, as well as their respective hydrides, while the Laser-SNMS spectrum only features resonantly excited ^{239}Pu and non-resonant ^{239}PuO. Binning increment of 0.1 for both **a** and **b**

Additional differences observed in the mappings might be caused by isobaric interferences present in the SIMS measurement, as well as the influence of the chemical environment on the sputter yield, the so-called matrix effect, which was hoped to be reduced for Laser-SNMS [41], but studies have shown that it cannot be eliminated [40, 42, 43]. While no influence of topography was observed in TOF-SIMS mass mappings for the flat HCP thin section (Fig. 6 and ESM Fig. S3), in case of the pyrite particle (Fig. 7 and ESM Fig. S4), the signal might also be disturbed by the strong topography, which is a known challenge for TOF-SIMS [11, 44], and it has also been observed for Laser-SNMS [45]. Local extraction field distortions

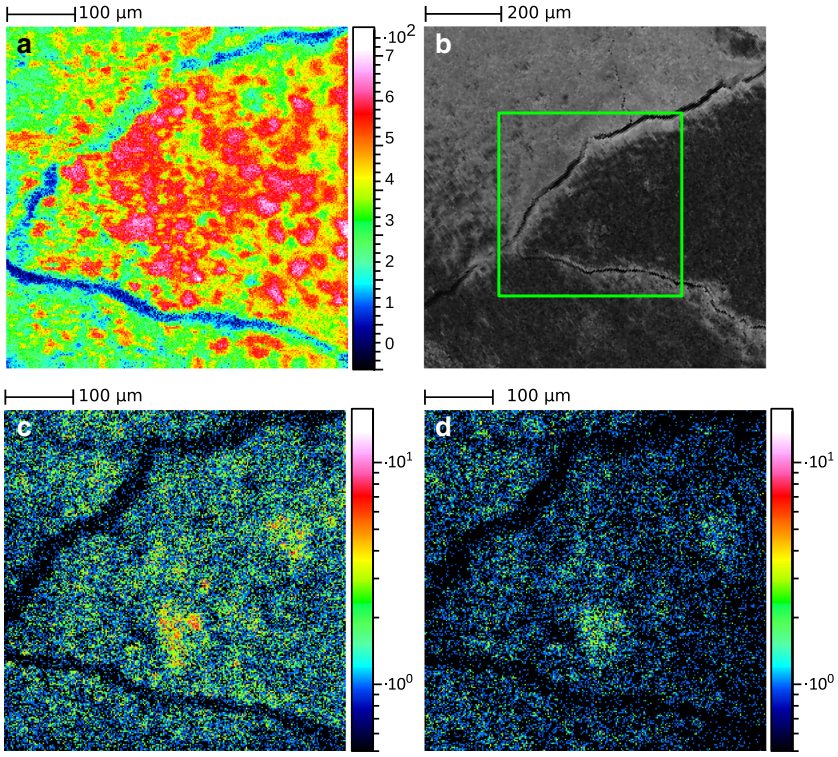

Fig. 6 Total secondary ion image (**a**) and SEM image (**b**) of a section of the non-conducting HCP sorption sample after contact with ^{242}Pu(III) solution. Spatial distribution of ^{242}Pu in SIMS (**c**) and Laser-SNMS mode (**d**). The green square in **b** represents the area scanned in TOF-SIMS and Laser-SNMS

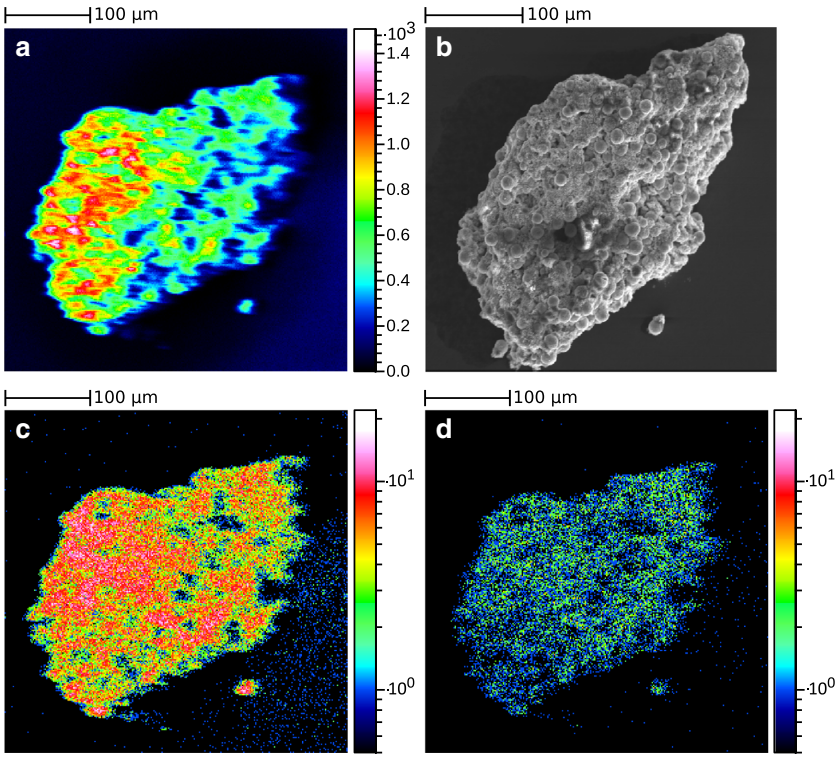

Fig. 7 Total secondary ion image (**a**) and SEM image (**b**) of a pyrite particle extracted from Opalinus Clay rock and contacted with ^{239}Pu(VI) solution. Spatial distribution of ^{239}Pu in SIMS (**c**) and Laser-SNMS mode (**d**). The mass images have been binned by a factor of 4

caused by a non-flat surface hinder homogenous ion extraction from the observed area. The TOF-SIMS mappings for a selection of elements of the pyrite particle presented in ESM Fig. S4 display such a dependency of the ion signal on the geometry of the sample. Nevertheless, since sputtered neutrals get photoionized in a volume above the sample and not on its surface, the effect should be greatly reduced in Laser-SNMS mode.

To evaluate geochemical interactions between Pu and materials encountered in a nuclear waste repository in future experiments, we propose a combined approach using the analytical flexibility of TOF-SIMS to identify components of the material's surface and the high sensitivity and selectivity of Laser-SNMS. Despite all challenges, Laser-SNMS allows for highly selective detection of Pu on the sample surface and, therefore, enhances the analytical capabilities of TOF-SIMS.

Despite that no correlation between surface materials and Pu in both semi-synthetic samples presented in this study has been observed, possibly due to the still relatively high concentrations of Pu used in the sample preparations, the combination of TOF-SIMS and Laser-SNMS offers a new and promising tool for nuclear safety research. Both methods do not require a large facility and can be used without extensive sample preparation in rapid succession by simply loading different operational parameters for the instrument. In addition, the specimen is still accessible for analysis by other means. Despite the material surface being slowly damaged by the PI beam during the measurement, this is limited to the field of view and can be reduced to a minimum.

Conclusion

In this work, a system for resonant Laser-SNMS based on a commercial TOF-SIMS III instrument combined with three tunable Ti:Sa lasers for resonant photoionization was presented. Measurement settings were developed for the analysis of both conducting and non-conducting samples in contact with Pu, and significant improvements in the overall efficiency of the setup were made compared to the original proof of concept. Laser-SNMS was used for the analysis of model systems aimed to gain insight into the complex geochemistry expected in a long-term nuclear waste repository. The resonant Laser-SNMS allowed for significant background suppression and an improved signal-to-noise ratio, improving the identification of Pu even in the presence of isobaric interferences. However, challenges regarding the sputter rate of atomic Pu from the presented samples were identified and require further study. Future studies might include the analysis of diffusion samples, retrieving the diffusion parameters necessary for modeling

migration processes in a long-term nuclear waste repository, or the simultaneous measurement of different radionuclides present in one sample. Since multi-step resonant excitation schemes are already available for other elements and isotopes, the method can easily be transferred to other radionuclides, such as Np [39], Tc [32], or U [46], contributing to the radiotoxicity present in a nuclear waste repository. In conclusion, the combined approach of TOF-SIMS and resonant Laser-SNMS offers a promising tool for nuclear safety research.

Supplementary Information The online version contains supplementary material available at https://doi.org/10.1007/s00216-021-03350-3.

Acknowledgements R. H. acknowledges funding from the Helmholtz Excellence Network ExNet020, Precision Physics, Fundamental Interactions and Structure of Matter (PRISMA+) from the Helmholtz Initiative and Networking Fund. The authors would like to thank Ch.E. Düllmann (Johannes Gutenberg-Universität Mainz) for the use of the target printer and SEM, D. Renisch (Johannes Gutenberg-Universität Mainz) for providing assistance by taking the SEM images and A. Sorowka (Max Planck Institute for Chemistry, Mainz, Germany) for the preparation of the thin section of hardened cement paste. David Jaeggi (swisstopo, Switzerland), Olivier Leupin (NAGRA, Switzerland), and Daniel Grolimund (microXAS Beamline Project, Swiss Light Source, Paul Scherrer Institute, Villigen, Switzerland) are acknowledged for the provision of Opalinus Clay rock samples from the Mont Terri rock laboratory (St-Ursanne, Switzerland).

Funding Open Access funding enabled and organized by Projekt DEAL. This work was funded by the Federal Ministry of Education and Research (BMBF) under contract number 02NUK044B.

Data availability Raw data were generated at the Department of Chemistry, Johannes Gutenberg-Universität Mainz, 55099 Mainz, Germany. Derived data supporting the findings of this study are available from the corresponding author, T.R., upon request.

Declarations

Conflict of interest The authors declare no competing interests.

Supplementary Information The online version contains supplementary material available at https://doi.org/10.1007/s00216-021-03350-3.

References

1. Gompper K. Zur Abtrennung langlebiger Radionuklide. Radioaktivität und Kernenergie. Karlsruhe, Germany: Forschungszentrum Karlsruhe GmbH; 2001. p. 152–67.
2. Jobmann M, Lommerzheim A. Projekt ANSICHT - Endlagerkonzept sowie Verfüll- und Verschlusskonzept für das Endlagerstandortmodell SÜD. Technical Report 2015 3.8.2015 Contract No.: TEC-26-2015-TB.
3. Amayri S, Fröhlich DR, Kaplan U, Trautmann N, Reich T. Distribution coefficients for the sorption of Th, U, Np, Pu, and Am on Opalinus Clay. Radiochim Acta. 2016;104(1):33–40. https://doi.org/10.1515/ract-2015-2409.
4. Marques Fernandes M, Baeyens B, Dähn R, Scheinost AC, Bradbury MH. U(VI) sorption on montmorillonite in the absence and presence of carbonate: a macroscopic and microscopic study. Geochim Cosmochim Acta. 2012;93:262–77. https://doi.org/10.1016/j.gca.2012.04.017.
5. Philipp T, Shams Aldin Azzam S, Rossberg A, Huittinen N, Schmeide K, Stumpf T. U(VI) sorption on Ca-bentonite at (hyper)alkaline conditions – spectroscopic investigations of retention mechanisms. Sci Total Environ. 2019;676:469–81. https://doi.org/10.1016/j.scitotenv.2019.04.274.
6. Bauer A, Fiehn B, Marquardt C, Klein M, Römer J, Schäfer T, Görtzen A, Kienzler B, editors. Results on the Pu diffusion in the Opalinus Clay. 2nd. Annual Workshop Proceedings 6th EC FP-FUNMIG IP; 2006; Stockholm2007.
7. Lee CG, Suzuki D, Esaka F, Magara M, Song K. Ultra-trace analysis of plutonium by thermal ionization mass spectrometry with a continuous heating technique without chemical separation. Talanta. 2015;141:92–6. https://doi.org/10.1016/j.talanta.2015.03.060.
8. Xing S, Zhang WC, Qiao JX, Hou XL. Determination of ultra-low level plutonium isotopes (^{239}Pu, ^{240}Pu) in environmental samples with high uranium. Talanta. 2018;187:357–64. https://doi.org/10.1016/j.talanta.2018.05.051.
9. Hotchkis MAC, Child DP, Froehlich MB, Wallner A, Wilcken K, Williams M. Actinides AMS on the VEGA accelerator. Nucl Instrum Meth B. 2019;438:70–6. https://doi.org/10.1016/j.nimb.2018.07.029.
10. Trautmann N, Passler G, Wendt K. Ultratrace analysis and isotope ratio measurements of long-lived radioisotopes by resonance ionization mass spectrometry (RIMS). Anal Bioanal Chem. 2004;378(2):348–55. https://doi.org/10.1007/s00216-003-2183-8.
11. Gelb LD, Walker AV. Toward understanding weak matrix effects in TOF SIMS. J Vac Sci Technol B. 2018;36(3):03F127. https://doi.org/10.1116/1.5019682.
12. Honig RE. Sputtering of surfaces by positive ion beams of low energy. J Appl Phys. 1958;29(3):549–55. https://doi.org/10.1063/1.1723219.
13. Woodyard JR, Cooper CB. Mass spectrometric study of neutral particles sputtered from Cu by 0- to 100-eV Ar ions. J Appl Phys. 1964;35(4):1107–17. https://doi.org/10.1063/1.1713576.

14. Gersch HU, Wittmaack K. Postionization of sputtered neutrals by a focused electron-beam. J Vac Sci Technol A. 1993;11(1):125–35. https://doi.org/10.1116/1.578278.
15. Mathieu HJ, Leonard D. Use of post-ionisation techniques to complement SIMS analysis. A review with practical aspects. High Temp Mater Proc. 1998;17(1–2):29–44. https://doi.org/10.1515/HTMP.1998.17.1-2.29.
16. Bieck W, Gnaser H, Oechsner H. Analytical performance of a secondary-neutral microprobe with electron-gas positionization and magnetic-sector mass-spectrometer. J Vac Sci Technol A. 1994;12(4):2537–43. https://doi.org/10.1116/1.579053.
17. Terhorst M, Möllers R, Niehuis E, Benninghoven A. High-spatial-resolution surface imaging of inorganic and organic structures by multiphoton post-ionization of sputtered neutrals and time-of-flight mass-spectrometry. Surf Interface Anal. 1992;18(12):824–6. https://doi.org/10.1002/sia.740181208.
18. Henkel T, Tizard J, Blagburn D, Lyon I. Interstellar dust laser explorer (IDLE): a new instrument for submicron analyses of stardust-quantification of laser SNMS. Appl Surf Sci. 2006;252(19):7117–9. https://doi.org/10.1016/j.apsusc.2006.02.139.
19. Veryovkin IV, Calaway WF, Tripa CE, Moore JF, Wucher A, Pellin MJ. Laser post-ionization secondary neutral mass spectrometry for ultra-trace analysis of samples from space return missions. Nucl Instrum Meth B. 2005;241(1–4):356–60. https://doi.org/10.1016/j.nimb.2005.07.041.
20. Pappas DL, Hrubowchak DM, Ervin MH, Winograd N. Atom counting at surfaces. Science. 1989;243(4887):64–6. https://doi.org/10.1126/science.243.4887.64.
21. Arlinghaus HF, Spaar MT, Tanigaki T, McMahon AW, Holloway PH. Sputter-initiated resonance ionization spectroscopy: an analytical technique for quantitative and sensitive measurements of impurities and ultra-shallow doping profiles in semiconductors. J Vac Sci Technol B. 1994;12(1):263–8. https://doi.org/10.1116/1.587151.
22. Staudt C, Wucher A, Bastiaansen J, Philipsen V, Vandeweert E, Lievens P, et al. Sputtering of Ag atoms into metastable excited states. Phys Rev B. 2002;66(8):085415. https://doi.org/10.1103/Physrevb.66.085415.
23. Vering G, Crone C, Kathers P, Bijma J, Arlinghaus HF. Resonant laser-SNMS of boron for analysis of paleoceanographic samples. Appl Surf Sci. 2006;252(19):7163–6. https://doi.org/10.1016/j.apsusc.2006.02.178.
24. Nishinomiya S, Kubota N, Sagara A, Fukumoto N, Morita H, Hayashi S. Matrix effect-free depth profiling of implanted Mg in $Al_xGa_{1-x}As$/GaAs multi-layers by resonance enhanced multiphoton laser post-ionization sputtered neutral mass spectrometry. Surf Interface Anal. 2012;44(6):641–3. https://doi.org/10.1002/sia.4873.
25. Pelster A, Korsgen M, Kurosawa T, Morita H, Arlinghaus HF. ToF-SIMS and laser-SNMS imaging of heterogeneous topographically complex polymer systems. Anal Chem. 2016;88(19):9638–46. https://doi.org/10.1021/acs.analchem.6b02415.
26. Savina MR, Trappitsch R, Isselhardt BH. Electronic excitation of uranium atoms sputtered from uranium metal and oxides. Spectrochim Acta B. 2018;149:214–21. https://doi.org/10.1016/j.sab.2018.08.003.
27. Erdmann N, Kratz JV, Trautmann N, Passler G. Resonance ionization mass spectrometry of ion beam sputtered neutrals for element- and isotope-selective analysis of plutonium in micro-particles. Anal Bioanal Chem. 2009;395(6):1911–8. https://doi.org/10.1007/s00216-009-2906-6.
28. Erdmann N, Betti M, Kollmer F, Benninghoven A, Grüning C, Philipsen V, et al. Resonance and nonresonant laser ionization of sputtered uranium atoms from thin films and single microparticles: evaluation of a combined system for particle trace analysis. Anal Chem. 2003;75(13):3175–81. https://doi.org/10.1021/ac0264426.
29. Franzmann M, Bosco H, Walther C, Wendt K. A new resonant laser-SNMS system for environmental ultra-trace analysis: installation and optimization. Int J Mass Spectrom. 2017;423:27–32. https://doi.org/10.1016/j.ijms.2017.10.003.
30. Franzmann M, Bosco H, Hamann L, Walther C, Wendt K. Resonant laser-SNMS for spatially resolved and element selective ultra-trace analysis of radionuclides. J Anal Atom Spectrom. 2018;33(5):730–7. https://doi.org/10.1039/c7ja00423k.
31. Grüning C, Erdmann N, Huber G, Klopp P, Kratz JV, Kunz P, et al. A high repetition rate solid state laser system for resonance ionization mass spectrometry of actinides. AIP Conf Proc. 1998;454(1):285–8. https://doi.org/10.1063/1.57161.
32. Schönberg P, Mokry C, Runke J, Schönenbach D, Stöbener N, Thörle-Pospiech P, et al. Application of resonance ionization mass spectrometry for ultratrace analysis of technetium. Anal Chem. 2017;89(17):9077–82. https://doi.org/10.1021/acs.analchem.7b01778.
33. Grüning C, Huber G, Klopp P, Kratz JV, Kunz P, Passler G, et al. Resonance ionization mass spectrometry for ultratrace analysis of plutonium with a new solid state laser system. Int J Mass Spectrom. 2004;235(2):171–8. https://doi.org/10.1016/j.ijms.2004.04.013.
34. Trautmann N, Folger H. Preparation of actinide targets by electrodeposition. Nucl Instrum Meth A. 1989;282(1):102–6. https://doi.org/10.1016/0168-9002(89)90117-4.
35. Kaplan U, Amayri S, Drebert J, Rossberg A, Grolimund D, Reich T. Geochemical interactions of plutonium with Opalinus Clay studied by spatially resolved synchrotron radiation techniques. Environ Sci Technol. 2017;51(14):7892–902. https://doi.org/10.1021/acs.est.6b06528.
36. Van Loon LR, Soler JM, Bradbury MH. Diffusion of HTO, $^{36}Cl^-$ and $^{125}I^-$ in Opalinus Clay samples from Mont Terri. Effect of confining pressure. J Contam Hydrol. 2003;61(1–4):73–83. https://doi.org/10.1016/S0169-7722(02)00114-6.
37. Haas R, Lohse S, Düllmann CE, Eberhardt K, Mokry C, Runke J. Development and characterization of a drop-on-demand inkjet printing system for nuclear target fabrication. Nucl Instrum Meth A. 2017;874:43–9. https://doi.org/10.1016/j.nima.2017.08.027.
38. Tits J, Gaona X, Laube A, Wieland E. Influence of the redox state on the neptunium sorption by cementitious materials. In: Altmaier M, Kienzler B, Duro L, Grivé M, Montoya V, editors. 3rd Annual Workshop Proceedings of the Collaborative Project "Redox Phenomena Controlling Systems" (7th EC FP CP RECOSY): KIT Scientific Publishing, Karlsruhe; 2011. p. 163–75.
39. Raeder S, Stöbener N, Gottwald T, Passler G, Reich T, Trautmann N, et al. Determination of a three-step excitation and ionization scheme for resonance ionization and ultratrace analysis of Np-237. Spectrochim Acta B. 2011;66(3–4):242–7. https://doi.org/10.1016/j.sab.2011.02.002.
40. Savina MR, Isselhardt BH, Kucher A, Trappitsch R, King BV, Ruddle D, et al. High useful yield and isotopic analysis of uranium by resonance ionization mass spectrometry. Anal Chem. 2017;89(11):6224–31. https://doi.org/10.1021/acs.analchem.7b01204.
41. Young CE, Pellin MJ, Calaway WF, Jorgensen B, Schweitzer EL, Gruen DM. Laser-based secondary neutral mass-spectroscopy - useful yield and sensitivity. Nucl Instrum Meth B. 1987;27(1):119–29. https://doi.org/10.1016/0168-583x(87)90012-7.
42. Goeringer DE, Christie WH, Valiga RE. Investigation of matrix effects on the neutral fractions ejected from ion-bombarded, uranium-containing solids using resonance ionization mass

spectrometry. Anal Chem. 1988;60(4):345–9. https://doi.org/10.1021/ac00155a015.
43. München J, Lipinsky D, Arlinghaus HF. Signals of secondary ions and resonantly and nonresonantly ionized neutrals sputtered from binary alloys as a function of oxygen exposure. Surf Interface Anal. 2013;45(1):117–21. https://doi.org/10.1002/sia.5027.
44. Rangarajan S, Tyler BJ. Topography in secondary ion mass spectroscopy images. J Vac Sci Technol A. 2006;24(5):1730–6. https://doi.org/10.1116/1.2217980.
45. Kollmer F, Bourdos N, Kamischke R, Benninghoven A. Nonresonant laser-SNMS and TOF-SIMS analysis of sub-μm structures. Appl Surf Sci. 2003;203–204:238–43. https://doi.org/10.1016/S0169-4332(02)00635-9.
46. Bushaw BA, Raeder S, Ziegler SL, Wendt K. Triple-resonance autoionization of uranium optimized for diode laser excitation. Spectrochim Acta B. 2007;62(5):485–91. https://doi.org/10.1016/j.sab.2007.04.015.

Publication II: Investigation of plutonium diffusion profiles in Opalinus Clay rock via TOF-SIMS and rL-SNMS

Contribution statement

The author was the main investigator of this work. The novel sample preparation technique was developed in collaboration with Markus Breckheimer. The diffusion experiment as well as the TOF-SIMS and rL-SNMS measurements were performed with Christopher Sirleaf. The CE-ICP-MS measurement was conducted with Janik Lohmann. For the publication all data analysis, creating of visualizations, the writing of the original draft, as well as the revision process were conducted by the author. The publication contains a contribution statement:
F. Berg: Writing - Original Draft, Writing - Review & Editing, Visualization, Methodology, Conceptualization, Investigation, Formal analysis, Project administration. **C. Sirleaf:** Writing - Review & Editing, Investigation. **M. Breckheimer:** Writing - Review & Editing, Investigation, Conceptualization, Methodology. **J. Lohmann:** Writing - Review & Editing, Investigation. **T. Reich:** Writing - Review & Editing, Conceptualization, Methodology, Resources, Supervision, Project administration, Funding acquisition.

Copyright

Authors: Felix Berg, Christopher Sirleaf, Janik Lohmann, Markus Breckheimer and Tobias Reich
Publication: Applied Geochemistry
Publisher: Elsevier
Date: April 2025

Applied Geochemistry 183 (2025) 106332

Contents lists available at ScienceDirect

Applied Geochemistry

journal homepage: www.elsevier.com/locate/apgeochem

Investigation of plutonium diffusion profiles in Opalinus Clay rock via TOF-SIMS and rL-SNMS

Felix Berg *, Christopher Sirleaf, Janik Lohmann, Markus Breckheimer, Tobias Reich *

Johannes Gutenberg-Universität Mainz, Department of Chemistry - Nuclear Chemistry, 55099, Mainz, Germany

ARTICLE INFO

Editor - Xavier Gaona

Keywords:
Nuclear waste
Plutonium
Diffusion
Opalinus Clay
Resonant laser ionization
TOF-SIMS
rL-SNMS
CE-ICP-MS

ABSTRACT

The capability of the combined approach of time-of-flight secondary ion mass spectrometry (TOF-SIMS) and resonant laser secondary neutral mass spectrometry (rL-SNMS) for the analysis of diffusion samples of ^{242}Pu in Opalinus Clay (OPA) under aerobic conditions was investigated at the micrometer scale. The speciation of Pu in the diffusion reservoir with OPA pore water (pH 7.6) was determined as PuO_2^+ using capillary electrophoresis coupled to inductively coupled plasma mass spectrometry (CE-ICP-MS). Using modern 3D printing techniques, a simple and easily scalable experimental setup was developed and adapted to the requirements of TOF-SIMS and rL-SNMS. Together, these techniques allowed for the observation of the pristine diffusion profile of Pu while retaining information about the heterogeneous clay rock. For the experiment with 35 days of in-diffusion, the modeling of an averaged diffusion profile of approximately 300 μm length resulted in $D_a = 3.2(4) \times 10^{-15}\ m^2\ s^{-1}$. TOF-SIMS and rL-SNMS mappings showed heterogeneous distributions of Pu inside the clay rock and correlations with the matrix elements Fe and Ca, pointing to pyrite and a cementing calcite phase as reactive mineral phases.

1. Introduction

Due to the long half-life of its isotopes, their high radiotoxicity and vast aqueous chemistry with multiple oxidation states possibly present at the same time, the trans-uranium element plutonium (Pu) is of major interest for the safety case for nuclear waste storage of high-level radioactive waste (HLW) (Geckeis et al., 2019). Many countries with a current or former nuclear energy program plan for the safekeeping of HLW in a deep geological repository (DGR) using a multi-barrier concept with a combination of (geo-)technical and geological barriers. The latter is of particular significance since the man-made measures are not expected to last for the total storage time required for HLW of up to one million years (Bundesgesetzblatt, 2017). Since no experimental data for a potential construction site of a DGR under investigation can be obtained over such a long period, the safety case then rests on models that are predicting the behaviour of the radioactive inventory and its interactions with the different barrier components using parameters retrieved in laboratory experiments. It is therefore vital to study the (geo-)chemical interactions of radionuclides as closely as possible and gain an in-depth knowledge about the underlying processes. Possible host-rock formations considered due to their unique favourable properties for a DGR are rock salt, crystalline and clay rocks. Many European countries are researching or already planning to build their DGR in clay rock (Preter, 2023; Andra, 2022; Nagra, 2022), for which, among others, Opalinus Clay (OPA) is a potential candidate. OPA and other clay rocks in general provide reducing conditions which are considered favourable for fission products and actinides such as Pu since their reduced species show less mobility (Churakov et al., 2020). However, still many questions remain concerning the stability of the reducing environment, the kinetics and the redox active components, i.e. the minerals (Maes et al., 2024). For this reason, the chemical interactions of various radionuclides and OPA have already been the subject of extensive research efforts in a wide variety of experiments (Wu et al., 2009; Joseph et al., 2013; Montavon et al., 2022). The insights and parameters retrieved for sorption and migration are usually averaged over the bulk material: for example, distribution coefficients are regularly obtained from batch sorption experiments with OPA suspensions. Samples from diffusion studies are often analyzed via abrasive peeling (Van Loon and Müller, 2014). Therefore, any information about the exact processes and various mineral phases possibly involved in the retention of a radionuclide, i.e. the microstructure, is lost. A spatially resolved approach would allow to gain further insight into the underlying processes.

Time-of-flight secondary-ion mass spectrometry (TOF-SIMS) is a technique for the spatially resolved analysis of surfaces at the micrometer or even nanometer scale: a pulsed primary ion (PI) beam is scanned

* Corresponding authors.
E-mail addresses: feberg@uni-mainz.de (F. Berg), treich@uni-mainz.de (T. Reich).

https://doi.org/10.1016/j.apgeochem.2025.106332
Received 29 October 2024; Received in revised form 21 February 2025; Accepted 22 February 2025
Available online 8 March 2025

over the sample, creating secondary ions (SIs) which are subsequently analyzed by their mass-to-charge ratio (m/z) in a TOF-MS. This way, a full mass spectrum is retrieved for every position sampled. By comparing the relative intensities of a mass peak for the various positions, the qualitative distribution of said mass on the sample's surface is mapped, which allows for conclusions about the surface's composition. One major drawback of TOF-SIMS is the possibility of isobaric interferences, especially if the concentration of analyte is as low as in the far-field of a DGR. Resonance ionization mass spectrometry (RIMS) is a highly sensitive and selective analytical technique that is able to address this shortcoming. Here, atomic species are photo-ionized via laser light in a multi-step excitation scheme, using the unique electronic structure of every element. Isotopes are then usually separated in a mass analyzer. Depending on the element and the excitation scheme, the selectivity can be further enhanced by tuning the lasers according to the optical isotope shift, i.e. small differences in the electronic level energies due to the variations in the structure of the nucleus and its interactions with the electrons. During the sputter process in the TOF-SIMS, only a fraction of the sample material is released as SIs. A lot of material is sputtered as secondary neutrals (SNs) which are usually lost for analysis (Benninghoven et al., 1993). By combining TOF-SIMS and RIMS to resonant laser secondary neutral mass spectrometry (rL-SNMS), these SNs become available for analysis and allow for confirmation that the signal observed is indeed the element in question since it is possible to record the background in rL-SNMS by tuning the lasers off resonance, which is not possible with TOF-SIMS (Bosco et al., 2021; Schönenbach et al., 2021; Raiwa et al., 2022; van Eerten et al., 2023). It is important to note that neither TOF-SIMS nor rL-SNMS can directly quantify an analyte without an externally calibrated standard with the exact same sample matrix as reference. Without such a reference material only qualitative comparisons can be made.

In this work, TOF-SIMS and rL-SNMS were applied for the study of the diffusion of Pu in OPA for the first time. The goal was to showcase and evaluate the capability of the combination of both methods to retrieve the diffusion profile of Pu while at the same time preserving the sample matrix and observing the geochemical interactions of the radionuclide with the various mineral phases present in OPA at the micrometer scale. To achieve this, a new workflow for simple and fast diffusion sample preparation tailored to TOF-SIMS and rL-SNMS was developed. For further insight into the complex redox chemistry behaviour of Pu, its oxidation state in the OPA pore water diffusion reservoir was analyzed using capillary electrophoresis coupled to an inductively coupled plasma mass spectrometer (CE-ICP-MS).

2. Materials and methods

2.1. Sample preparation

Cylindrical samples of aerobic OPA ($\varnothing = 5$ mm, $L \approx 15$ mm) were CNC milled dry from larger chunks of bulk OPA (D25 (L11), Mont Terri Rock Laboratory, St-Ursanne, Switzerland) under atmospheric conditions. All further sample preparations were conducted in a fume hood open to ambient air. The cylinders were embedded into custom PMMA sample holders using a slow curing epoxy resin (EpoxiCure™ 2, Buehler, Lake Bluff, Illinois, USA) with the natural bedding of the OPA perpendicular to the in-diffusion contact surface (compare Fig. 1 a & b) and placed in contact with artificial aerobic OPA pore water (OPA-PW) with an ionic strength of approximately 0.39 mol L^{-1} prepared after Pearson (1998) to re-saturate the material and allow it to swell (for the exact composition compare supporting information Table S1). To note, in this step the samples were not hung in the reservoir with the contact surface facing down, but laid on their long side to avoid air entrapment.

After a minimum contact time of 10 d, the contact surface was wet-sanded flat. The OPA samples were then stored in OPA-PW until use for an experiment. No alterations were observed even after three months. The ^{242}Pu(VI) stock solution was prepared by evaporating a ^{242}Pu solution three times with 5 mL of 1 mol L^{-1} $HClO_4$ under heat until near dryness before the residue was picked up in 3 mL of 1 mol L^{-1} $HClO_4$. The Pu oxidation state was then confirmed via UV–VIS (TIDAS 100, J & M Analytik AG, Germany). The concentration of the ^{242}Pu(VI) stock solution ($1.4(8)\times10^{-3}$ mol L^{-1}) was calculated from the absorption band for Pu(VI) at 830 nm using the molar decadic extinction coefficient $\epsilon = 555$ L mol^{-1} cm^{-1} (Clark et al., 2008). An aliquot of the freshly prepared stock solution was then added to 50 mL of OPA-PW (pH 7.7(1), Eh = 650(10) mV (SHE)) to achieve a concentration of 5×10^{-6} mol L^{-1} ^{242}Pu(VI) in a standard laboratory flask (100 mL laboratory bottle, narrow neck, with screw cap, VWR International, Leuven, Belgium). An aliquot of 100 µL of a 1.5 mol L^{-1} NaN_3 solution was added to the reservoir to prevent bacterial or algae growth. The pH was measured using an inoLab© pH 720 meter (WTW© a Xylem brand, Weilheim, Germany) and an SI Analytics™ BlueLine 16 pH micro-electrode (SI Analytics™ a Xylem brand, Mainz, Germany) filled with 3 mol L^{-1} NaCl solution. The pH meter was calibrated using buffer solutions at pH 6.87 (Schott Instruments, L4790) and pH 9.18 (Certipur®, Merck KGaA, Darmstadt, Germany). For Eh measurements a Pt ring electrode with 3 mol L^{-1} KCl (6.0451.100, METROHM Prozessanalytik GmbH & Co. KG, Filderstadt, Germany) was used. The electrode was tested using a redox buffer solution (Eh = 640 mV (SHE), SI Anlytics™ a Xylem brand, Mainz, Germany). The ^{242}Pu concentration in the OPA-PW was monitored via liquid scintillation counting (LSC; HIDEX 300SL, Hidex Oy, Turku, Finland; cocktail: ULTIMA GOLD™ XR, revvity Germany GmbH, Hamburg, Germany) for the duration of the experiment. The reservoir was sampled for LSC measurements in aliquots of 10 µL (until day 17) and 20 µL (until day 35) of the experiment. After an equilibration time of about seven days, when the Pu concentration and pH were constant, five OPA samples were placed into the solution for up to 35 d under aerobic conditions using a custom designed 3D printed insert out of polylactic acid (PLA) (see SI Figure S1). The diffusion cores were taken out of the reservoir after 21, 25, 28 (2 samples) and 35 d, respectively, of which four samples (one for each time interval) were analyzed via TOF-SIMS and rL-SNMS. The samples were directly split by notching the PMMA sample holder parallel to the natural OPA bedding with a saw and applying as little force as possible with a scalpel to split the

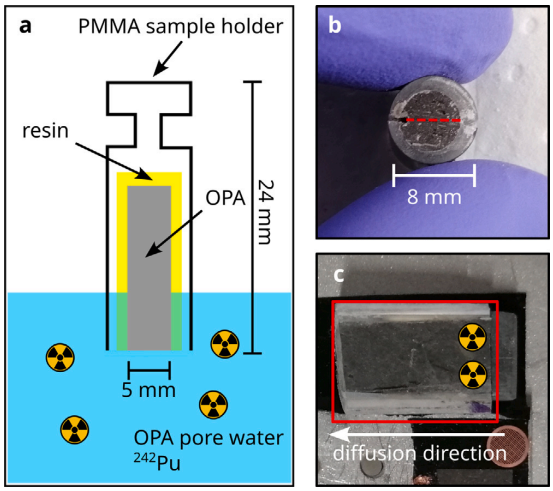

Fig. 1. **a** Schematic of diffusion sample in contact with the pore water solution containing ^{242}Pu. **b** View of the contact surface of a notched diffusion sample. The red line indicates the natural bedding of the OPA along which the sample is then split to allow access to the diffusion profile. **c** Top view of a split diffusion core mounted on a TOF-SIMS sample holder via carbon tape (red square). The Pu diffused into the material from the right edge of the sample and was observed via TOF-SIMS and rL-SNMS.

OPA core (see Fig. 1 b). This allowed for access to a pristine surface unaltered by saw marks and with relatively low topography which is favourable for both TOF-SIMS and rL-SNMS (see Fig. 1 c). The samples were then dried for a minimum of one day in a glove box under Ar atmosphere before being transferred into the TOF-SIMS instrument.

2.2. TOF-SIMS and rL-SNMS

The TOF-SIMS instrument used in this work is a commercial TOF-SIMS III (iontof GmbH, Münster, Germany) with the controls upgraded to TOF-SIMS V level including a USB-TDC as well as the iontof Surface Lab 6.6 control and analysis software. The custom titanium:sapphire (Ti:sa) laser system consists of three tunable Ti:sa lasers jointly pumped with circa 45 W at 10 kHz by a frequency-doubled neodymium:yttrium aluminum garnet (Nd:yag) laser (DM532-60, Nexlase GmbH, Gröbenzell, Germany). TOF-SIMS and laser system timings were synchronized for rL-SNMS measurements via a frequency generator (modell 577, BNC, San Rafael, USA). The wavelength of the lasers was monitored quasi-simultaneously by a wavemeter equipped with a switch (WS6-200, Highfinesse, Tübingen, Germany). The laser light was transported to the TOF-SIMS via a multi-mode optical fiber and introduced into the analysis chamber via a view port. The setup has been described in more detail in a previous publication (Schönenbach et al., 2021). The samples were attached via carbon tape to a sample holder and transferred into the TOF-SIMS. The vacuum was $<1 \times 10^{-7}$ mbar during measurements. For TOF-SIMS the field of view (FOV) of 500 µm × 500 µm was scanned 50 times with 512^2 px resolution with one PI shot per pixel. For rL-SNMS the same FOV was scanned 20 times with 256^2 px resolution and ten PI shots per pixel. For the first diffusion sample extracted after 21 d, four non-overlapping FOV were recorded, but only one showed sufficient Pu signal to measure rL-SNMS. For the second sample (25 d) five FOVs, for the third sample (28 d) seven FOVs and for the fourth sample after 35 d, six FOVs were analyzed. For the resonant photo-ionization the three step scheme by Grüning et al. (2004) was used. Laser powers were measured (PowerMax© model PM3 with Fieldmate powermeter, Coherent GmbH, Göttingen, Germany) directly after the fiber before the view port of the TOF-SIMS and were usually around 40 mW for the first excitation step (FES), approximately 400 mW for the second excitation step (SES) and 650 mW for the ionizing step (IS).

2.3. CE-ICP-MS

The electrophoresis measurements to determine the oxidation state of Pu in aerobic OPA-PW were conducted using an Agilent 7100 CE (Agilent Technologies Deutschland GmbH, Waldbronn, Germany) coupled to an Agilent 7900 ICP-MS (Agilent Technologies Deutschland GmbH, Waldbronn, Germany). The CE apparatus was coupled to the ICP-MS using a MiraMist CE nebulizer (Burgener Research, Mississauga, Canada) and a Scott-type spray chamber (AHS Analysentechnik, Tübingen, Germany). A fused silica capillary with 50 µm inner diameter and 50 cm length was used (Polymicro Technologies, Phoenix, Arizona, USA). A voltage of 10 kV was applied to the capillary. The setup and measurement procedure have been described in detail in a previous publication (Willberger et al., 2019). To determine the oxidation state, aliquots of the OPA-PW solution with ^{242}Pu were spiked with 2-bromopropane as electroosmotic flow (EOF) marker. In addition, samples of ^{237}Np(V) in OPA-PW (ca. 1×10^{-7} mol L^{-1}) were prepared the same way and analyzed via CE-ICP-MS for comparison. The electrophoretic mobility μ_e was calculated from the retention times of the analyte (t) and the EOF marker (t_{EOF}) as well as the length of the capillary (L) and the applied voltage (U) according to Eq. (1) (Willberger et al., 2019):

$$\mu_e = \frac{L^2}{U} \cdot \left(\frac{1}{t} - \frac{1}{t_{\mathrm{EOF}}} \right), [\mu_e] = \frac{\mathrm{m}^2}{\mathrm{V} \cdot \mathrm{s}}. \quad (1)$$

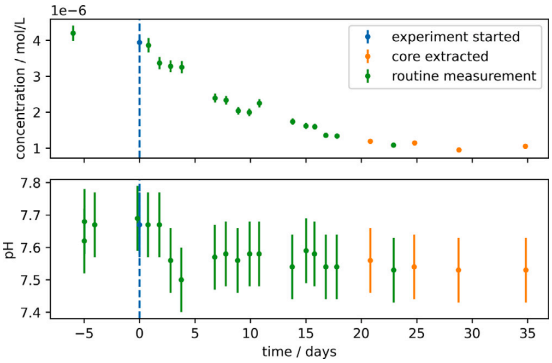

Fig. 2. Concentration of ^{242}Pu monitored by LSC in the reservoir (V = 50 mL) for the duration of the diffusion experiment and the measured pH. To ensure a stable Pu concentration in the reservoir, a measurement was performed before the addition of the diffusion cores and the start of the experiment indicated by the blue dashed line. A reduction of Pu concentration in solution by a factor of 4 is observed 35 d after starting the experiment with most of the decrease happening within 21 d of in-diffusion. The pH of the OPA-PW solution was at around 7.6 for the whole duration of the experiment. Four diffusion samples were analyzed after 21, 25, 28 and 35 days of contact time, respectively, via TOF-SIMS and rL-SNMS.

3. Results and discussion

3.1. Analysis of the OPA-PW diffusion reservoir

As shown in Fig. 2, immediately after inserting the OPA diffusion samples, the ^{242}Pu concentration of the reservoir decreased and stabilized after approximately 21 d, indicating an initial high uptake of Pu by the samples. The pH of the reservoir solution remained nearly constant for the whole duration of the experiment, with only a slight drop of 0.1 pH units 3 d into the experiment.

The trend is comparable to previous diffusion experiments with Np(V) and OPA (Wu et al., 2009; Fröhlich et al., 2013). The Eh of the solution reduced from initially 650(10) mV to 480(20) mV (SHE) after 35 days. Figure 3 displays the Pourbaix diagram for the system presented here, including the two Eh measurements at the beginning (orange) and after the end of the experiment (blue). Since this experiment was conducted under oxidizing conditions, the values are higher than in the reducing conditions in the host rock: Field measurements in different OPA boreholes in Mont Terri resulted in Eh values between −120 mV to 140 mV (SHE) (Pearson et al., 2003).

The theoretical calculation for the diffusion system suggests that in the beginning the majority of Pu was present as $PuO_2^+(aq)$ but with the change of the Eh $Pu(OH)_4(aq)$ should be the dominating species. In order to evaluate the oxidation state of Pu in the reservoir at the end of the experiment, CE-ICP-MS measurements of an aliquot of the reservoir OPA-PW solution were performed. Figure 4 shows the electrophoretic mobility determined via CE-ICP-MS for ^{242}Pu and ^{237}Np in OPA-PW, with the sample for ^{242}Pu taken from the diffusion reservoir used in this study after the experiment had ended. Both isotopes are displaying the same positive μ_e, suggesting that they are present in OPA-PW as similar chemical species, despite having different initial oxidation states (^{242}Pu: VI and ^{237}Np: V) when they were added initially to OPA-PW under aerobic conditions.

Since Np is stable as $NpO_2^+(aq)$ under these conditions, this suggests that Pu is present as $PuO_2^+(aq)$ in the reservoir solution. As mentioned above, the Pourbaix diagram for the system suggests as well that under the initial conditions of the contact solution (pH 7.7(1), Eh = 650(10) mV (SHE)) the majority of Pu should be Pu(V). However, the theoretical calculations would predict Pu(IV) to be the dominating species for the Eh = 480(20) mV measured after finishing the diffusion experiment,

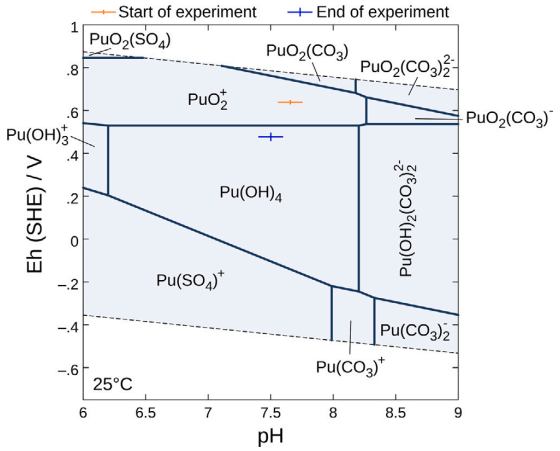

Fig. 3. Pourbaix diagram of 4×10^{-6} mol L^{-1} Pu in OPA-PW under aerobic conditions. Calculated using The Geochemist's Workbench® 2023 Community Edition, Release 17.0.3 and the Thermochimie Database v12a (Giffaut et al., 2014). Composition of OPA-PW according to Pearson (1998) without Sr. A concentration of 420 ppm CO_2 in the atmosphere was assumed. Mineral phases were suppressed since no precipitation was observed during the experiment. The Eh and pH measured in the ^{242}Pu containing OPA-PW contact solution before the start of the experiment (pH 7.7(1), Eh = 650(10) mV (SHE)) and at the end of the experiment (pH 7.6(1), Eh = 480(20) mV (SHE)) after 35 days are shown in orange and blue, respectively.

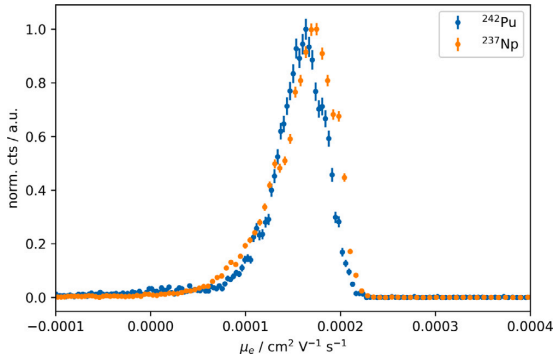

Fig. 4. Comparison of the electrophoretic mobilities (μ_e) of ^{237}Np (initial ox. state V) and ^{242}Pu (initial ox. state VI) in OPA-PW at pH 7.6(1), Eh = 480(20) mV (SHE). Since Pu is displaying the same μ_e as Np(V) which is stable as $NpO_2^+(aq)$ under these conditions, it follows that also Pu exists as $PuO_2^+(aq)$ in the OPA-PW reservoir.

but Pu(IV) was not detected in the CE-ICP-MS measurement. Possible explanations include the decreased solubility of $Pu(OH)_4$ compared to PuO_2^+ for pH 7.6(1) (Neck et al., 2007) below the detection limit of the CE-ICP-MS system or increased sorption of Pu(IV) to the sample or reservoir surfaces since no precipitation was observed either by visual inspection or in the CE-ICP-MS measurements. CE-ICP-MS is sensitive to the presence of colloids or precipitation and no centrifugation of the sample was necessary to obtain an analyte signal free of interferences. Our result suggests that Pu(VI) was reduced to Pu(V) in OPA-PW in the experiment's reservoir under aerobic conditions at pH 7.6 and was present predominantly as PuO_2^+. A recent study by Kaplan et al. (2024) on Pu(V) diffusion in OPA using X-ray absorption fine structure spectroscopy (XAFS) showed that Pu(V) was subsequently reduced to the less mobile oxidation and stronger sorbing state Pu(IV) inside the clay rock with the relative amount of Pu(V) decreasing with increasing

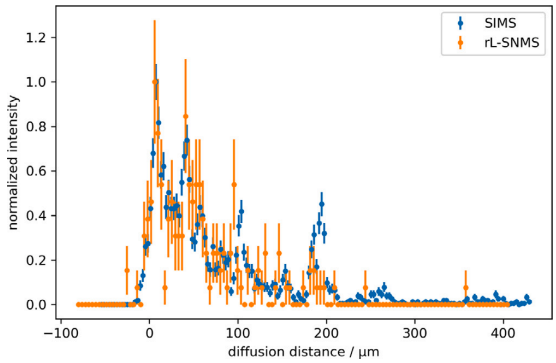

Fig. 5. Diffusion profiles extracted from the distributions of Pu obtained via TOF-SIMS (the sum of $^{242}Pu^+$ and $^{242}PuO^+$) and rL-SNMS (Pu^+) in Fig. 6 for a single FOV with 500 μm × 500 μm. The profiles were obtained by summing up the signal intensity in each row along the direction of the diffusion in the distribution for the respective masses. Both profiles show intensity spikes which are the result of areas with increased intensity in the Pu distributions. The data has been binned with a binning increment of two. Error bars are calculated as $\sigma = \sqrt{N}$ with N the number of events detected.

diffusion depth. At this point, further studies via CE-ICP-MS are necessary to determine the kinetics of the formation of Pu(V) from Pu(VI) and the role of Pu(IV) in the OPA-PW reservoir solution.

3.2. TOF-SIMS and rL-SNMS measurements of the Pu diffusion profile

During analysis, no significant differences between the first three samples removed from the reservoir after 21 d, 24 d and 28 d with regard to diffusion depth and distribution of Pu were observed. Therefore, the discussion is focused on the two samples in contact with Pu for 21 d and 35 d, respectively.

Figure 5 shows the Pu diffusion profiles retrieved via TOF-SIMS and rL-SNMS for a single FOV with 500 μm × 500 μm from the first sample extracted after 21 d of contact time. The profile is generated from the respective distribution image for Pu shown in Fig. 6 by summing the intensity of each row parallel to the sample interface, thereby constructing the profile along the diffusion direction into the sample.

Both TOF-SIMS and rL-SNMS profiles show that more ^{242}Pu is located near the interface of solution and OPA and the overall signal decreases with increasing depth. ^{242}Pu migrated approximately 280 μm into the sample within 21 d, which is comparable to the literature (Kaplan et al., 2024). However, the diffusion profiles include spikes in the signal which have not been reported from comparable experiments using abrasive methods.

Figure 6 displays the total ion image and Ca^+ distribution for a 500 μm × 500 μm area at the interface of the OPA sample and the contact solution indicated by the dashed white line as well the distribution of Pu observed via TOF-SIMS and rL-SNMS from which the profiles in Fig. 5 were generated. The total ion image gives a general idea of the topography and microstructure of the sample. Although the sample was split parallel to its natural bedding, it still displays differences in height, with lower areas showing a reduced signal and therefore topographic interferences of the signal cannot be fully excluded and need to be taken into account. As already established in the description of the profile, both TOF-SIMS and rL-SNMS show a higher abundance of Pu towards the edge of the sample and interface with the OPA-PW indicated by the dashed white line (see Fig. 6) as well as a decrease in signal with increasing diffusion depth. But, similar to Ca^+, Pu has a heterogeneous distribution in contrast to other elements such as Si or K (see SI Figure S2) and shows areas of high intensity or 'hot spots', that cannot be explained by the topography and which are the origin of

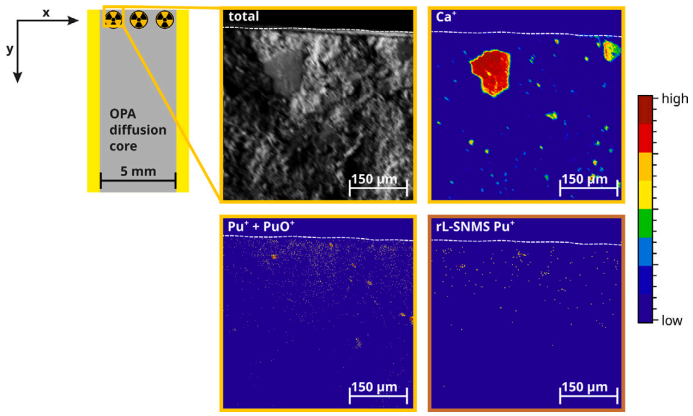

Fig. 6. Total ion image (top left) and Ca^+ (m/z = 40 u, top right), as well as the distributions of Pu^+ plus PuO^+ (m/z = 242 u and 258 u, bottom left) observed via TOF-SIMS compared to Pu^+ detected by rL-SNMS (m/z = 242 u, bottom right) in a 500 µm × 500 µm measured window on an OPA diffusion core in contact after 21 d. The white dashed line indicates the interface of the sample and the ^{242}Pu spiked OPA-PW solution. The direction of diffusion is parallel to the y-axis. TOF-SIMS was measured with 512^2 px resolution, rL-SNMS with 256^2 px. The rL-SNMS signal for Pu is significantly smaller than the sum of Pu^+ and PuO^+ for a comparable measurement time, suggesting the resonant photo-ionization of Pu is less efficient. Nevertheless, a resonant signal is observed. Additional matrix element distributions observed by TOF-SIMS can be found in SI Figure S2.

the deviations from a smooth diffusion profile observed in Fig. 5. Additionally, in some areas of high Ca^+ intensity, that can be attributed to calcite when looking at the microstructure visible in the total ion image, the Pu signal is reduced. In general, both TOF-SIMS and rL-SNMS show the same distribution, but the total ion signal for $^{242}Pu^+$ detected by rL-SNMS is lower compared to TOF-SIMS. First, this can be explained that using TOF-SIMS $^{242}Pu^+$ and $^{242}PuO^+$ can be observed, whereas for rL-SNMS only $^{242}Pu^+$ is detected. Second, with the current laser setup no signal saturation is reached in the IS, resulting in only partial ionization of available ions (Schönenbach et al., 2021). In addition, only Pu sputtered as neutral species is available for being resonantly ionized from the ground state, so a possible explanation would also be that the percentage of sputtered neutrals might be reduced for this type of matrix. Here, further investigations are necessary. However, despite the lower intensity, rL-SNMS allows in its current development state to confirm the distribution retrieved via TOF-SIMS and gives a direct method to attribute the signal for m/z = 242 u to $^{242}Pu^+$.

Figure 7 (top right) shows the Pu distribution observed via TOF-SIMS in a representative FOV for the fourth diffusion sample extracted after 35 d of being in contact with the ^{242}Pu containing reservoir solution.

Also here, the diffusion profile (see SI Figure S4) and the distribution image indicate similar areas of increased ^{242}Pu signal that are not explained by the topography shown in the total ion image. Upon comparison with other elements, a correlation between the Pu^+, PuO^+, Fe^+ and Ca^+ for the 'hot spots' is observed (Fig. 7 bottom). To note, in some areas for Ca^+ an anti-correlation with Pu as discussed for the previous sample (Fig. 6) can also be identified. These observations are also confirmed by scatter plots Fig. 8 of the normalized intensities for Fe^+, Ca^+ and the sum of Pu^+ and PuO^+ for the magnified FOVs shown in Fig. 7, bottom row.

The intensity for the combined Pu signal of Pu^+ and PuO^+ is correlated with Fe^+ (compare Fig. 8 **a**). Also for the intensity of the Ca^+ signal there is a correlation with Pu, but an increased signal of Ca^+ does not lead to an increase in Pu (Fig. 8 **b**). The scatter plot for the signal intensity of Fe^+ and Ca^+ (Fig. 8 **c**) also suggests an influence on the Fe^+ signal by the presence of Ca^+. However, also here a high Ca^+ intensity does not cause a high Fe^+ signal. As mentioned before this confirms the observation of areas with a high Ca^+ intensity in the mapping shown in Fig. 7 that have no co-localization with Pu or Fe.

For the areas with a positive correlation, an isobaric interference between CaO^+ and Fe^+ was excluded by comparing the ratio $^{54}Fe^+/^{56}Fe^+$

Table 1
$^{54}Fe^+/^{56}Fe^+$ ratios observed for the 'hot spots' in Fig. 7. The ratio agrees with the literature and therefore it is unlikely that isobaric interferences of CaO^+ are observed on mass 56 u.

Position no.	$^{54}Fe^+/^{56}Fe^+$
1	0.063(5)
2	0.071(17)
3	0.061(11)
4	0.066(12)
5	0.062(9)
De Laeter et al. (2003)	0.0637(11)

for the positions 1–5 (compare Fig. 7 bottom) on the sample's surface that is in excellent agreement with the literature value 0.0637(11) (De Laeter et al., 2003) (see Table 1) for the natural isotopic ratio of $^{54}Fe^+$ and $^{56}Fe^+$.

At this point of the method development and due to instrumental limitations, it is not possible to identify the mineral phases involved via TOF-SIMS and rL-SNMS. Fe bearing minerals in OPA include for example siderite, illite and pyrite. The mineral pyrite (FeS_2) has already been indicated in literature as one potential mineral phase of OPA that is involved in the retention of radionuclides (Fröhlich et al., 2012; Reich et al., 2016; Kaplan et al., 2017). Pyrite is present in clay rocks as sub-mm-sized aggregates (Greer, 1978; Wang et al., 2013) associated with a cementitious calcite phase (Lerouge et al., 2014; Breckheimer et al., 2023), which could explain the observed correlation with Ca^+. Unfortunately, due to the isobaric interference of O_2^- on mass 32 u and an increased background on non-conducting samples, it was not possible to detect ^{32}S or other isotopes of S in negative ion mode TOF-SIMS. Furthermore, the influence of the so-called matrix effect, i.e. changes in the sputter rate of the different elements due to the chemical surrounding, cannot be excluded. Additional information from other chemical imaging techniques such as μ-XRD or μ-XRF could provide answers in the future. This is also true for the oxidation state of the Fe in the iron bearing mineral. Due to the aerobic nature of the OPA sample and the experiment, at least partial oxidation and therefore changes in the redox behaviour, especially towards the interface of the sample, have to be assumed. Here, XANES and XRD measurements at a synchrotron facility could provide further insights. In general, no differences in the distribution of Pu were observed between the two samples (21 d and 35 d of contact time with Pu, respectively) discussed

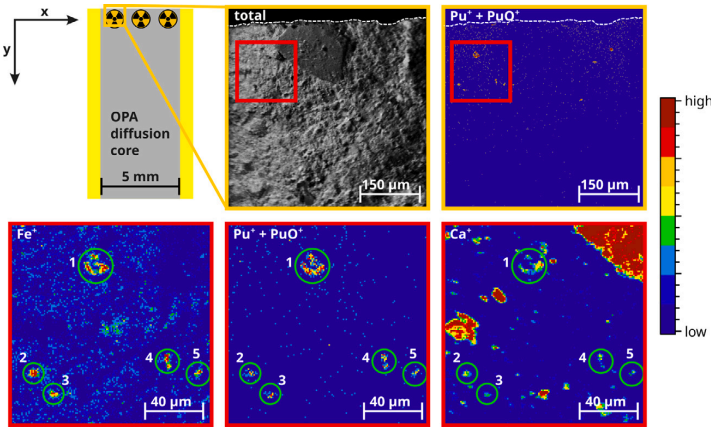

Fig. 7. Total ion image and Pu^+ plus PuO^+ (m/z = 242 u and m/z = 258 u) distributions as observed by TOF-SIMS on an OPA diffusion sample after 35 d (top row). Also in this sample 'hot spots' of Pu are observed. For the area marked by the red square, the distributions of Fe^+ (m/z = 56 u), Pu^+ and PuO^+ as well as Ca^+ (m/z = 40 u) are displayed as magnifications (bottom row). Here, a correlation between all three masses is observed for the Pu 'hot spots'. To rule out an isobaric interference by CaO^+ on the same mass as Fe^+, the areas 1–5 marked by green circles have been analyzed for the $^{54}Fe^+/^{56}Fe^+$ ratio (see Table 1) which is in excellent agreement with the literature value 0.0637(11) (De Laeter et al., 2003). FOV: 500 µm × 500 µm, 512^2 px. Additional matrix element distributions observed by TOF-SIMS can be found in SI Figure S3.

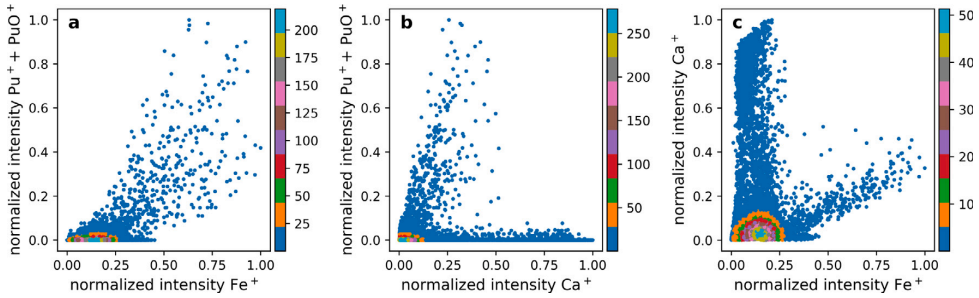

Fig. 8. Normalized intensity scatter plots of $Fe^+/(Pu^+ + PuO^+)$ **(a)**, $Ca^+/(Pu^+ + PuO^+)$ **(b)** and Fe^+/Ca^+ **(c)** for the FOVs displayed in the bottom row of Fig. 7. The intensity scatter plots were generated by applying a Gaussian filter with $\sigma = 1$ to the normalized 140^2 px raw data matrix for the respective mass peaks using custom scripts. The color scale indicates point density and was retrieved via a Gaussian kernel density estimate (Virtanen et al., 2020) of the filtered data matrix.

and only a slight increase of the diffusion depth of around 20 µm and an overall increase of Pu signal intensity was noted. It is also important to mention that since the splitting of the sample is done along the natural bedding, it might separate along a weakened natural potential fracture layer and therefore greater and faster diffusion is observed.

3.3. Modeling of an averaged diffusion profile

Since for the fourth diffusion sample placed in contact with Pu for 35 d six different 500 µm × 500 µm FOVs with sufficient Pu signal were measured via TOF-SIMS, it is possible to average over all six profiles and therefore minimize the influence of the 'hot spots' already discussed. This yields a profile that is comparable to the ones retrieved via classic abrasive peeling. A novel workflow using custom python scripts for the registration of the edges of each profile and averaging was developed. Since TOF-SIMS does not allow for direct quantification of the analyte signal, a dimensionless approach such as the solution of Fick's law shown in Eq. (2) by Yaroshchuk and Van Loon (2008) is required. This allows to use the signal intensity of the TOF-SIMS measurement directly.

$$c(\xi_*, \tau_*) = exp(\xi_* + \tau_*) \cdot erfc\left(\sqrt{\tau_*} + \frac{\xi_*}{2 \cdot \sqrt{\tau_*}}\right). \quad (2)$$

The diffusion normalized diffusion depth ξ is calculated from the diffusion depth x and the length l_* according to Eq. (3) with α the rock capacity factor, the reservoir volume V and the contact surface area of the OPA diffusion core S:

$$\xi_* = x/l_* \text{ with } l_* = \frac{V}{\alpha \cdot S}. \quad (3)$$

The normalized diffusion time τ_* is calculated according to Eq. (4) via the diffusion time t, α, the effective diffusion coefficient D_e, as well as the before mentioned V and S:

$$\tau_* = \frac{t}{t_*} \text{ with } t_* = \frac{1}{\alpha \cdot D_e} \cdot \left(\frac{V}{S}\right)^2. \quad (4)$$

Under the assumption that the maximum counts cts_{max} for Pu observed via TOF-SIMS directly at the interface correlate with the concentration of Pu in the reservoir, the intensity of the TOF-SIMS signal is normalized to cts_{max}. It is important to note that this model does not account for changing concentration in the reservoir and for redox processes inside the sample. An additional assumption required is that the 'rising edge' at the sample interface is an artifact of the TOF-SIMS measurement and not a Pu wavefront moving into the sample. This is the prerequisite for excluding these data points from the fit since the model cannot account for such a shape. For this reason it needs to be stressed that the diffusion coefficient D_e and the rock capacity factor α retrieved from the fit are only a rough approximation but nevertheless an important showcase for the potential to model a diffusion profile observed via TOF-SIMS. Further work and more advanced diffusion models are necessary to reach the full potential of the data. The fit was

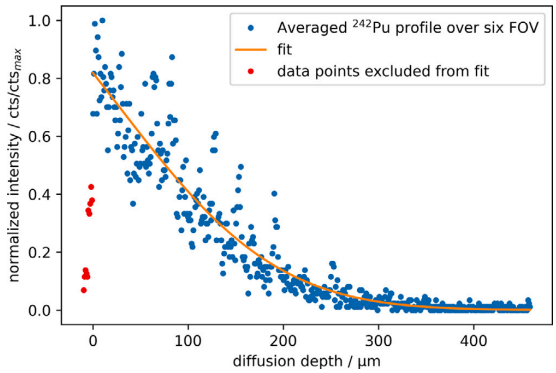

Fig. 9. Fit of the averaged Pu diffusion profile for the fourth diffusion sample (35 d). A total of six separate 500 µm × 500 µm FOV were measured via TOF-SIMS along the interface of the OPA diffusion core. The obtained profiles were aligned and averaged.

Table 2
Constants and fit parameters retrieved for the fit of an Pu diffusion profile obtained by averaging over six FOVs measured by TOF-SIMS (Fig. 9) using the model in Eq. (2).

Parameter	Value
V / m^3	5×10^{-5}
S / m^2	1.96×10^{-5}
t / s	3 024 000
D_e / m^2 s^{-1}	$1.6(2) \times 10^{-11}$
α / –	4853(358)
D_a / m^2 s^{-1}	$3.2(4) \times 10^{-15}$

performed using custom python scripts and the lmfit package (Newville et al., 2024). Figure 9 shows the averaged diffusion profile and the fit to Eq. (2). The individual profiles for each of the six FOVs averaged are shown in the SI Figure S5.

Despite the already discussed restrictions of the model, it is able to reproduce the data. The main difficulty is to locate the beginning of the profile since the fit does not start at the highest intensity at the beginning of the profile. In addition, spikes in signal intensity originating from intensity spikes in the individual profiles are still visible, but their significance is reduced. The used constants and retrieved diffusion parameters are listed in Table 2. The apparent diffusion coefficient D_a was calculated from D_e/α.

The model results in $D_e = 1.6(2) \times 10^{-11}$ m^2 s^{-1} and a capacity factor of $\alpha = 4853(358)$ for this dataset. Using Eq. (5) (Yaroshchuk and Van Loon, 2008) and typical literature values for the porosity ϵ (0.15(1) Wu et al., 2009; Joseph et al., 2013) and density ρ (≈2400 kg m^{-3} Wu et al., 2009; Joseph et al., 2013) of OPA, a theoretical distribution coefficient R_d of approximately 2.4 m^3 kg^{-1} for Pu in OPA can be calculated.

$$\alpha = \epsilon + (1 - \epsilon) \cdot \rho \cdot R_d. \quad (5)$$

However, these values have only a very limited significance due to the strong correlation of α and D_e (C(α, D_e) = 0.94). The apparent diffusion coefficient D_a is a more reliable parameter, since already small changes to the dataset, e.g. binning, influence D_e and α, but their ratio D_a is constant within the margin of error (compare SI Figure S6 and Table S2). When compared to literature, the retrieved D_a(Pu) = $3.2(4) \times 10^{-15}$ m^2 s^{-1} is smaller in relation to experiments with other actinides, such as U(VI) (D_a(U(VI)) = $3.1(3) \times 10^{-14}$ m^2 s^{-1} Joseph et al., 2013) or Np(V) (D_a(Np(V)) = $2.8(5) \times 10^{-14}$ m^2 s^{-1}, calculated from Wu et al., 2009). This suggests that under the settings of the experiment conducted, Pu diffuses slower in OPA than other minor actinides.

4. Conclusions

TOF-SIMS and rL-SNMS were successfully applied to study the diffusion of 4×10^{-6} mol L^{-1} Pu(V) in Opalinus Clay with clay pore water as mobile phase under ambient air conditions. For the in-diffusion experiments a novel, easily scalable setup with small clay cylinders ($\varnothing$ = 5 mm, L ≈15 mm) was developed using modern 3D printing techniques. The in-diffusion experiments lasted up to 35 d. At the end of the diffusion experiment, the electrophoretic mobility of Pu in the sample reservoir was determined by CE-ICP-MS and compared to Np(V). This measurement showed that PuO_2^+ is the main species in the aqueous phase of the diffusion reservoir at pH 7.6 under ambient air conditions.

By cleaving the clay cylinders parallel to the natural bedding of the clay, several 500 µm × 500 µm areas (FOVs) of the pristine clay surface were investigated at the micrometer scale using TOF-SIMS and rL-SNMS. By measuring multiple FOVs along the interface of the OPA core and the reservoir, it was possible to retrieve an averaged diffusion profile of Pu comparable with the classic abrasive peeling technique used for strongly sorbing radionuclides (Van Loon and Müller, 2014). The determined apparent diffusion coefficient $D_a = 3.2(4) \times 10^{-15}$ m^2 s^{-1} of Pu is smaller compared to values found in literature for the diffusion of U(VI) and Np(V) in OPA, suggesting that Pu is less mobile. However, due to limitations of the diffusion model, this is subject of further investigations, which should also consider the complex redox chemistry of Pu in the system.

Certain patterns of the reactive transport of Pu inside OPA could be observed by the elemental distributions of Pu and several matrix elements, i.e., Fe and Ca, at the micrometer scale. Scatter plots of the Pu, Fe and Ca signal intensities reveal correlations between areas of increased Pu signal and Fe and Ca. Although the associated mineral phase could not be identified by TOF-SIMS, a comparison with literature (Kaplan et al., 2024, 2017; Breckheimer et al., 2023) points towards the Fe(II) bearing mineral pyrite with a cementing phase of calcite as the cause for Pu 'hot spots'. The presence of Pu could be confirmed by rL-SNMS, despite its signal for Pu in OPA was significantly reduced compared to the TOF-SIMS signal for Pu^+ and PuO^+. Possible reasons for this include an insufficient sputter rate of atomic Pu necessary for resonant photoionization in the chemical matrix of OPA or insufficient laser power for saturating the ionizing step. The latter is currently being addressed with the setup of a new laser system that allows for higher laser powers and the application of novel excitation schemes for actinides (Savina et al., 2018; Kneip et al., 2020; Kaja et al., 2024). In future investigations of diffusion samples with several actinides present solution, rL-SNMS will be used to resolve isobaric interferences, e.g., between $^{238}UH^+$ and $^{239}Pu^+$.

In conclusion, the combined approach of TOF-SIMS and rL-SNMS allows for faster access to diffusion profiles of strongly sorbing radionuclides compared to the classic abrasive peeling technique while retaining detailed chemical information at the micrometer scale. In the context of the safety assessment for the long-term storage of nuclear waste, both methods are powerful tools for the analysis of transport processes in porous media like argillaceous rocks or concrete. This will facilitate future diffusion experiments with other radionuclides, longer diffusion times and other chemical conditions, e.g. in the presence of organic substances like cement additives or waste constituents (Tasi et al., 2021).

CRediT authorship contribution statement

Felix Berg: Writing – review & editing, Writing – original draft, Visualization, Project administration, Methodology, Investigation, Formal analysis, Conceptualization. **Christopher Sirleaf:** Writing – review & editing, Investigation. **Janik Lohmann:** Writing – review & editing, Investigation. **Markus Breckheimer:** Writing – review & editing, Methodology, Investigation, Conceptualization. **Tobias Reich:** Writing – review & editing, Supervision, Resources, Project administration, Methodology, Funding acquisition, Conceptualization.

Funding

This project was funded by the Federal Ministry of Education and Research (BMBF) under contract no. 02NUK075B (project SOLARIS). M. B. acknowledges funding from the European Union's Horizon 2020 project EURAD (WP FUTuRE), EC Grant agreement no. 847593.

Declaration of competing interest

The authors declare that they have no known competing financial interests or personal relationships that could have appeared to influence the work reported in this paper.

Acknowledgments

The authors would like to thank Dr. Samer Amayri for his contributions during fruitful discussions, Dr. Daniel Grolimund for providing the Opalinus Clay rock and the mechanical workshops of the Department of Chemistry and the research reactor TRIGA at the Johannes Gutenberg-Universität Mainz for the CNC milling of the samples and production of PMMA sample holders. Furthermore, we would like to thank R. Dagnelie and the second anonymous reviewer for their efforts and helpful comments.

Appendix A. Supplementary data

Supplementary material related to this article can be found online at https://doi.org/10.1016/j.apgeochem.2025.106332.

Data availability

Data will be made available on request.

References

Andra, 2022. Demande d'autorisation de création (DAC). URL https://www.andra.fr/cigeo/les-documents-de-reference#section-14367. (Accessed on Feb. 10th 2025).

Benninghoven, A., Hagenhoff, B., Niehuis, E., 1993. Surface MS: probing real-world samples. Anal. Chem. 65 (14), 630A–640A.

Bosco, H., Hamann, L., Kneip, N., Raiwa, M., Weiss, M., Wendt, K., Walther, C., 2021. New horizons in microparticle forensics: Actinide imaging and detection of ^{238}Pu and ^{242m}Am in hot particles. Sci. Adv. 7 (44), eabj1175.

Breckheimer, M., Amayri, S., Ferreira Sanchez, D., Grolimund, D., Reich, T., 2023. Chemical tomography of pyrite composites extracted from Opalinus Clay and reacted with neptunium and plutonium. In: Book of abstracts, 18th International Conference on Chemistry and Migration Behaviour of Actinides and Fission Products in the Geosphere - Migration. p. 340.

Bundesgesetzblatt, 2017. Repository Site Selection Act (Standortauswahlgesetz - StandAG). Bundesgesetzblatt (26), 1074–1102, URL http://www.bgbl.de/xaver/bgbl/start.xav?startbk=Bundesanzeiger_BGBl&jumpTo=bgbl117s1074.pdf.

Churakov, S.V., Hummel, W., Fernandes, M.M., 2020. Fundamental research on radiochemistry of geological nuclear waste disposal. Chimia 74 (12), 1000.

Clark, D.L., Hecker, S.S., Jarvinen, G.D., Neu, M.P., 2008. Plutonium, In: Morss, L.R., Edelstein, N.M., Fuger, J. (Eds.), third ed. In: The Chemistry of the Actinide and Transactinde Elements, vol. 2, Springer, pp. 813–1264 (Chapter 7).

De Laeter, J.R., Böhlke, J.K., De Bievre, P., Hidaka, H., Peiser, H., Rosman, K., Taylor, P., 2003. Atomic weights of the elements. Review 2000 (IUPAC Technical Report). Pure Appl. Chem. 75 (6), 683–800.

Fröhlich, D., Amayri, S., Drebert, J., Grolimund, D., Huth, J., Kaplan, U., Krause, J., Reich, T., 2012. Speciation of Np(V) uptake by Opalinus Clay using synchrotron microbeam techniques. Anal. Bioanal. Chem. 404, 2151–2162.

Fröhlich, D., Amayri, S., Drebert, J., Reich, T., 2013. Influence of humic acid on neptunium(V) sorption and diffusion in Opalinus Clay. Radiochim. Acta 101 (9), 553–560.

Geckeis, H., Zavarin, M., Salbu, B., Lind, O.C., Skipperud, L., 2019. Environmental chemistry of plutonium, second ed. In: Plutonium Handbook, vol. 4, American Nuclear Society, p. 1979,

Giffaut, E., Grivé, M., Blanc, P., Vieillard, P., Colàs, E., Gailhanou, H., Gaboreau, S., Marty, N., Made, B.t., Duro, L., 2014. Andra thermodynamic database for performance assessment: ThermoChimie. Appl. Geochem. 49, 225–236.

Greer, R.T., 1978. Evaluation of pyrite particle size, shape, and distribution factors. Energy Sources 4 (1), 23–51.

Grüning, C., Huber, G., Klopp, P., Kratz, J., Kunz, P., Passler, G., Trautmann, N., Waldek, A., Wendt, K., 2004. Resonance ionization mass spectrometry for ultratrace analysis of plutonium with a new solid state laser system. Int. J. Mass Spectrom. 235 (2), 171–178.

Joseph, C., Van Loon, L., Jakob, A., Steudtner, R., Schmeide, K., Sachs, S., Bernhard, G., 2013. Diffusion of U(VI) in Opalinus Clay: Influence of temperature and humic acid. Geochim. Cosmochim. Acta 109, 74–89.

Kaja, M., Studer, D., Berg, F., Berndt, S., Düllmann, C.E., Kneip, N., Reich, T., Urquiza-González, M., Wendt, K., 2024. Resonant laser ionization of neptunium: investigation on excitation schemes and the first ionization potential. Eur. Phys. J. D 78 (5), 1–9.

Kaplan, U., Amayri, S., Drebert, J., Grolimund, D., Reich, T., 2024. Plutonium mobility and reactivity in a heterogeneous clay rock barrier accented by synchrotron-based microscopic chemical imaging. Sci. Rep. 14 (1), 1–11.

Kaplan, U., Amayri, S., Drebert, J., Rossberg, A., Grolimund, D., Reich, T., 2017. Geochemical interactions of plutonium with Opalinus Clay studied by spatially resolved synchrotron radiation techniques. Environ. Sci. Technol. 51 (14), 7892–7902.

Kneip, N., Düllmann, C.E., Gadelshin, V., Heinke, R., Mokry, C., Raeder, S., Runke, J., Studer, D., Trautmann, N., Weber, F., Wendt, K., 2020. Highly selective two-step laser ionization schemes for the analysis of actinide mixtures. Hyperfine Interactions 241 (1), 1–7.

Lerouge, C., Grangeon, S., Claret, F., Gaucher, E., Blanc, P., Guerrot, C., Flehoc, C., Wille, G., Mazurek, M., 2014. Mineralogical and isotopic record of diagenesis from the Opalinus Clay formation at Benken, Switzerland: implications for the modeling of pore-water chemistry in a clay formation. Clays Clay Miner. 62 (4), 286–312.

Maes, N., Churakov, S., Glaus, M., Baeyens, B., Dähn, R., Grangeon, S., Charlet, L., Brandt, F., Poonoosamy, J., Hoving, A., et al., 2024. EURAD state-of-the-art report on the understanding of radionuclide retention and transport in clay and crystalline rocks. Front. Nucl. Eng. 3, 1417827.

Montavon, G., Ribet, S., Loni, Y.H., Maia, F., Bailly, C., David, K., Lerouge, C., Madé, B., Robinet, J., Grambow, B., 2022. Uranium retention in a Callovo-Oxfordian clay rock formation: From laboratory-based models to in natura conditions. Chemosphere 299, 134307.

Nagra, 2022. The Site for the Deep Geological Repository - Nagra's Proposal. Tech. Rep., URL https://nagra.ch/wp-content/uploads/2022/09/Report-the-site-for-the-deep-geological-repository-Nagras-proposal.pdf.

Neck, V., Altmaier, M., Seibert, A., Yun, J.-I., Marquardt, C.M., Fanghänel, T., 2007. Solubility and redox reactions of Pu(IV) hydrous oxide: Evidence for the formation of PuO_{2+x}(s, hyd). Radiochim. Acta 95 (4), 193–207.

Newville, M., Otten, R., Nelson, A., Stensitzki, T., Ingargiola, A., Allan, D., Fox, A., Carter, F., Michał, Osborn, R., Pustakhod, D., Weigand, S., Ineuhaus, Aristov, A., Glenn, Mark, mgunyho, Deil, C., Hansen, A.L.R., Pasquevich, G., Foks, L., Zobrist, N., Frost, O., Stuermer, Jaskula, J.-C., Caldwell, S., Eendebak, P., Pompili, M., Nielsen, J.H., Persaud, A., 2024. lmfit/lmfit-py: 1.3.2. Zenodo.

Pearson, F., 1998. Opalinus Clay Experimental Water: A1 Type, Version 980318. Tech. Rep. TM-44-98-07, Paul Scherrer Institut, Villigen PSI.

Pearson, F., Arcos, D., Bath, A., Boisson, J., Fernández, A., Gäbler, H., Gaucher, E., Gautschi, A., Griffault, L., Hernán, P., et al., 2003. Mont Terri project-Geochemistry of water in the Opalinus clay formation at the Mont Terri Rock Laboratory. Berichte des BWG, Ser. Geol. 5.

Preter, P.D. (Ed.), 2023. Activity Report 2021 & 2022. EIG EURIDICE, Tech. Rep. EURIDICE/54165858. URL https://www.euridice.be/sites/default/files/editor/Euridice%20Activity%20Report%202021_2022.pdf.

Raiwa, M., Büchner, S., Kneip, N., Weiß, M., Hanemann, P., Fraatz, P., Heller, M., Bosco, H., Weber, F., Wendt, K., Walther, C., 2022. Actinide imaging in environmental hot particles from Chernobyl by rapid spatially resolved resonant laser secondary neutral mass spectrometry. Spectrochim. Acta Part B: At. Spectrosc. 190, 106377.

Reich, T., Amayri, S., Boerner, P.J.B., Drebert, J., Fröhlich, D.R., Grolimund, D., Kaplan, U., 2016. Speciation of neptunium during sorption and diffusion in natural clay. J. Physics: Conf. Ser. 712 (1), 012081.

Savina, M.R., Trappitsch, R., Kucher, A., Isselhardt, B.H., 2018. New resonance ionization mass spectrometry scheme for improved uranium analysis. Anal. Chem. 90 (17), 10551–10558.

Schönenbach, D., Berg, F., Breckheimer, M., Hagenlocher, D., Schönberg, P., Haas, R., Amayri, S., Reich, T., 2021. Development, characterization, and first application of a resonant laser secondary neutral mass spectrometry setup for the research of plutonium in the context of long-term nuclear waste storage. Anal. Bioanal. Chem. 413 (15), 3987–3997.

Tasi, A., Gaona, X., Rabung, T., Fellhauer, D., Rothe, J., Dardenne, K., Lützenkirchen, J., Grive, M., Colas, E., Bruno, J., 2021. Plutonium retention in the isosaccharinate–cement system. Appl. Geochem. 126, 104862.

van Eerten, D., Raiwa, M., Hanemann, P., Leifermann, L., Weissenborn, T., Schulz, W., Weiß, M., Shulaker, D.Z., Boone, P., Willingham, D., Thomas, K., Sammis, B., Isselhardt, B., Savina, M., Walther, C., 2023. Multi-element isotopic analysis of hot particles from Chornobyl. J. Hazard. Mater. 452, 131338.

Van Loon, L.R., Müller, W., 2014. A modified version of the combined in-diffusion/abrasive peeling technique for measuring diffusion of strongly sorbing radionuclides in argillaceous rocks: A test study on the diffusion of caesium in Opalinus Clay. Appl. Radiat. Isot. 90, 197–202.

Virtanen, P., Gommers, R., Oliphant, T.E., Haberland, M., Reddy, T., Cournapeau, D., Burovski, E., Peterson, P., Weckesser, W., Bright, J., van der Walt, S.J., Brett, M., Wilson, J., Millman, K.J., Mayorov, N., Nelson, A.R.J., Jones, E., Kern, R., Larson, E., Carey, C.J., Polat, I., Feng, Y., Moore, E.W., VanderPlas, J., Laxalde, D., Perktold, J., Cimrman, R., Henriksen, I., Quintero, E.A., Harris, C.R., Archibald, A.M., Ribeiro, A.H., Pedregosa, F., van Mulbregt, P., SciPy 1.0 Contributors, 2020. SciPy 1.0: fundamental algorithms for scientific computing in Python. Nature Methods 17 (3), 261–272.

Wang, P., Huang, Y., Wang, C., Feng, Z., Huang, Q., 2013. Pyrite morphology in the first member of the Late Cretaceous Qingshankou formation, Songliao Basin, northeast China. Palaeogeogr. Palaeoclimatol. Palaeoecol. 385, 125–136.

Willberger, C., Amayri, S., Häußler, V., Scholze, R., Reich, T., 2019. Investigation of the electrophoretic mobility of the actinides Th, U, Np, Pu, and Am in different oxidation states. Anal. Chem. 91 (18), 11537–11543.

Wu, T., Amayri, S., Drebert, J., van Loon, L.R., Reich, T., 2009. Neptunium(V) sorption and diffusion in Opalinus Clay. Environ. Sci. Technol. 43 (17), 6567–6571.

Yaroshchuk, A.E., Van Loon, L.R., 2008. Improved interpretation of in-diffusion measurements with confined swelling clays. J. Contam. Hydrol. 97 (1–2), 67–74.

Publication III: Investigating a novel excitation scheme for RIMS measurements of Pu

Contribution statement

The author was the main investigator for this publication. The sample preparation, characterization as well as all RIMS measurements were performed by the author. He also conducted the data analysis, created the visualizations, wrote the original draft and was responsible for the review process. The publication contains the following author contribution statement:
F. Berg: Writing - Original Draft, Writing - Review & Editing, Visualization, Methodology, Conceptualization, Investigation, Formal analysis, Project administration **T. Reich:** Writing - Review & Editing, Conceptualization, Methodology, Resources, Supervision, Project administration, Funding acquisition.

Copyright

Analytical and Bioanalytical Chemistry
https://doi.org/10.1007/s00216-025-06062-0

RESEARCH PAPER

Investigating a novel three-step excitation scheme for the ultra-trace analysis of plutonium via RIMS

Felix Berg[1] · **Tobias Reich**[1]

Received: 27 June 2025 / Revised: 24 July 2025 / Accepted: 28 July 2025

Abstract
A novel three-step excitation scheme for the ultra-trace analysis of ^{242}Pu via resonance ionization mass spectrometry reported by Galindo-Uribarri et al. was investigated. Previously unknown optical isotope shifts for the second excitation and ionizing step for the plutonium isotopes $^{238-240,244}$Pu were measured. Saturation powers were recorded, and the efficiency was compared via electrodepositions of ^{238}Pu with reference to the established scheme by Grüning et al. routinely applied on our setup. Both schemes share the same first excitation step and use a Rydberg state as ionizing step. The resonances for ^{242}Pu published by Galindo-Uribarri et al. were confirmed.

Keywords Ultra-trace analysis · Resonance ionization mass spectrometry · Plutonium · Optical isotope shifts

Introduction

Plutonium (Pu) is a major by-product of nuclear power plants and has been released into the environment during incidents as well as production and tests of nuclear weapons in the twentieth century [1–3]. Due to its long-lived isotopes and its high radiotoxicity as well as complex aqueous chemistry, Pu is considered a major health risk and therefore is also of interest for the safety case of a deep geological long-term nuclear waste storage facility [4, 5]. In order to monitor Pu in the environment, to study its geochemical interactions in the scenario of a deep geological repository, as well as monitor such a facility in the future, a method is required that can detect and quantify Pu even at the trace and ultra-trace level. Traditional radioanalytical tools such as α spectroscopy or liquid scintillation counting (LSC) depend on the specific radioactivity of an isotope and are not able to detect small amounts of long-lived isotopes. Various types of mass spectrometry, such as inductively coupled plasma-mass spectrometry (ICP-MS) [6–8] or thermal ionization mass spectrometry (TIMS) [9, 10], do not depend on the radioactive properties of the analytes and allow for the detection and quantification at very low levels down to 10^5 to 10^8 atoms, but can be hampered by isobaric interference. This is also the case for accelerator mass spectrometry (AMS), which can reach levels of detections down to a few thousand atoms [11–13], but only after extensive sample preparation and development of the suppression of isobaric interferences.

By photoionizing atoms via laser light, using a multi-step excitation scheme exploiting the unique electronic level structure of every element, resonance ionization mass spectrometry (RIMS) is able to effectively suppress isobaric interferences and allows for the detection and quantification of even the smallest amounts of analyte [14–17]. The separation of isotopes by their mass-to-charge ratio in the mass separator can be even further enhanced by exploiting the optical isotope shift. Due to the varying number of neutrons in the nucleus, slight differences in the electronic energy levels of different isotopes of the same element exist, and by tuning sufficiently narrow laser light exactly to these energies, isotope selectivity can be achieved. To note, the exact knowledge of the optical isotope shift is of the utmost importance if isotope ratios are to be quantified. For example, if the ratio of ^{240}Pu/^{239}Pu is an indication for the burn-up of nuclear fuel or an indication of the type of nuclear reactor, it needs to be guaranteed that both isotopes are equally photoionized. In case the optical isotope shift is sufficiently large, retuning the lasers to the exact resonance of each isotope might be necessary.

Felix Berg
feberg@uni-mainz.de

Tobias Reich
treich@uni-mainz.de

[1] Department of Chemistry - Nuclear Chemistry, Johannes Gutenberg-Universität Mainz, 55099 Mainz, Germany

Published online: 23 August 2025

Efficiency is an important characteristic of a multi-step photoionization scheme. Not all optical transitions yield the same amount of excited electrons, and careful characterization as well as selection of each excitation step are required. Nevertheless, the overall efficiency of a RIMS measurement does not only depend on the excitation scheme but also among other things on the type of source region, its atomization efficiency, the laser interaction volume, and the transmission efficiency of the mass separator.

Recently, Galindo-Uribarri et al. reported a novel, highly efficient three-step, three-color scheme for the laser resonance ionization of ^{242}Pu [18]. The Pu atoms are first excited from $5f^6 7s^2\ ^7F_0$ ground state to the known excited state $5f^6 7s6p\ ^7D_1$ at 23,765.98(2) cm^{-1} using laser light from a titanium:sapphire (Ti:Sa) laser at λ_1 = 420.77 nm (scheme **a** in Fig. 1). From this first excited state (FES), the Pu atoms were further excited to a second excited state (SES) of even parity at 35,977.28(4) cm^{-1} using a second Ti:Sa laser with λ_2 = 818.91 nm. Using laser light with λ_3 = 792.79 nm, the Pu atoms were further excited to a state at 48,590.90(5) cm^{-1}. This state is below the ionization potential (IP) of Pu, and from there, ionization can occur via different mechanisms, such as infrared radiation, an external electrical field, or gas collision. With their experimental setup, Galindo-Uribarri et al. observed a factor of 4.5 higher signal compared to scheme **c** (Fig. 1) reported by Raeder et al. [19]. As shown in Fig. 1, **a** and **c** use the same FES of ^{242}Pu. In scheme **c**, the intermediate SES at 35,568.70(4) cm^{-1} with J = 2 is excited using λ_2 = 847.28 nm. The ionization of Pu takes place with λ_3 = 750.24 nm via the population of an auto-ionizing state above the IP at 48,898 cm^{-1}. In routine ultra-trace analysis of Pu isotopes in environmental samples using RIMS at the Nuclear Chemistry group in Mainz, the excitation scheme developed by Grüning et al. (scheme **b** in Fig. 1) is applied [20]. It uses the same FES and SES as the scheme by Raeder et al. But instead of exciting an auto-ionizing state, ionization takes place from a populated Rydberg state at 48,597.51(6) cm^{-1} below the IP. Since a higher efficiency would improve the RIMS analysis of Pu, we compared the schemes **a** and **b** using the RIMS setup at the Nuclear Chemistry group in Mainz. Scheme **c** by Raeder et al. was not investigated further as part of this study. As a first step, the unknown isotope shifts for $^{238-240,244}$Pu as well as the saturation power P_s for each excitation step for the scheme by Galindo-Uribarri et al. were determined. Afterwards, the ionization efficiency of the two schemes was determined using the short-lived isotope ^{238}Pu ($t_{1/2}$ = 87.74 a). This allowed for the precise quantification of the exact amount of ^{238}Pu in each sample ($\approx 10^{10}$ atoms) via α spectroscopy before the RIMS measurement.

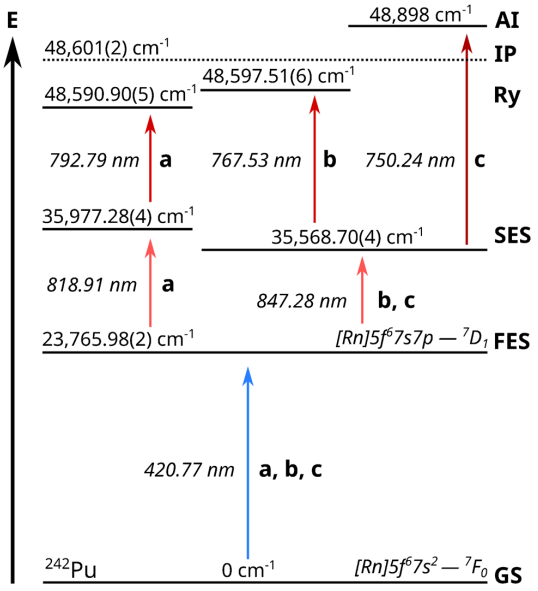

Fig. 1 Comparison of three excitation schemes used for the resonant photoionization of ^{242}Pu. Scheme **a** was reported by Galindo-Uribarri et al. [18], and **b** was developed by Grüning et al. [20] and is regularly applied in our laboratory. Both schemes use a Rydberg state (Ry) as ionizing state. Scheme **c** by Raeder et al. [19] was used in the study by Galindo-Uribarri et al. to compare the efficiency of their newly developed scheme, and an increase of efficiency by a factor of 4.5 was reported. It differs from **b** only in the ionizing step. All schemes use the same first excited state (FES). The ionization potential (IP) was reported in [21]. Errors, if available, are from the respective publications. Schematic not to scale

Materials and methods

Setup for resonance ionization mass spectrometry

The RIMS setup consisted of a custom time-of-flight mass spectrometer (TOF-MS) displayed in Fig. 2 and three custom Ti:Sa lasers jointly pumped by a frequency doubled Nd:YAG laser (Photonics Industries International, Inc., Ronkonkoma, NY, USA, model DM532-60) at 532 nm with approximately 45 W laser power and 10 kHz repetition rate. For the measurement of the isotope shifts, the initial saturation curves, and the efficiency measurements, the three Ti:Sa of the original design presented in the work by Grüning et al. [20] were used. These lasers use a Lyot filter and an etalon for wavelength selection and have an approximate linewidth of 6–8 GHz and a Pockels cell for temporal synchronization. To note, the 10 kHz repetition rate is an increase compared to the 6.6 kHz in the work of Grüning et al., which was conducted on the same setup. Furthermore, the lasers are not introduced into the source region via an optical fiber, but directly, which allows for higher laser powers in the source region. After the initial results had indicated insufficient laser power in

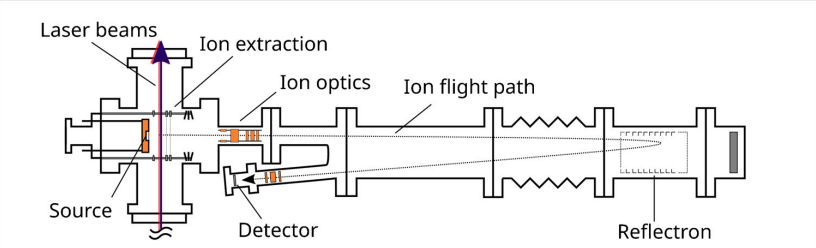

Fig. 2 Schematic view of the time-of-flight mass separator (TOF-MS) of the Nuclear Chemistry group in Mainz. The laser beams are directly introduced into the source region perpendicular to the flight path of the photoions. Pressure for measurements is $< 2 \times 10^{-6}$ mbar. Not to scale

the IS, the Ti:Sa driving the SES-Ry transition was replaced with a current generation model that allows for higher output powers to repeat the saturation curve measurements. The current generation "standard" Ti:Sa, that are developed by the LARISSA workgroup at the Institute of Physics at the Johannes Gutenberg-Universität Mainz, have a more compact design without the need for a Pockels cell and have a linewidth of approximately 5 GHz, but still use a Lyot filter and an etalon for wavelength selection [22]. Laser system and mass spectrometer were synchronized via a joint pulse generator (BNC, San Rafael, USA, model 577). The wavelengths of the Ti:Sa lasers were measured quasi simultaneously by a wavemeter equipped with a switch (Highfinesse, Tübingen, Germany, WS6-200, 200 MHz accuracy). Laser powers were recorded before and after each efficiency measurement to exclude power fluctuations (PowerMax© model PM3 with Fieldmate powermeter, Coherent GmbH, Göttingen, Germany). The laser beams were introduced into the atom source perpendicular to the flight path of the ions. To ensure optimal overlap between the beams, they were guided through two irides before and after the source region. Samples were placed into the source as electrodepositions on tantalum filaments covered with a thin layer of titanium (Ti) as reducing agent. These sandwich filaments were then resistively heated by applying current directly to them, resulting in a cloud of atomic plutonium in which the laser light is shone. Measurements were conducted at pressures $< 2 \times 10^{-6}$ mbar. Ions were extracted into the TOF-MS by applying an extraction pulse with ca. 1.3 kV. The mass spectrometer and laser setup have been described in more detail in previous publications [16, 20, 23].

Electrodepositions of Pu

All samples used in this study were produced via electrodeposition of plutonium onto tantalum filaments via a custom electrolysis cell described in detail in previous publications [16, 24]. For spectroscopy samples, a mixture containing $\approx 10^{10}$ atoms of ^{238}Pu, ^{239}Pu, ^{240}Pu, ^{242}Pu, and ^{244}Pu each was added to 6 mL 0.2 g mL^{-1} $(NH_4)_2SO_4$ (Alfa Aesar GmbH & Co KG, Karlsruhe, Germany) electrolyte solution in MilliQ water (18.2 MΩ, Synergy^{TM} Millipore water system, Millipore GmbH, Schwalbach, Germany) at pH 1.8. Approximately 350 mA at 16 V were applied for 1.5 h. Five minutes before the end of the electrolysis, 5–6 drops of conc. NH_4OH (Merck KGaA, Darmstadt, Germany) were added to the solution to prevent detaching of the deposited Pu. The recording of the laser power saturation curves was conducted using a sample of ^{239}Pu. For efficiency measurements, the samples were prepared by adding only an aliquot with $\approx 10^{10}$ atoms of ^{238}Pu to the electrolyte solution. All samples were covered with an ≈ 1 µm thick titanium layer as reducing agent applied in a custom sputter setup, increasing the amount of atomic Pu evaporated in the source region of the mass spectrometer.

Results and discussion

Isotope shifts

To scan the resonances for the transitions of each Pu isotope, two of three lasers were kept at a constant wavenumber while the third one was varied. Each resonance was scanned six times: three times from lower to higher wavenumbers and three times vice versa. The power of each step was reduced if necessary so little to no saturation broadening was observed. To retrieve the centroids of the resonances for the first and second excitation steps, the data was fitted with a single Gaussian curve plus a linear component for even isotopes and two Gaussian curves and a linear component for ^{239}Pu to account for the hyperfine structure. ^{239}Pu is the only Pu isotope in this study with a nuclear spin of $I = 1/2$. All the other isotopes have a nuclear spin $I = 0$. The centroid of the ^{239}Pu resonances was calculated by the sum of the centroids of the two Gaussian curves, weighted by the respective total area fraction. The ionization steps were modeled with a single Lorentzian curve and a linear component.

Table 1 shows the resonances observed for each excitation step. The results for ^{242}Pu as well as for the first excitation step of the other Pu isotopes are in excellent agreement

Table 1 In this work observed resonances for $^{238-240,242,244}$Pu for the three-step excitation scheme proposed by Galindo-Uribarri et al. The resonances found for the first excitation step (FES) for all isotopes as well as for the known second excitation step (SES) and ionizing step (IS) for ^{242}Pu are in excellent agreement with the literature [18, 20]

Pu isotope	FES/cm^{-1}	SES/cm^{-1}	IS/cm^{-1}
238	23,766.41(1)	12,210.84(1)	12,613.82(1)
239	23,766.32(2)	12,210.95(2)	12,613.76(1)
240	23,766.16(1)	12,211.10(1)	12,613.69(1)
242	23,765.97(1)	12,211.29(1)	12,613.59(1)
244	23,765.77(1)	12,211.48(1)	12,613.50(1)
242 (Lit.)	23,765.98(2) [20]	12,211.30(4) [18]	12,613.62(2) [18]

with the literature [18, 20]. Furthermore, in some cases, we were able to improve the uncertainty. These resonances were then used in the subsequent saturation power and efficiency measurements. The optical isotope shifts of the different Pu isotopes in reference to ^{242}Pu are displayed in Fig. 3 and Table 2. Also included are the isotope shifts for the FES calculated from the resonances described in literature [20], which are in excellent agreement with the results from the measurements presented here as well.

As both schemes compared in this work share the same first excitation step and as it was already known from literature [20], it is clear that it needs to be adjusted for each isotope to ensure maximum photoionization. For the newly measured isotope shifts of the second excitation step for the scheme proposed by Galindo-Uribarri et al., the difference between the resonance for ^{238}Pu and ^{244}Pu for the second excitation step is up to ≈20 GHz and for the ionizing step ≈10 GHz. That means even using Ti:Sa lasers with a linewidth of 6–8 GHz, it is not possible to photoionize all isotopes equally at

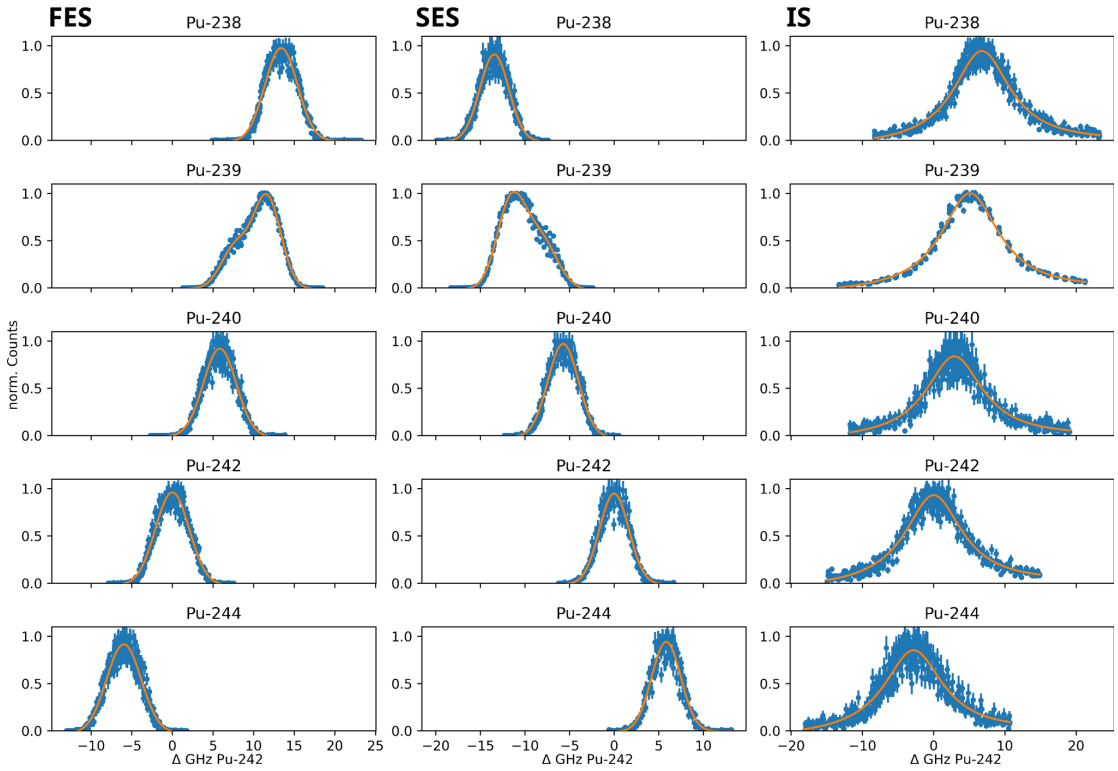

Fig. 3 Isotope shifts of $^{238-240,244}$Pu in reference to ^{242}Pu. Each resonance was scanned six times. The first and second excitation steps (FES, SES) for even isotopes were modeled using a Gaussian curve as well as a linear component for background, and for the uneven isotope ^{239}Pu, two Gaussian curves and a linear term were used to account for the hyperfine structure. The ionizing step (IS) was modeled with a Lorentzian curve and a linear component. Error bars are presented as $\sigma = \sqrt{N}$ from the number of detected ions N

Table 2 Isotope shifts for the first and second excitation (FES, SES) as well as ionizing step (IS) of $^{238-240,244}$Pu in reference to ^{242}Pu observed in this work. Literature values for the FES were calculated from wavenumbers given in [20]

Pu isotope	FES Lit. [20]/GHz	FES/GHz	SES/GHz	IS/GHz
238	12.6(12)	13.4(5)	−13.4(5)	6.8(5)
239	10.2(12)	10.4(6)	−10.2(7)	5.1(5)
240	5.4(12)	5.8(5)	−5.7(5)	2.9(6)
244	−6.9(12)	−6.0(5)	5.8(5)	−2.8(6)

the same time. By comparing the resonance positions shown in Fig. 3, it is evident that already for isotopes with overlapping resonances for the FES and SES and a relatively similar ionizing step, such as ^{238}Pu and ^{239}Pu, the excitation wavelengths need to be adjusted. Lasers tuned to the FES and SES of ^{238}Pu would not cover the whole resonances of ^{239}Pu, and therefore, the amount of ^{239}Pu would be underestimated. In the same scenario, all the other isotopes are not excited and would be lost in the analysis. Therefore, in a measurement of the isotopic ratio using the scheme by Galindo-Uribarri et al., the optical isotope shift cannot be omitted and all three lasers need to be adjusted to the respective isotope to ensure correct results. In case of the scheme by Grüning et al., the second excitation step needs also to be retuned for each isotope as well, but the ionizing step does not display a significant optical isotope shift and it is not necessary to adjust the laser for each isotope, therefore simplifying the measurement.

Saturation

The saturation curves for the FES, SES, and IS of the excitation schemes by Galindo-Uribarri et al. and Grüning et al. displayed in Fig. 4 were recorded by varying the laser power (P) of the excitation step in question via a neutral density filter while keeping the other two constant. Since the measurement of the IS required more datapoints in order to avoid influences caused by changes of the emittance from the sample over time, the measurement procedure was slightly adopted: Here, after every two data points, a reference measurement without attenuation of the laser beam was included to normalize the data. As mentioned in the setup section, after initial results indicated insufficient laser power for the IS, the measurements presented here were repeated with a new generation Ti:Sa laser driving the SES-Ry transition that was able to provide more power for the IS compared to the efficiency measurements. The FES and SES were still driven by the older generation Ti:Sa. The laser powers were measured (FES: PowerMax© model PM3 with Fieldmate powermeter, Coherent GmbH, Göttingen, Germany; SES, IS: PM-160T-HP, Thorlabs GmbH, Bergkirchen, Germany) directly in front of the entrance window of the source region. The intensity I was then modeled using Eq. 1 where I_0 is the non-resonant contribution by the other excitation steps, A the maximum theoretically saturation amplitude, P_s

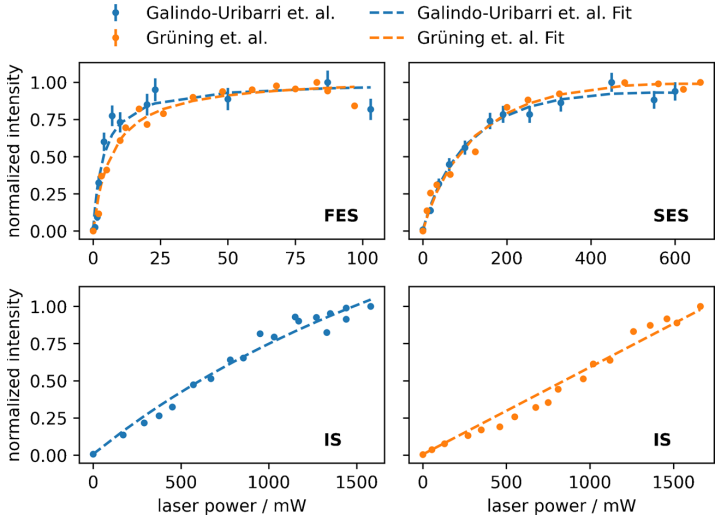

Fig. 4 Measured saturation curves for the first excitation step (FES), the second excitation step (SES), and the ionizing step (IS) for the excitation schemes by Galindo-Uribarri et al. (blue) and Grüning et al. (orange) as well as the respective fit (dashed line). No saturation was reached for either scheme in the IS. Errors are calculated from the number of ions detected N via $\sigma = \sqrt{N}$. For the measurements of the Grüning et al. scheme, the error bars are small compared to the data point symbol

the saturation power, and the term $m \cdot P$ accounts for non-resonant ionization as well as the volume increase of the laser beam with the increase in power [19].

$$I = I_0 + A \cdot \frac{P/P_s}{1 + (P/P_s)} + m \cdot P. \quad (1)$$

Table 3 displays the resulting saturation powers P_s.

For both schemes, the FES and SES reach saturation. Both schemes are using the same FES and only minimal laser power is required to saturate the transition. For the two different SES, more laser power is required, but also here a plateau is reached. In contrast, both schemes do not reach saturation in the IS. Here, an increase in laser power leads to a continuous increase in signal intensity and the fit, although converging, does not yield credible results. The foci of the laser beams had previously been adjusted for maximum signal intensity. To further investigate the unsaturated IS, the beam profile of the IS laser was measured to ensure a sufficient focus. Since measuring the beam profile directly inside the source region is not possible, the beam was diverted using a mirror and the beam profile camera (CinCam CMOS-1202-OM, CINOGY Technologies GmbH, Duderstadt, Germany) was placed at the same distance compared to the ionization volume. Analysis of the beam profile with a Gaussian fit using the software provided with the camera (RayCi-lite, CINOGY Technologies GmbH, Duderstadt, Germany) showed a circular distribution over an area of ca. 0.16 mm^2, resulting in an energy density of approximately 1 mJ mm^{-2} at 1.6 W and 10 kHz operation. That despite this high energy density no saturation was reached indicates that the laser interaction volume is too small. With the SES-Ry driving laser beam focused so strongly, it can no longer be assumed that the whole atom plume emitted from the sandwich type filament in the source region is sufficiently illuminated by this laser beam. If the beam diameter is only slightly increasing with the increasing power during the saturation curve measurement, a larger area of the atom plume is covered and more atoms are photoionized. Due to the perpendicular geometry of the laser interaction volume used in this work, the effect of a lack of energy density might be more pronounced compared to a co-linear setup, since there is less probability for an atom to interact with the photons. By applying such a co-linear laser beam geometry to illuminate a hot-cavity atom source, Galindo-Uribarri et al. determined a saturation power of 325(67) mW for the IS [18].

Table 3 Resulting saturation powers P_s for the different excitation steps

Scheme	FES/mW	SES/mW	IS/mW
Galindo-Uribarri et al.	4(2)	135(36)	–
Grüning et al.	7(2)	153(58)	–

In addition to being more efficient for atomization, such a source provides a confined atom plume and therefore additionally increased atom-photon interaction probability. What also needs to be considered when comparing the saturation behaviors between the two setups is the actual ionization process from the Rydberg state. While in the source region used in this work most likely the only contributing ionization path is the electric field caused by the extraction electrode, in the hot-cavity-type source, other pathways, such as black-body radiation and collision, play a more dominant role [25].

Efficiency measurements

For efficiency measurements, the samples were characterized via α spectroscopy (detector: Ortec, Germany, model CR-SNA-450-100) to yield the exact amount of ^{238}Pu deposited. Figure 5 displays an exemplary spectrum recorded for one of the samples used in this study. Each sample was measured 3600 s. The detector was energy calibrated using ^{148}Gd and ^{241}Am. The detector efficiency of 0.146(15) was determined using a certified ^{241}Am standard (Amersham Büchler GmbH & Co KG, Braunschweig, Germany, reference no. 9454).

For the efficiency measurements by RIMS, the samples were heated until a first signal for ^{238}Pu at around 650 °C was observed. Afterwards, a sequence was programmed in which all lasers were tuned to the resonances observed for ^{238}Pu for 120 s before the first excitation step was detuned for 5 s to record the background. The sample was heated further up during the recording of the background whenever a drop in the count rate was observed. This process was continued until the sample was no longer emitting ^{238}Pu, up to around 1200 °C. Before each measurement, the laser power and beam overlap were checked to ensure comparability and consis-

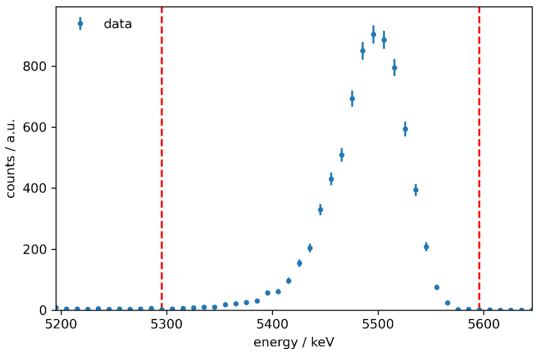

Fig. 5 α spectrum of a ^{238}Pu sample used in this work to quantify the RIMS efficiency. The red dashed lines indicate the range for which the signal was summed up. All six samples used in this work were measured 3600 s using the same Si detector. Errors are calculated from the number of events detected N via $\sigma = \sqrt{N}$

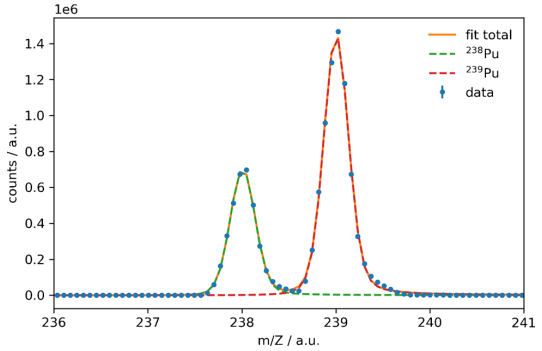

Fig. 6 Excerpt of the mass spectrum of a ^{238}Pu efficiency sample with lasers tuned to the optical transitions for ^{238}Pu using the scheme by Grüning et al. A strong signal for ^{239}Pu is observed which is near-resonantly ionized due to the width of the lasers and the broadness of its transitions. The origin of the ^{239}Pu is most likely from a contamination of the electrolysis cell or the ^{238}Pu stock solution and was not observed via α spectroscopy. Errors are calculated from the number of ions detected N via $\sigma = \sqrt{N}$. However, the error bars are too small compared to the data point symbol

tency. Laser powers during the efficiency measurements for the FES were 80 to 85 mW, the SES 400 to 600 mW, and the IS 1.1 to 1.2 W.

As displayed in Fig. 6, a strong signal of ^{239}Pu was observed in addition to ^{238}Pu indicating a contamination of either the electrolysis setup or the ^{238}Pu stock solution. ^{239}Pu was not observed via α spectroscopy of the filaments due to the lower specific activity. Due to the small isotope shift between ^{238}Pu and ^{239}Pu and the width of the Ti:Sa laser light of up to 8 GHz, ^{239}Pu is partly ionized even when the lasers are tuned to the resonances of ^{238}Pu. This was observed for both excitation schemes by Grüning et al. as well as by Galindo-Uribarri et al. Nevertheless, the mass signals are sufficiently separated in the mass analyzer, and the detection efficiency of ^{238}Pu could be determined.

As shown in Table 4, no difference in efficiency was observed between the two excitation schemes using the same setup. Variations in the absolute value for a single measurement can be attributed to slight variations in the laser power during the measurements. Here, it becomes evident that a different excitation scheme alone does not necessarily result in an increased efficiency on different RIMS setups. As already discussed for the saturation curves, due to the co-linear layout and the hot-cavity source used in [18], the total ionizing volume, as well as the atom-photon interaction and subsequent ionization probability from the Rydberg state, are much larger compared to the perpendicular laser beam geometry and sandwich type filament applied in this work. Additional factors contributing to the overall measurement efficiency are the atomization in the source as well as the total ion transmission of the MS. However, an increase of the efficiency using the scheme by Grüning et al. by a factor of ≈2-3 compared to the original measurements that were performed on the same setup in 2004 [20] was observed. This can be attributed to the higher laser powers possible by introducing the laser light directly into the source region of the mass spectrometer and not via an optical fiber, as well as the increased repetition rate of the lasers from 6.6 to 10 kHz. Another factor might be that the amount of Pu deposited on the filaments was directly quantified via α spectroscopy.

Conclusion

This work confirmed the resonance wavelengths for ^{242}Pu published by Galindo-Uribarri et al. In addition, the previously unknown isotope shifts for the isotopes ^{238}Pu, ^{239}Pu, ^{240}Pu, and ^{244}Pu for the second excitation and ionizing steps were measured. This allows now the application of this scheme for measurements of isotopic ratios of these Pu isotopes, whether for determining the isotopic fingerprint in nuclear forensic investigations or for quantifying the Pu con-

Table 4 Measured efficiencies using the three-step excitation schemes by Grüning et al. and Galindo-Uribarri et al. The amount of electrodeposited ^{238}Pu was quantified via α spectroscopy. Errors for RIMS measurement are $3 \cdot \sqrt{N} + 3 \cdot \sqrt{N_{\mathrm{BG}}}$. No difference in efficiency was observed between the two excitation schemes

Sample	^{238}Pu atoms	RIMS counts ^{238}Pu/a.u	Efficiency
Grüning et al. scheme			
I	$5.6(6) \times 10^{10}$	3,483,304(5815)	$6.2(7) \times 10^{-5}$
II	$2.8(3) \times 10^{10}$	1,654,655(3987)	$5.9(7) \times 10^{-5}$
III	$6.6(7) \times 10^{10}$	4,173,582(6385)	$6.3(7) \times 10^{-5}$
Average			$6.2(12) \times 10^{-5}$
Galindo-Uribarri et al. scheme			
IV	$4.8(5) \times 10^{10}$	2,664,358(5046)	$5.6(6) \times 10^{-5}$
V	$6.4(7) \times 10^{10}$	3,685,399(5970)	$5.8(6) \times 10^{-5}$
VI	$6.8(7) \times 10^{10}$	4,566,554(6650)	$6.7(7) \times 10^{-5}$
Average			$6.0(12) \times 10^{-5}$

tent in environmental samples with the help of an isotopic spike. It has been demonstrated that the isotopic shifts measured in this work are in the order of multiple GHz, and therefore, it is required to tune the laser wavelengths to the respective Pu isotope to ensure full ionization and correct measurements. We were not able to observe an increase in efficiency compared to the three-step excitation scheme by Grüning et al. regularly applied in routine measurements of ^{239}Pu and ^{240}Pu in environmental samples in our laboratory. Galindo-Uribarri et al. have reported a factor 4.5 higher intensity when comparing their new scheme to the three-step scheme by Raeder et al. that only differs in the IS from the one compared to in this work. It has been demonstrated that the efficiency of a Pu RIMS measurement does not only depend on the excitation scheme, but also heavily on the source region and overall setup design. Factors that have to be considered are atomization efficiency, the atom plume, the resulting laser interaction volume, laser power, and ionization pathways. The efficiency observed in this work is multiple orders of magnitude lower compared to Galindo-Uribarri et al. It has been established that setups equipped with a hot-cavity source region and co-linear laser geometry, such as the resonance ionization laser ion source (RILIS) used by Galindo-Uribarri et al., have a higher efficiency compared to a sandwich type filament source region such as the RIMS setup used in this work. Therefore, the question might arise why not to build all RIMS setups with co-linear laser geometry and a hot-cavity source. However, the source region should be designed with the application of the setup in mind. An oven-type source is at a significant disadvantage when it comes to possible contamination from previous samples and sample turn-around time, since it is required to perform a bake out after every sample or to replace the whole oven unit. This would make routine measurements of Pu isotopes in environmental samples at the ultra-trace level, as they are performed in the Nuclear Chemistry in Mainz, extremely time-consuming and increases the cost significantly. Nevertheless, future studies using a measurement setup that allows for both co-linear and perpendicular geometry of the laser beams with respect to the atom source, such as the RISIKO mass separator of the LARISSA workgroup at the Institute of Physics at the Johannes Gutenberg-Universität Mainz [22, 26], might provide further insights into the factors contributing to the efficiency of a Pu measurement via RIMS. In general, a more systematic comparison of the different excitation schemes already known for RIMS measurements of Pu, maybe even involving different measurement setups, would be of benefit. Despite not observing a difference in efficiency for the two schemes compared in this study, an overall increase in efficiency compared to the measurements performed by Grüning et al. on the same setup in the Nuclear Chemistry in Mainz was observed. This can be attributed to quantifying the exact amount Pu deposited in each electrolysis directly, the increased laser repetition rate, and introducing the laser light directly into the source region, resulting in higher laser powers.

Acknowledgements The authors would like to thank K. Wendt, M. Stemmler, R. Hasse, S. Raeder, and G. Passler for their input and feedback during fruitful discussions. Additionally, we would like to thank M. Stemmler and K. Wendt for providing the beam profiler camera. We also want to acknowledge the efforts of the three anonymous reviewers. Their very helpful questions and comments improved the manuscript.

Author contribution F. Berg: writing—original draft, writing—review and editing, visualization, methodology, conceptualization, investigation, formal analysis, project administration.
T. Reich: writing—review and editing, conceptualization, methodology, resources, supervision, project administration, funding acquisition.

Funding Open Access funding enabled and organized by Projekt DEAL. This work was funded by the Federal Ministry of Research, Technology and Space (BMFTR) under contract number 02NUK075B.

Data availability Data available at request from the corresponding author.

Declarations

Conflict of interest The authors declare no competing interests.

References

1. Oughton DH, Fifield LK, Day JP, Cresswell RC, Skipperud L, Di Tada ML, et al. Plutonium from Mayak: measurement of isotope ratios and activities using accelerator mass spectrometry. Environ Sci Technol. 2000;34(10):1938–45. https://doi.org/10.1021/es990847z.
2. Kershaw PJ, Leonard KS, McCubbin D, Aldridge JN. Plutonium: The legacy of Sellafield. In: Kudo A, editor. Plutonium in the environment. Vol. 1 of Radioactivity in the environment. Osaka, Japan: Elsevier; 2001. p. 305–328.
3. Thakur P, Khaing H, Salminen-Paatero S. Plutonium in the atmosphere: a global perspective. J Environ Radioact. 2017;175–176:39–51. https://doi.org/10.1016/j.jenvrad.2017.04.008.
4. Schramke JA, Santillan EFU, Peake RT. Plutonium oxidation states in the Waste Isolation Pilot Plant reposi-

tory. Appl Geochem. 2020;116:104561. https://doi.org/10.1016/j.apgeochem.2020.104561.
5. Geckeis H, Salbu B, Schäfer T, Zavarin M. Environmental chemistry of plutonium; 2019. Available from: https://www.osti.gov/biblio/1606477.
6. Boulyga SF, Koepf A, Konegger-Kappel S, Macsik Z, Stadelmann G. Uranium isotope analysis by MC-ICP-MS in sub-ng sized samples. J Anal At Spectrom. 2016;31:2272–84. https://doi.org/10.1039/C6JA00238B.
7. Hou X, Zhang W, Wang Y. Determination of femtogram-level plutonium isotopes in environmental and forensic samples with high-level uranium using chemical separation and ICP-MS/MS measurement. Anal Chem. 2019;91(18):11553–61. https://doi.org/10.1021/acs.analchem.9b01347.
8. Dowell SM, Barlow TS, Chenery SR, Humphrey OS, Isaboke J, Blake WH, et al. Optimisation of plutonium separations using TEVA cartridges and ICP-MS/MS analysis for applicability to large-scale studies in tropical soils. Anal Methods. 2023;15:4226–35. https://doi.org/10.1039/D3AY01030A.
9. Lee CG, Suzuki D, Esaka F, Magara M, Song K. Ultra-trace analysis of plutonium by thermal ionization mass spectrometry with a continuous heating technique without chemical separation. Talanta. 2015;141:92–6. https://doi.org/10.1016/j.talanta.2015.03.060.
10. Goswami P, Paul S, Bhushan KS, Jaison PG. Rapid and precise determination of the ^{238}Pu/^{239}Pu isotope ratio using thermal ionization mass spectrometry. J Anal At Spectrom. 2024;39:500–5007. https://doi.org/10.1039/D3JA00307H.
11. Hain K, Faestermann T, Fimiani L, Golser R, Gómez-Guzmán JM, Korschinek G, et al. Plutonium isotopes ($^{239-241}$Pu) dissolved in Pacific ocean waters detected by accelerator mass spectrometry: no effects of the Fukushima Accident observed. Environ Sci Technol. 2017;51(4):2031–7.
12. Hotchkis MAC, Child DP, Fröhlich MB, Wallner A, Wilcken K, Williams M. Actinides AMS on the VEGA accelerator. Nucl Inst Methods Phys Res Section B: Beam Interact Mater Atoms. 2019;438:70–6. https://doi.org/10.1016/j.nimb.2018.07.029.
13. Hain K, Steier P, Fröhlich MB, Golser R, Hou X, Lachner J, et al. ^{233}U/^{236}U signature allows to distinguish environmental emissions of civil nuclear industry from weapons fallout. Nat Commun. 2020;11(1):1–11. https://doi.org/10.1038/s41467-020-15008-2.
14. Nunnemann M, Erdmann N, Hasse HU, Huber G, Kratz JV, Kunz P, et al. Trace analysis of plutonium in environmental samples by resonance ionization mass spectroscopy (RIMS). J Alloys Compd. 1998;271:45–8.
15. Trautmann N, Passler G, Wendt K. Ultratrace analysis and isotope ratio measurements of long-lived radioisotopes by resonance ionization mass spectrometry (RIMS). Anal Bioanal Chem. 2004;378:348–55.
16. Schönberg P, Mokry C, Runke J, Schönenbach D, Stöbener N, Thörle-Pospiech P, et al. Application of resonance ionization mass spectrometry for ultratrace analysis of technetium. Anal Chem. 2017;89(17):9077–82.
17. Raeder S, Kneip N, Reich T, Studer D, Trautmann N, Wendt K. Recent developments in resonance ionization mass spectrometry for ultra-trace analysis of actinide elements. Radiochim Acta. 2019;107(7):645–52.
18. Galindo-Uribarri A, Liu Y, Romero Romero E, Stracener DW. High efficiency laser resonance ionization of plutonium. Sci Reports. 2021;11(1):1–11. https://doi.org/10.1038/s41598-021-01886-z.
19. Raeder S, Hakimi A, Stöbener N, Trautmann N, Wendt K. Detection of plutonium isotopes at lowest quantities using in-source resonance ionization mass spectrometry. Anal Bioanal Chem. 2012;404:2163–72.
20. Grüning C, Huber G, Klopp P, Kratz JV, Kunz P, Passler G, et al. Resonance ionization mass spectrometry for ultratrace analysis of plutonium with a new solid state laser system. Int J Mass Spectrom. 2004;235(2):171–8.
21. Köhler S, Deißenberger R, Eberhardt K, Erdmann N, Herrmann G, Huber G, et al. Determination of the first ionization potential of actinide elements by resonance ionization mass spectroscopy. Spectrochim Acta B Atomic Spectrosc. 1997;52(6):717–26. https://doi.org/10.1016/S0584-8547(96)01670-9.
22. Kaja M, Studer D, Berg F, Berndt S, Düllmann CE, Kneip N, et al. Resonant laser ionization of neptunium: investigation on excitation schemes and the first ionization potential. Eur Phys J D. 2024;78(5):1–9.
23. Schönenbach D, Berg F, Breckheimer M, Hagenlocher D, Schönberg P, Haas R, et al. Development, characterization, and first application of a resonant laser secondary neutral mass spectrometry setup for the research of plutonium in the context of long-term nuclear waste storage. Anal Bioanal Chem. 2021;413(15):3987–97.
24. Trautmann N, Folger H. Preparation of actinide targets by electrodeposition. Nuclear Instrum Methods Phys Res Section A: Accel Spectrometers Detectors Assoc Equip. 1989;282(1):102–6.
25. Liu Y, Baktash C, Beene JR, Havener CC, Krause HF, Schultz DR, et al. Time profiles of ions produced in a hot-cavity resonant ionization laser ion source. Nuclear Instrum Methods Phys Res Section B Beam Interact Mater Atoms. 2011;269(23):2771–80.
26. Kaja M, Urquiza-González M, Berg F, Reich T, Stemmler M, Studer D, et al. High-resolution laser spectroscopy on the hyperfine structure and isotope shift of ^{237,239}Np. Eur Phys J A. 2024;60(7):140.

Publication IV: Resonant laser ionization of neptunium: investigation on excitation schemes and the first ionization potential

Contribution statement

The author contributed to the following publication by preparing the required ^{237}Np and ^{239}Pu samples for this study. This involved the preparation and characterization of the respective stock solutions as well as production of the appropriate dilutions. Furthermore, he contributed to the manuscript by proof reading and editing.
Contribution statement from the publication:
Conceptualization: M.K., D.S., N.K., K.W.; Investigation: M.K., D.S., S.B., M.U.-G.; Formal analysis and Visualization: M.K.; Writing—original draft preparation: M.K.; Writing—review and editing: M.K., D.S., F.B., C.E.D., T.R., K.W.; Funding acquisition: C.E.D, T.R., K.W.; Resources: F.B.; Supervision: C.E.D, T.R., K.W.

Copyright

Eur. Phys. J. D (2024) 78:50
https://doi.org/10.1140/epjd/s10053-024-00833-7

THE EUROPEAN PHYSICAL JOURNAL D

Regular Article - Atomic Physics

Resonant laser ionization of neptunium: investigation on excitation schemes and the first ionization potential

Magdalena Kaja[1,a], Dominik Studer[2,3], Felix Berg[4], Sebastian Berndt[1,4], Christoph E. Düllmann[2,3,4], Nina Kneip[1], Tobias Reich[4], Mitzi Urquiza-González[5,6], and Klaus Wendt[1]

[1] Institute of Physics, Johannes Gutenberg University Mainz, 55099 Mainz, Germany
[2] GSI Helmholtzzentrum für Schwerionenforschung GmbH, 64291 Darmstadt, Germany
[3] Helmholtz Institute Mainz, 55099 Mainz, Germany
[4] Department of Chemistry - Nuclear Chemistry, Johannes Gutenberg University Mainz, 55099 Mainz, Germany
[5] Division Hübner Photonics, Hübner GmbH & Co. KG, 34123 Kassel, Germany
[6] Department of Physics, University of Gothenburg, 41296 Gothenburg, Sweden

Received 30 January 2024 / Accepted 20 March 2024 / Published online 4 May 2024

Abstract.
The atomic structure of neptunium (Np) was investigated by two-step resonance ionization spectroscopy. The study involved exploring ground-state transitions as well as following transitions to high-lying states just below the ionization potential (IP) or auto-ionizing states above the IP. That resulted in the identification of two-step ionization schemes, suitable for trace analysis and nuclear structure investigations. The lifetimes of two excited states located at 25,342.48 cm^{-1} and 25,277.64 cm^{-1} were determined as 230(12) ns and 173(9) ns, respectively. Because of the absence of Rydberg series in wide-ranging spectra recorded, the first IP was determined through the field ionization of high-lying, weakly-bound states using a well-controlled static electric field. By applying the saddle-point model, an IP value of 50,535.54(15) cm^{-1} [6.265608(19) eV] was derived. This value agrees with the current literature value of 50,535(2) cm^{-1}, while providing a more than ten times higher precision.

1 Introduction

Neptunium (Np), with atomic number Z = 93 is the first transuranic actinide. In the environment, only one of the twenty-five isotopes of $^{219-244}$Np known at present, is found in trace amounts, namely ^{237}Np ($t_{1/2} = 2.1 \times 10^6$ y), being created as decay products from transmutation reactions in uranium ores. However, the main source of Np isotope contamination, found today on earth and specifically in the biosphere, is fallout from nuclear weapon testing. An estimated total of about three tons of ^{237}Np has been released globally into the environment by above-ground nuclear explosions [1]. Historically, the element Np was synthesized for the first time by McMillan and Abelson in 1940 via the reaction chain

$$^{238}_{92}\mathrm{U} \xrightarrow{(n,\gamma)} {}^{239}_{92}\mathrm{U} \xrightarrow[23\ \mathrm{min}]{\beta^-} {}^{239}_{93}\mathrm{Np}, \qquad (1)$$

with ^{239}Np ($t_{1/2}$ = 2.356 d) decaying subsequently into ^{239}Pu [2]. The long-lived isotope ^{237}Np was produced one year later by Wahl and Seaborg using the reaction

$$^{238}_{92}\mathrm{U} \xrightarrow{(n,2n)} {}^{237}_{92}\mathrm{U} \xrightarrow[6.75\ \mathrm{d}]{\beta^-} {}^{237}_{93}\mathrm{Np}, \qquad (2)$$

which involves bombardment of ^{238}U with fast neutrons [3]. Today, Np is generated steadily and in macroscopic amounts within the nuclear fuel cycle with one ton of nuclear-spent fuel containing typically 500 g of ^{237}Np, corresponding to typical production rates of ∼10 kg in each conventional pressurized water reactor per year [4]. Subject to the chemical conditions within the repositories and the geological characteristics of the surrounding environment, neptunium can exist in four different oxidation states, +III to +VI, with Np(V) species exhibiting the highest mobility [5]. Thus Np represents a major hazard in the final disposal of nuclear waste due to the high radiotoxicity and the long half-life of the isotope ^{237}Np.

As a consequence, the ultra-trace analysis of Np in environmental samples is of high relevance, in particular regarding the closure and reliable sealing of long-term repositories for nuclear waste [6]. The necessary development of efficient and selective non-radiometric determination methods for Np based on the implementa-

[a] e-mail: mkaja@uni-mainz.de (corresponding author)

tion of laser ionization into mass spectrometry requires the development of efficient, easy-to-implement ionization schemes and detailed atomic spectroscopy [7]. Currently, existing ionization schemes of Np are applying sequential three- or two-step excitation induced by dye lasers [8] or require three Ti:sapphire lasers [6].

In this work, novel two-step excitation schemes in the spectral range of Ti:sapphire lasers, which turn out to be far more reliable and easier to operate than dye lasers, were investigated regarding their suitability for Np ultra-trace analysis. This reduces the complexity and susceptibility to errors of the technique in particular regarding studies on multiple isotopes or even elements. However, a reduction in the number of excitation steps involved may also negatively affect sensitivity as well as selectivity of the process, which must be examined before application.

In 1977, Fred et al. [9] measured 6069 lines of Np in the range between 4000 and 40,000 cm^{-1} with the Argonne 9 m Pashen-Runge spectrograph. They classified 130 even- and 329 odd-parity energy levels. A few years later Worden et al. [10] added 27 odd- and 37 even-parity energy levels in the range of 33,000 to 37,000 cm^{-1} to that data set. They also determined the ionization potential (IP) as 50,536(4) cm^{-1} from a dedicated study of the Rydberg series involving ionization in a pulsed electric field. Delayed application of intermittent electric field 5 μs after the populating laser pulse permitted decay of shorter-lived valence states that beforehand obscured the Rydberg series identification. The most recent value of the IP of Np was reported by Köhler et al. to be 50,535(2) cm^{-1} [11]. It was derived using three-step resonance ionization and applying the saddle-point model, which involves the ionization of highly excited atoms in a static electric field. This approach is much easier to realize and analyze without relying on the assignment of individual Rydberg series within an overwhelming multitude of other levels but has a similar precision in complex spectra to one of the Rydberg series investigations. More recently this model was also utilized by Studer et al. [12] and by Kneip et al. [13] for studies on the IP of Pm and Cm, respectively, in a rather similar context as reported here.

In this work, the investigation of the atomic structure of neptunium within the energy region around the first IP is presented. The studies include the search for strong auto-ionizing states (AI), which were addressed from three different odd-parity intermediate energy levels. As part of the process to identify efficient ionization schemes, a detailed examination of the first excited states (FES) was undertaken, focusing on line profiles and including the measurement of atomic level lifetimes. Due to the complexity of the Np spectra and the absence of easily assignable Rydberg series, a redetermination of the IP was accomplished using the electric field ionization method analogous to [12,13].

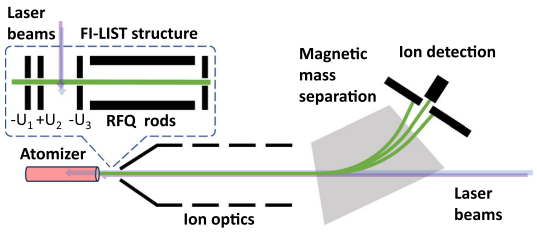

Fig. 1 Illustration of the RISIKO mass separator with ion trajectory highlighted in green and laser beams in blue and violet. The FI-LIST is an optional part and has been used only for the ionization potential measurements. Details on RISIKO specifications can be found in reference [14], and FI-LIST in [15]

2 Experimental setup

Our study employs resonance ionization spectroscopy (RIS) as a technique known for its remarkable sensitivity regarding the examination of minuscule sample amounts. Applying the stepwise photoionization process with well-tuned pulsed laser radiation also offers inherent selectivity for a specific element or even isotope. A 10 μL sample containing approximately 4×10^{13} atoms of ^{237}Np in dilute nitric acid solution was dripped onto a $4 \times 4\,mm^2$ zirconium carrier foil with a thickness of 25 µm and subsequently evaporated slowly to dryness under an infrared lamp. Accordingly, a sample containing about 2×10^{13} atoms of ^{237}Np and 2×10^{13} atoms of ^{239}Pu was prepared to test the schemes' element selectivity. The foil was folded and placed in the hot cavity atomizer of the Mainz University RISIKO mass separator and laser ion source facility, as sketched in Fig. 1. The atomizer is a 35 mm long tantalum tube with a 2.5 mm inner diameter and can be resistively heated up to about 1700 °C [14]. The ions created in the source unit are extracted and the resulting ion beam is shaped by ion optics and mass separated in a 60° sector field magnet. Ions passing a separation slit downstream of the magnet are quantitatively counted by a special channel electron multiplier (MagneTOF) detector, which ensured high detection efficiency at a very low background.

Laser ionization is normally carried out within the atomizer tube to ensure the highest efficiency in spectroscopic studies. The spectral resolution of this arrangement is limited to a few GHz linewidth by the Doppler broadening, occurring within the atomic vapor. Different ancillary devices have been developed to overcome such limitations. Based upon the Laser Ion Source Trap (LIST) [16], which comprises two electrodes, a radiofrequency quadrupole (RFQ) structure, and an exit plate, providing full suppression of background ions stemming from surface ionization on the hot cavity walls,

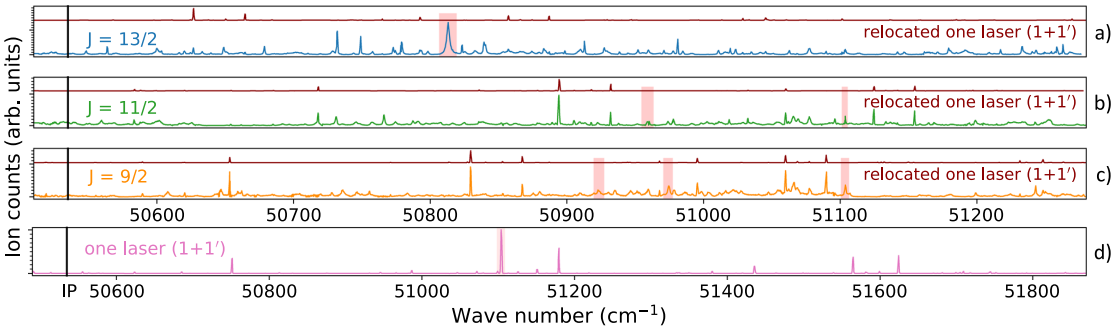

Fig. 2 Measured AI spectra above the ionization potential excited from three different first excited states: 25,075.15 cm^{-1} ($J = 13/2$) (blue graph in **a**), 25,342.48 cm^{-1} ($J = 11/2$) (green graph in **b**) and 25,277.64 cm^{-1} ($J = 9/2$) (orange in **c**) as well as a spectrum obtained by only one laser without additional first excitation step (**d**). For simple identification of resonances not stemming from the chosen FES, the latter spectrum was relocated by the energy of the respective FES and inserted in dark red color as an upper trace into each AI spectrum, as explained in the caption of Fig. 6. AI resonances studied in detail in this work are highlighted by pale red boxes

the perpendicular illuminated version PI-LIST [17,18] has been set up. By the transverse introduction of laser radiation with respect to the atom beam effusing from the atomizer cavity, high resolution is obtained for studies on hyperfine structures and isotope shifts. A further upgrade is the field ionization version, i.e., the FI-LIST [15], specifically designed for precise adjustment of an external electric field, which is needed for the determination of the ionization potential via the saddle-point model. FI-LIST is formed as a unit consisting of three electrodes in front of the regular LIST RFQ structure. At the first electrode, which is located at a distance of 0.5 mm from the cavity exit, a low negative potential is applied to repel electrons created inside the hot cavity atomizer. A second electrode following immediately has two purposes: One is to repel surface-ionized ions by a positive potential, and the second is to create a well-defined homogeneous electric field toward the third electrode, which is set on a similar but negative potential. These two electrodes are separated by exactly 10 mm distance, and the interaction region for laser radiation with the effusing atomic beam is arranged precisely in the center point of the arrangement. Created ions are directed through electrode three to enter the guiding field of the RFQ structure, which also acts as a protective shield against any influences or disturbances from the high acceleration voltage of the mass spectrometer. A detailed characterization and discussion of the performance of this FI-LIST unit can be found in [15].

Optical transitions of a two-step excitation scheme in the spectrum of the Np atom are induced by using two tunable, pulsed Ti:sapphire lasers pumped by 15 W each of a commercial, frequency-doubled Nd:YAG laser at 532.0nm with 10 kHz repetition rate. Two specific Z-shape resonator geometry types of such tunable lasers were used. These are the so-called standard Ti:sapphire of the Mainz University design, which operates with a typical pulse length of 50 ns, a spectral linewidth of 5 GHz, and up to 4 W average output power [19], but does not permit continuous long-range wavelength scans. The grating-tuned Ti:sapphire laser allows mode-hope-free tuning in the entire accessible spectral range with an output power of up to 2 W and a spectral linewidth of 2–5 GHz [20]. The tuning range of both laser types is 700–1000 nm and can be extended to 350–500 nm by a resonator-internal frequency doubling process within a beta barium borate (BBO) crystal. The fundamental frequency of each laser was measured by a commercial wavemeter (High Finesse WS6-600), with a precision of 600 MHz or 20% of the laser linewidth. Laser beams enter the RISIKO mass separator either anti-collinearly to the ion beam through the dipole magnet, or alternatively, when using the FI-LIST, both lasers are introduced into the interaction region in transversal geometry (see Fig. 1).

3 Ionization schemes

Starting from the even-parity ground state $5f^4 6d7s^2\ ^6L$ ($J = 11/2$), three different FES at 25,075.15 cm^{-1} ($J = 13/2$) (blue in Figs. 2, 3, 4, 5), 25,342.48 cm^{-1} ($J = 11/2$) (green) and 25,277.64 cm^{-1} ($J = 9/2$) (orange), were chosen for investigation of two-step excitation schemes. Unfortunately, configuration assignments of all three first excited levels are not available. To identify suitable ionization schemes into low-lying autoionizing levels, the grating-tuned laser was scanned by about 800 cm^{-1} just above the IP for all three cases as shown in the upper part of Fig. 2. During the scanning process of the second laser, a population of alternative FES occurs on occasion. Via a two-photon one-color 1 + 1' excitation including non-resonant ionization, this leads to extra peaks in the spectra, which would be incorrectly assigned and must be removed. These artifacts in the ionization spectra can be easily detected by scanning the examined range using only one

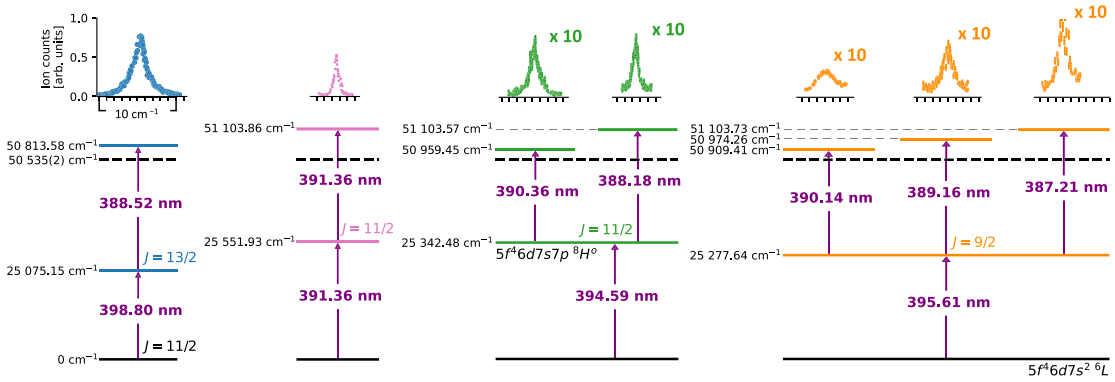

Fig. 3 Two-step excitation schemes investigated in Np. The top part is the comparison of the relative efficiencies between the different schemes. The ion counts of AI starting from the first excited states at 25,342.48 cm^{-1} and 25,277.64 cm^{-1} are magnified 10 times to visualize the shape of their profiles. The electron configurations are taken from [21] and the IP value from [11]

laser, as presented in the lowest trace of Fig. 2. Relocating this spectrum must be done by properly replacing the overall energy value. In the case of excitation with two lasers, the first-step energy is added to the scanning laser energy. In single laser excitation via 1 + 1' by just twice the second step energy gives the proper peak location and discloses these contributions for easy removal, as shown in Fig. 2 by the individual upper traces given in dark red color in each spectrum. Remarkably, 1 + 1' scan revealed a very strong two-step one-color scheme at $2 \times 25{,}551.93\,cm^{-1} = 51{,}103.86\,cm^{-1}$ (pink in Figs. 2, 3), which quasi resonantly populates an AI level at 51,103.7 cm^{-1}, found later on through two different two-step excitation schemes. In Fig. 2, the AI states marked with pale red boxes were chosen as second excited steps. These candidates were selected either according to their strength or favorable wavelength concerning the emission range of the laser. Corresponding seven investigated ionization schemes are illustrated in Fig. 3. The resonance curves and the relative efficiencies of the schemes, obtained from the ion counts measured under identical atomizer and laser power conditions, are given in the upper part of Fig. 3. In addition, a reference one-color 1 + 1' scheme was employed to subsequently adjust the data for any significant experimental variations not caused by the lasers. A list of the level positions of the five newly reported AI resonances of even parity is given in Table 1, even though no precise angular momenta or assignments can be given.

The most efficient scheme turned out to be the one starting at FES 25,075.15 cm^{-1} with $J = 13/2$, for which an efficient first-step excitation is expected by the angular momentum change of $\Delta J = +1$. This is seemingly combined with an efficient ionization channel in the second step. The scheme is approximately two times more efficient than the one-color 1 + 1' scheme and about ten times more efficient than the other schemes investigated. Two schemes, i.e., the one with a FES with $J = 13/2$ (blue in Figs. 3–5) and a FES with

Table 1 Energy levels and possible J of the investigated AI resonances presented in Fig. 3; three of them were found to be the same state

AI-No.	Energy (cm^{-1})	Possible J
1	50,813.58(20)	11/2, 13/2, 15/2
	51103.86(20)	
2	51103.57(18)	9/2, 11/2
	51103.73(26)	
3	50,959.45(18)	9/2, 11/2, 13/2
4	50,974.26(20)	7/2, 9/2, 11/2
5	50,909.41(20)	7/2, 9/2, 11/2

$J = 9/2$ and an AI at 50,909.41 cm^{-1} (orange) were explicitly proven not to be affected by an intentional plutonium admixture; when the sample with a similar amount of Np and Pu was tested, the Pu, which is much more volatile than Np or U and thus causes more background, was fully suppressed. This verification makes them perfect candidates for fundamental studies of lowest-abundance short-lived isotopes of Np as well as for trace analysis. In both cases, the occurrence of a large surplus of the neighboring elements, e.g., U or Pu must be considered. From the scans of four different first excitation steps, as presented in Fig. 4, we derive that excitations into the four intermediate levels show experimental linewidths of maximum 1.3 cm^{-1} for the J=13/2 transition, values around 1 cm^{-1} for the two J=11/2 transitions, down to 0.5 cm^{-1} for the J=9/2 transition (FWHM). Aside from a small contribution from saturation broadening, caused by a possibly slightly too high laser power chosen for one or the other of these strong transitions, this finding is ascribed to a particularly large hyperfine structure (HFS) in the excited state for J=13/2. As will be discussed in detail in a forthcoming paper [22], where we have studied this effect in the two ground-state transitions at 398.80 nm

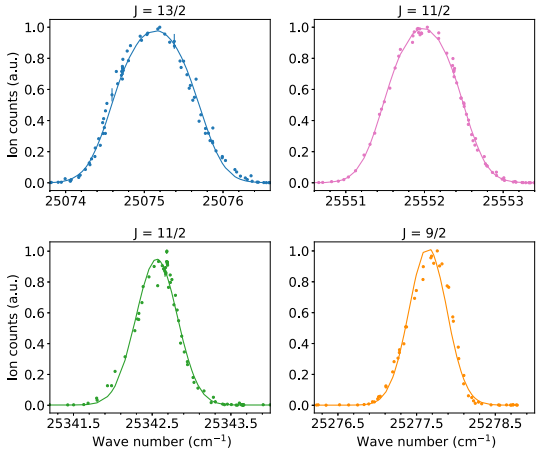

Fig. 4 Line profiles of the four first excited steps into energy levels at 25,075.15 cm^{-1} ($J = 13/2$), 25,551.93 cm^{-1} ($J = 11/2$), 25,342.48 cm^{-1} ($J = 11/2$) and 25,277.64 cm^{-1} ($J = 9/2$)

and 395.61 nm using high-resolution spectroscopy. The overall width of the HFS in the first one to the $J = 13/2$ intermediate level amounts to more than 1 cm^{-1}, while the most significantly narrower peak of the transition to the $J = 9/2$ level is caused by a HFS of less than 0.5 cm^{-1}, fully explaining the values obtained here. The experimentally determined energies of all four FES are in full agreement with the literature values from Blaise et al. [23].

Lifetimes of the FES were assessed by measuring the decay of the FES population. This was achieved by introducing a well-controlled delay between the second-step laser and the first-step laser and recording the decrease in the ion signal as a function of delay time. The corresponding temporal decay of the population in the excited state is plotted against this difference between the laser pulse settings in Fig. 5. After a start sequence, representing the rapid growth and decline of the laser pulse, it follows the expected exponential. It is important to note that, correspondingly, this method for determining lifetimes is not suitable for lifetimes significantly shorter than the laser-pulse duration ($\approx$ 50 ns). On the other hand, lifetimes longer than approx 3 μs are also inaccessible, due to the mean free path of the atoms in the source, which affects and falsifies the result [24]. Consequently, we were unable to determine the very short lifetime for the FES at 25,075.15 cm^{-1} (Fig. 5), where we only give an upper limit. The lifetimes of the FES at 25,342.48 cm^{-1} and 25,277.64 cm^{-1} were determined to be 230(12) ns and 173(9) ns, respectively. These values represent the averages obtained from measurements conducted with two distinct laser power levels of 100 mW and $\approx$ 370 mW of the first step laser to avoid any possible influences caused by saturation.

4 Ionization potential

The first attempt to determine the ionization potential of Np applied in this work involved measurements of ionization spectra in a range of about 350 cm^{-1} below the ionization potential in search of Rydberg series, which could give the IP as a convergence limit. The collected data are given in Fig. 6 in a similar way as the scans above the IP in Fig. 2, but using logarithmic intensity scaling to account for the appearance of weak peaks and structures, which might relate to Rydberg series. All the spectra show numerous resonances within a very rich and heavily complex structure of three orders of magnitude dynamical range; however, no evident pattern that could be assigned to a Rydberg series to deliver the IP was observed. In addition, by using only the scanning laser without first-step excitation, it was verified, that the majority of peaks observed relate to artifacts, caused by alternative first-step excitations with subsequent non-resonant ionization. Furthermore, correlations between remaining peaks, which could have been used for assignment of the angular momentum J, were only found in few case. Thus, no further analysis of the positions, widths, and intensities of these structures has been performed.

As a consequence, an alternative method was worked out and the IP was determined using the saddle point model, as extensively discussed by Littman et al. [25]. This approach utilizes the ionization of highly excited states just below the expected IP within a static electric field. For that purpose, the FI-LIST was installed at RISIKO, modifying the conventional laser ion source [15]. In an external field, ionization appears at a threshold W_s described by

$$W_s = \mathrm{IP} - 2\sqrt{\frac{Z_{\mathrm{eff}} e^3 F}{4\pi\epsilon_0}} \tag{3}$$

where the effective charge of the atomic core is Z_{eff}, and the external field strength is F. Equation 3 can be simplified for highly excited states, by assuming $Z_{\mathrm{eff}} = 1$, resulting in $W_s = \mathrm{IP} - 6.12(\mathrm{V}\cdot\mathrm{cm})^{-1/2}\cdot\sqrt{F}$. Hence, the IP can be determined through the precise measurement of a suitable number of field ionization thresholds W_s and extrapolation to zero-field conditions.

The scheme via the FES at 25,075.15 cm^{-1} with $J = 13/2$ was used for the field ionization measurements, as it delivered a significantly higher count rate compared to any other scheme investigated. An overview of the second-step laser scans performed in a range of about 120 cm^{-1} below up to slightly above the IP under various electric field strengths is depicted in Fig. 7, in linear y-scaling. The a) trace is obtained without any electric field. There, the ionization was induced by non-resonant processes, e.g., by black body radiation, collisions or non-resonant photons. It compares well to the relevant part of the similar spectrum shown in blue in Fig 6, measured with the conventional laser

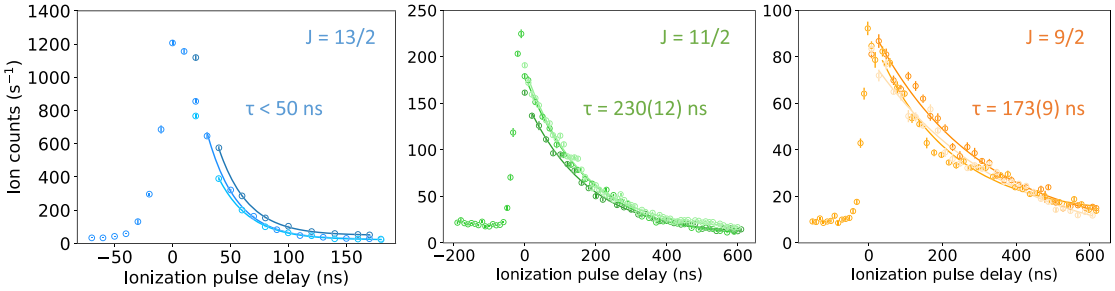

Fig. 5 Lifetime measurements for the first excited levels at: **a** 25,075.15 cm^{-1} ($J = 13/2$), **b** 25,342.48 cm^{-1} ($J = 11/2$), and c) 25,277.64 cm^{-1} ($J = 9/2$) measured with a laser power of 100 mW. The ion signal was recorded three times for each excited state to enhance statistics and later fitted with an exponential function. Additional details are provided in the text

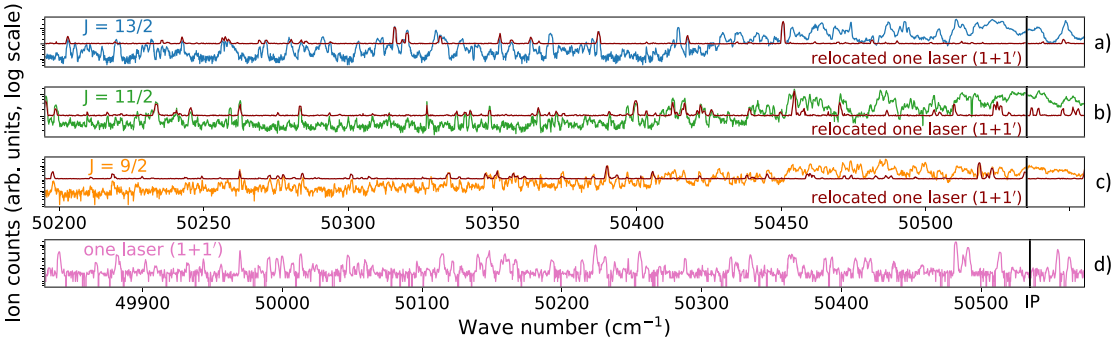

Fig. 6 Spectra of neutral neptunium acquired by scanning the second-step laser just below the IP for the three distinct FES at 25,075.15 cm^{-1} ($J = 13/2$) (blue graph in **a**), 25,342.48 cm^{-1} ($J = 11/2$) (green graph in **b**) and 25,277.64 cm^{-1} ($J = 9/2$) (orange graph in **c**). The lowest trace is a scan of a single laser (**d**), which is also indicated in dark red color as an upper trace in each spectrum beginning from different FES. The proper relocation of its energetic position as provided within the plots is achieved by dividing the scan width of the $1 + 1'$ excitation by two and adding the individual first-step energy of the respective two-step excitation. This eases the determination of artifacts in the scans. Notably, there is no noticeable presence of a Rydberg series in these spectra

ion source but exhibits somewhat reduced line intensities. For this reason, the scan was accordingly recorded at a higher atomizer temperature to increase the signal-to-background ratio. The b) trace represents resonances induced only by the second laser, which appear as artifacts in the a) spectrum too. Importantly, these resonances remain unaffected by the presence of an electric field because their excitation energy actually exceeds the IP. The c) to g) traces, given in blue color, show scans performed under different electric fields. It is evident that a higher electric field results in a shift of the ionization threshold toward lower energies. Structures lying above the ionization threshold are preserved independent of the field strengths, showing no significant influence of Stark splittings or shifts. This behavior was similarly observed in the early spectroscopic studies on actinides by Köhler and colleagues [8,11]. The same behavior was also observed in Pm [12] and it suggests the absence of strong Rydberg peaks in the spectra, which would be influenced significantly by electric fields due to their high polarizability, as observed similarly, e.g., in Yb [15].

For the investigations on the IP, we explicitly studied 12 peaks marked with green lines (see Fig. 7) in the range from 50,454 cm^{-1} to 50,526 cm^{-1} within electric fields between 2 and 184 V/cm strength. This region is significantly closer to zero field conditions and thus the IP than the one used in the studies by Köhler et al. [11], where they had to use electric field strengths as high as 60 to 340 V/cm for proper operation conditions of the used TOF mass spectrometer. This proximity to zero field reduces influences from improper systematic field determination and error contributions from an extrapolation over a wide range. As it was impossible to scan the field via addressing both electrodes involved, i.e., electrodes two and three (see Fig. 1), of the FI-LIST structure at the same time but in opposite directions, two different scans were carried out for each resonance marked in Fig. 7. Either electrode two was scanned with electrode three set onto the central value of the desired range but with opposite polarity or vice versa. An illustration for the two voltage scans for the energy level at 50,474.22 cm^{-1} is provided in Fig. 8. The data shown in Fig. 8a correspond to the scan using electrode two, while

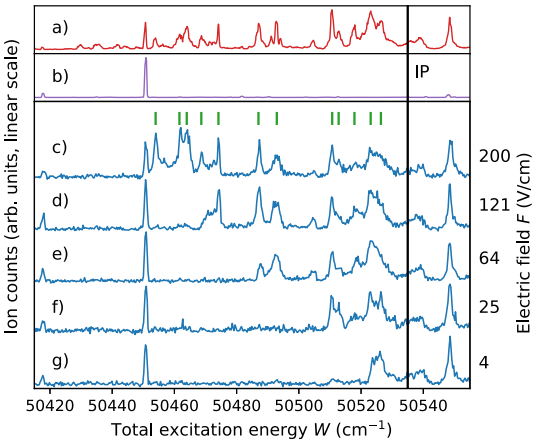

Fig. 7 Scans of the second-step laser under different conditions. The top (red) trace represents the laser scan taken without any electric field. The middle (violet) trace is the scan with a detuned first excitation step, revealing parasitic resonances. The lower traces (blue scans) represent the laser scans conducted at different electric fields F, with the corresponding electric field value indicated on the right side. The green dashes denote the peaks chosen for the detailed field scans

Fig. 8b shows the scan of electrode three, showing the good agreement among the obtained curves. In none of the twelve cases, any significant discrepancy outside the errors was observed except for a difference in the background level. This is ascribed to the background arising from electron-impact ionization, which was specifically induced by the field settings when scanning electrode two and could not be suppressed fully in the measurements. It was addressed by conducting additional measurements with detuned lasers. This allowed us to subtract any disturbing trend of this background from the data.

The measured ionization thresholds can be precisely reproduced by a sigmoid function $S(F)$, effectively capturing the convolution of the expected step function with the Gaussian profile of the peak shape

$$S(F) = A_0 + \frac{A_1}{1 + e^{-k(F-F_T)}}, \tag{4}$$

with an offset A_0, amplitude A_1, exponential coefficient k determining the width, and turning point F_T. The latter is identified as the ionization threshold for the corresponding excitation energy, following the detailed discussion and arguments given e.g. in [12]. In order to determine the IP, the parameters of W_s were evaluated as a function of $\sqrt{F}$, as presented in Fig. 9. The data points given in orange and red correspond to the scans conducted with variations of electrode two and electrode three, respectively. As pointed out above and visualized in the inlays of Fig. 9, individual data points from both scans are in perfect agreement and confirm the expected linear trend. A fit according to Eq. 3 resulted in

$$W_s^F = 50{,}535.54(15)\,\mathrm{cm}^{-1} - 6.029(9)(\mathrm{Vcm})^{-1/2} \cdot \sqrt{F}. \tag{5}$$

That indicates an IP of 50,535.54(15) cm^{-1}, which is in excellent agreement with the literature value of 50,535(2) cm^{-1} [11]. The line slope is slightly smaller than the value of 6.12 $(\mathrm{V\ cm})^{-1/2}$ expected from the saddle point model, which was also previously reported and explained when characterizing the FI-LIST [15]. This fact has already been discussed in the literature, notably in references [12,26]. It could be attributed to determining the separation distance between the electrodes defining the electric field incorrectly by about 0.1 mm. An alternative explanation attributes the finding to the Stark effect, which is not considered in the simplified saddle point model. Regardless of the origin, it is important to note that the electrode spacing solely affects the slope of the line and does not modify the y-axis intersection, which represents the IP. For all examined voltage configurations, simulations using the SIMION code [27] were performed within a ±2 mm range from the central interaction point of the ioniza-

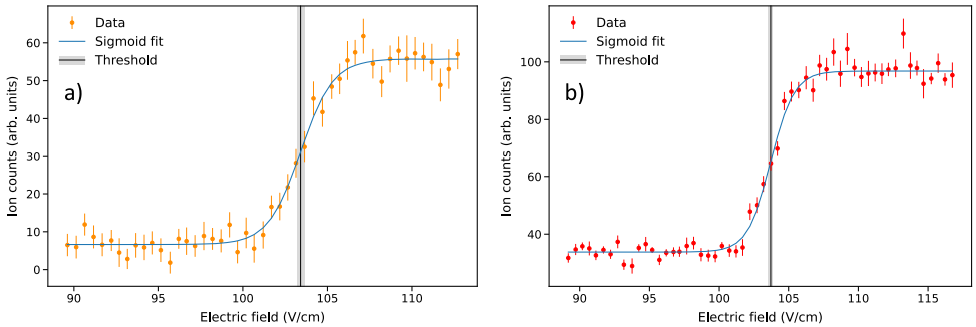

Fig. 8 Electric field ionization thresholds obtained by scanning electrode two—**a** trace and electrode three, **b** trace for the energy level at 50,474.22 cm^{-1}. For more information see the text

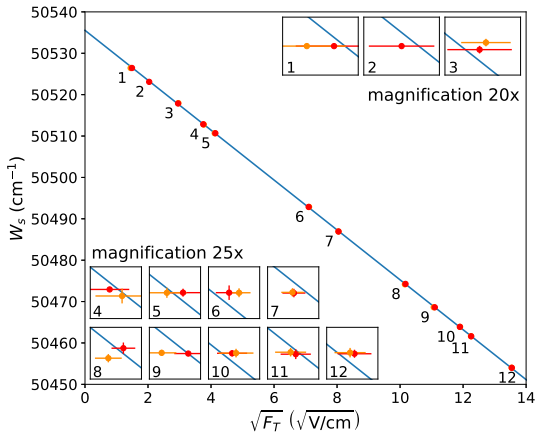

Fig. 9 Extracted ionization thresholds as a function of the square root of the electric field. The thresholds are represented by orange and red points, depending on whether the electrode two or three was scanned, respectively. The blue line corresponds to the fitted curve for all presented data. The insets display an enlarged view of the deviation between the data points and the fitted line, with a magnification factor of 20x for regions 1–3, and 25x for the others

tion region for consideration of a possible misalignment of one or both lasers or possible field disturbance by geometric effects. In all cases, the deviation between simulated electric field strength and nominal is well below 1%. It just starts to deviate for the lowest values of around 4 V/cm. Corresponding corrections are included in the presented data and errors.

5 Conclusion and outlook

Extensive studies in the atomic spectrum of neutral neptunium were carried out by two-step laser resonance ionization spectroscopy to search (i) for Rydberg and auto-ionizing levels, (ii) to determine efficient excitation schemes for fundamental investigations and trace analytics, and (iii) for a re-determination of the ionization potential. Three first-step transitions to different—J intermediate levels were investigated including the determination of their lifetimes. Scans below and above the IP were performed. Below the IP an especially rich and strongly fissured structure was found, which prevented the identification of the Rydberg series or any useful analysis of individual level positions. Based on the three first excitation steps, seven reasonably efficient ionization schemes leading above the IP, which are connected to different auto-ionizing resonances of even parity were identified and characterized. Some schemes were tested for the relative suppression of Pu and were found to be good candidates for ultra-trace analysis as well as for fundamental studies of lowest-abundance short-lived Np isotopes, i.e., regarding isotope shift or hyperfine structure measurements. The different first excitation steps were investigated in more detail by determination of their lifetimes and the line profiles.

To re-determine the IP of neptunium, the electric field ionization method based on the saddle point model was employed, yielding a value of 50,535.54(15) cm^{-1}. This result is in excellent agreement with the current literature value of 50,535(2) cm^{-1} derived by Köhler et al. [11], and represents an improvement in precision by more than an order of magnitude. The good agreement confirms the former measurements by Köhler et al. and proves that the newly developed FI-LIST source unit is a well-suited tool for IP measurements of complex and rare elements. Its application at on-line and off-line radioactive ion beam facilities, e.g., ISOLDE at CERN, and ISAC at TRIUMF, is foreseen for further IP investigation on other exotic atomic species. For future experiments, a reduction of background stemming from electron impact ionization is planned by establishing a fixed electron repeller potential relative to electrode two, for instance, setting |U1| = U2—offset, for which the optimal offset value still needs to be determined. Additionally, we could easily implement a time-gated data acquisition relative to the laser pulse, furthermore significantly reducing background from continuous surface ionization or dark counts of the detector [18]. When employing this method, it is crucial to account for ions reaching the detector earlier at higher electric fields.

Acknowledgements This work has received funding from the European Union's Horizon 2020 Research and Innovation Programme under grant agreement project number 861198 (LISA) Marie Sklodowska-Curie Innovative Training Network (ITN) and Federal Ministry of Education and Research (BMBF) under Contract Number 05P21UMFN3 and 02NUK075B (project SOLARIS).

Author contributions

Conceptualization: M.K., D.S., N.K., K.W.; Investigation: M.K., D.S., S.B., M.U.-G.; Formal analysis and Visualization: M.K.; Writing—original draft preparation: M.K.; Writing—review and editing: M.K., D.S., F.B., C.E.D., T.R., K.W.; Funding acquisition: C.E.D, T.R., K.W.; Resources: F.B.; Supervision: C.E.D, T.R., K.W..

Funding Information Open Access funding enabled and organized by Projekt DEAL.

Data Availability Statement The manuscript has no associated data in a data repository [Authors' comment: The datasets generated during and/or analyzed during the current study are available from the corresponding author on reasonable request.]

References

1. T. Beasley, J. Kelley, T. Maiti, L. Bond, J. Environ. Radioact. **38**, 133 (1998)
2. E. McMillan, P.H. Abelson, Phys. Rev. **57**, 1185 (1940)
3. A.C. Wahl, G.T. Seaborg, Phys. Rev. **73**, 940 (1948)
4. M. Krachler, R. Alvarez-Sarandes, P. Souček, P. Carbol, Microchem. J. **117**, 225 (2014)
5. P. Thakur, G. Mulholland, Appl. Radiat. Isot. **70**, 1747 (2012)
6. S. Raeder, N. Stöbener, T. Gottwald, G. Passler, T. Reich, N. Trautmann, K. Wendt, Spectrochim. Acta Part B Atomic Spectroscopy **66**, 242 (2011)
7. N. Trautmann, G. Passler, K. Wendt, Anal. Bioanal. Chem. **378**, 348 (2004)
8. J. Riegel, R. Deißenberger, G. Herrmann, S. Köhler, P. Sattelberger, N. Trautmann, H. Wendeler, F. Ames, H.J. Kluge, F. Scheerer et al., Appl. Phys. B Photophys. Laser Chem. **56**, 275 (1993)
9. M. Fred, F.S. Tomkins, J.E. Blaise, P. Camus, J. Vergès, J. Opt. Soc. Am. **67**, 7 (1977)
10. E.F. Worden, J.G. Conway, J. Opt. Soc. Am. **69**, 733 (1979)
11. S. Köhler, R. Deissenberger, K. Eberhardt, N. Erdmann, G. Herrmann, G. Huber, J.V. Kratz, M. Nunnemann, G. Passler, P.M. Rao et al., Spectrochim. Acta Part B **52**, 717 (1997)
12. D. Studer, S. Heinitz, R. Heinke, P. Naubereit, R. Dressler, C. Guerrero, U. Köster, D. Schumann, K. Wendt, Phys. Rev. A **99**, 062513 (2019)
13. N. Kneip, F. Weber, M.A. Kaja, Ch.E. Düllmann, Ch. Mokry, S. Raeder, J. Runke, D. Studer, N. Trautmann, K. Wendt, Eur. Phys. J. D **76**, 190 (2022)
14. T. Kieck, H. Dorrer, Ch.E. Düllmann, V. Gadelshin, F. Schneider, K. Wendt, Nuclear Instrum. Methods Phys. Res. Sect. A Accelerators Spectrometers Detectors Assoc. Equip. **945**, 162602 (2019)
15. M. Kaja, D. Studer, R. Heinke, T. Kieck, K. Wendt, Nucl. Instrum. Methods Phys. Res. Sect. B **547**, 165213 (2024)
16. D.A. Fink, S.D. Richter, B. Bastin, K. Blaum, R. Catherall, T.E. Cocolios, D.V. Fedorov, V.N. Fedosseev, K.T. Flanagan, L. Ghys et al., Nucl. Instrum. Methods Phys. Res. Sect. B **317**, 417 (2013)
17. R. Heinke, T. Kron, S. Raeder, T. Reich, P. Schönberg, M. Trümper, C. Weichhold, K. Wendt, Hyperfine Interact. **238**, 6 (2017)
18. R. Heinke, M. Au, C. Bernerd, K. Chrysalidis, T.E. Cocolios, V.N. Fedosseev, I. Hendriks, A.A. Jaradat, M. Kaja, T. Kieck et al., Nucl. Instrum. Methods Phys. Res. Sect. B **541**, 8 (2023)
19. S. Rothe, B.A. Marsh, C. Mattolat, V.N. Fedosseev, K. Wendt, J. Phys. Conf. Ser. **312**, 052020 (2011)
20. A. Teigelhöfer, P. Bricault, O. Chachkova, M. Gillner, J. Lassen, J.P. Lavoie, R. Li, J. Meißner, W. Neu, K.D.A. Wendt, Hyperfine Interact. **196**, 161 (2010)
21. V.V. Kazakov, V.G. Kazakov, V.S. Kovalev, O.I. Meshkov, A.S. Yatsenko, Phys. Scr. **92**, 105002 (2017)
22. M. Kaja, M. Urquiza-González, F. Berg, T. Reich, M. Stemmler, D. Studer, F. Weber, K. Wendt, Eur. Phys. J. A (manuscript submitted for publication) (2024)
23. J. Blaise, J.F. Wyart, *Constantes selectionnees niveaux d'energie et spectres atomiques des actinides* (Centre National de la Recherche Scientifique, Paris, France, 480, Paris) (1995)
24. D. Studer, L. Maske, P. Windpassinger, K. Wendt, Phys. Rev. A **98**, 042504 (2018)
25. M.G. Littman, M.M. Kash, D. Kleppner, Phys. Rev. Lett. **41**, 103 (1978)
26. F. Merkt, A. Osterwalder, R. Seiler, R. Signorell, H. Palm, H. Schmutz, R. Gunzinger, J. Phys. B Atomic Mol. Opt. Phys. **31**, 1705 (1998)
27. D.A. Dahl, *SIMION Version 8.1.1,* (computer program, Idaho National Engineering and Environmental Laboratory) (2020)

Publication V: High-resolution laser spectroscopy on the hyperfine structure and isotope shift of ^{237,239}Np

Contribution statement

The author contributed to this work by preparing the required ^{237}Np and ^{239}Np samples. This involved the production of a ^{239}Np stock solution by irradiation of ^{238}U at the TRIGA research reactor Mainz, the subsequent chemical separation via anion exchange chromatography and the characterization by γ-ray-spectroscopy. Furthermore, he contributed to the manuscript by proof reading and editing. Author contribution statement from the publication:
Conceptualization: MK, DS, FW, KW; Investigation: MK, MU-G, MS, DS, FW; formal analysis and visualization: MK; writing—original draft preparation: MK; writing—review and editing: MK, MU-G, FB, TR, DS, KW; funding acquisition: TR, KW; resources: FB; supervision: TR, KW.

Copyright

Eur. Phys. J. A (2024) 60:140
https://doi.org/10.1140/epja/s10050-024-01362-y

THE EUROPEAN PHYSICAL JOURNAL A

Regular Article - Experimental Physics

High-resolution laser spectroscopy on the hyperfine structure and isotope shift of ^{237,239}Np

Magdalena Kaja[1,a], **Mitzi Urquiza-González**[2,3], **Felix Berg**[4], **Tobias Reich**[4], **Matou Stemmler**[1], **Dominik Studer**[5,6], **Felix Weber**[1], **Klaus Wendt**[1]

[1] Institute of Physics, Johannes Gutenberg University Mainz, Mainz 55099, Germany
[2] Division Hübner Photonics, Hübner GmbH & Co. KG, Kassel 34123, Germany
[3] Department of Physics, University of Gothenburg, Gothenburg SE-41296, Sweden
[4] Department of Chemistry—Nuclear Chemistry, Johannes Gutenberg University Mainz, Mainz 55099, Germany
[5] GSI Helmholtzzentrum für Schwerionenforschung GmbH, Darmstadt 64291, Germany
[6] Helmholtz Institute Mainz, Mainz 55099, Germany

Received: 18 March 2024 / Accepted: 14 June 2024

Communicated by Klaus Blaum

Abstract Nuclear ground state properties of ^{237,239}Np were investigated by high-resolution laser spectroscopy at the RISIKO mass separator off-line radioactive beam facility of the University of Mainz. The isotope shifts and the hyperfine parameters were determined in two different atomic ground-state transitions at 398.80 nm and 395.61 nm. The data allowed for calculation of the so far unknown nuclear moments of the short-lived isotope ^{239}Np, i.e. the nuclear magnetic dipole moment of $\mu_I = +3.18(2)\,\mu_N$ and the electric quadrupole moment of $Q_S = +4.05(8)\,e$b, using the known nuclear moments of ^{237}Np as a reference, which were determined by electron paramagnetic resonance and investigations of muonic X-ray hyperfine structures, respectively.

1 Introduction

Nuclear ground state properties such as spin and electromagnetic moments as well as variations in mean square charge radii within an isotopic chain are highly relevant parameters to describe nuclear shell effects and deformations all along the nuclear chart and can serve as sensitive tests for nuclear models [1]. They can be determined with great precision using high-resolution laser spectroscopy [2]. This technique, which resolves the minor effects of hyperfine structures and isotope shifts in the optical resonance lines, has been refined in recent years towards both, remarkable precision as well as high sensitivity for studying minute sample sizes. Today, not only stable but also short-lived and exotic isotopes generated at various radioactive ion-beam facilities and nuclear reactors are accessible [1,3]. A specific region of interest for application of high-resolution laser spectroscopy is found in the range of the heaviest elements of the Periodic Table, i.e. the actinides and transactinides, where the stability of nuclear matter relies significantly on stabilizing shell effects. On the other hand, experimental data in this range of the nuclear chart, which would also validate theoretical estimates towards the description of the superheavy elements, are very scarce. Here we report on studies on the actinide element neptunium using resonance ionization mass spectrometry (RIMS). This technique has recently been adapted for high-resolution applications on rare radioisotopes [4] and has specifically been applied to actinides, both on-line [5] and off-line [6].

With an atomic number of Z = 93, neptunium is the first transuranium element. Naturally, it is occurring only in trace amounts as decay products from transmutation reactions in uranium ores. McMillan and Abelson discovered neptunium in 1939 [7] by subjecting ^{238}U to neutron bombardment. This led to the formation of the short-lived isotope ^{239}Np ($t_{1/2}$ = 2.356 d), which decays to ^{239}Pu. Two years later, the significantly longer-lived neptunium isotope ^{237}Np ($t_{1/2} = 2.1 \cdot 10^6$ y) was initially produced by Wahl and Seaborg through the bombardment of ^{238}U with fast neutrons [8]. Today, Np isotopes are a dominant by-product of the nuclear fuel cycle with the production of ~10 kg of ^{237}Np in each conventional pressurized water reactor annually [9]. Moreover, about 3 tons of ^{237}Np were released globally by mankind into the environment by above-ground nuclear detonations in the late 20th century [10]. Due to the very long half-life of ^{237}Np, it is essential to monitor nuclear waste repositories and their long-term performance specifically regarding ^{237}Np, which

[a] e-mail: mkaja@uni-mainz.de (corresponding author)

Published online: 01 July 2024

serves as an additional second motivation for the spectroscopic work described here.

The technique of RIMS, applied here for investigation of nuclear ground state properties in Np, has proven to be also suited as a sensitive and selective non-radiometric analytical technique for ultra-trace analytics in actinides and specifically ^{237}Np [11–13]. ^{239}Np could serve as a suitable tracer for precise quantification, which can be obtained as the alpha-decay daughter of ^{243}Am or alternatively from neutron irradiation of ^{238}U. However, its short half-life makes it an expensive and time-consuming option, as it has to be prepared and standardized on a weekly basis [14]. Its application in RIMS analytics thus relies on identifying ionization schemes with high elemental selectivity and the identification of isotope-related effects like hyperfine structures (HFS) and isotope shift (IS). Due to the large splittings and shifts observed in neptunium [15], unlike to most other elements, this becomes particularly important.

Already in 1977, a notable number of optical transitions in neptunium were categorized and hyperfine structure parameters for some of them were determined by Fred et al. [15]. Their experimental setup involved the analysis of a Np discharge at the 9 m Paschen-Runge spectrograph at Argonne National Laboratory together with Fourier transform spectroscopy at the Laboratoire Aime Cotton at Orsay. The precision of the HFS parameters $\mathcal{A}$ and $\mathcal{B}$ is not quoted in the paper. Considering the linewidths achieved by Fred et al. [15] of about 1 GHz, we estimated the errors to be in the order of 10 MHz for $\mathcal{A}$ and 300 MHz for $\mathcal{B}$. These estimates were obtained by fitting artificially generated data with this linewidth and suitable other parameters.

In this work, we report on two-step resonance ionization spectroscopy performed on both isotopes ^{237,239}Np. The high resolution was accomplished by using a perpendicularly illuminated laser ion source and trap (PI-LIST) unit at the off-line mass separator RISIKO of Mainz University [5, 16]. The HFS for both isotopes was studied in two different atomic ground-state transitions, which allowed for the determination of the nuclear moments of ^{239}Np and the extraction of the isotope shift between ^{237}Np and ^{239}Np in these transitions.

2 Experimental setup

Neptunium samples were prepared at the Department of Chemistry - Nuclear Chemistry, TRIGA site of the University of Mainz. ^{237}Np was available as a stock solution, while ^{239}Np was produced by irradiation of ^{238}U at the research reactor TRIGA Mark II Mainz and chemically purified through anion exchange column chromatography as described in [17]. Samples containing about 10^{13} atoms of ^{237}Np and 10^{11} atoms of ^{239}Np in nitric acid solution were deposited onto a 4 x 4 mm^2 zirconium carrier foil and evaporated slowly under an infrared lamp. As had been investigated in test measurements, Zr as a reduction agent combines optimum evaporation of Np atoms with good durability under high-temperature conditions. The folded foil was inserted into the atomizer cavity of the RISIKO mass separator ion source [18]. A simplified sketch giving the spectroscopy components of the setup up to the PI-LIST unit is presented in Fig. 1. The atomizer was resistively heated gradually up to an evaporation temperature with a maximum around 2000 °C, ensuring smooth evaporation of Np. The evaporated neutral atoms drift towards the front end of the cavity to enter the PI-LIST as an atomic beam, which is well suited for high-resolution spectroscopy. The PI-LIST has two repeller electrodes facing the atomizer and a radiofrequency quadrupole (RFQ) ion guide structure with a free field radius of 7.5 mm, a rod diameter of 10 mm, and a length of 45 mm. The repeller electrodes suppress background stemming from electrons emitted from the hot atomizer or surface ionized species. Inside the RFQ structure, the atomic beam is intersected by the beam of the spectroscopy laser entering the vacuum chamber through a window at the side of the ion source in a perpendicular geometry to substantially reduce Doppler broadening. The interaction region is located at a distance of just a few millimeters from the atomizer. To further reduce the Doppler width, the second laser beam, inducing the ionization transition is entering through a window in the mass separator magnet, in this way overlapping the atom beam in an anti-collinear manner. This configuration selects a narrow velocity class of atoms and narrows the effective opening angle within the interaction region to a minimum. A downside of this geometry is a reduction in ionization efficiency by a factor of about 100 compared to standard in-source laser ionization [16], for which this value is in the order of 10%. The ions created inside the RFQ structure are confined by the guiding RF field and transported towards the exit electrode of the PI-LIST to be accelerated to 30 keV. Subsequently, they undergo separation in the 60° sector field magnet based on their mass-to-charge ratio. In this process, adjacent masses are eliminated by a separator slit in the focal plane of the magnet. Typically a mass resolving power of $M/\Delta M \approx 600$ is realized. Finally, the ions are counted on a MagneTOF single ion detector. To further suppress background, time-resolved acquisition of the created ions was employed using a multichannel analyzer. Due to the pulsed laser ionization, the ion beam features a bunched structure with 20 μs width and 100 μs period. Counts from ions that are detected outside the expected time window are rejected, thus reducing the time-independent background by a factor of five.

Two different two-step resonant ionization schemes, labeled (A) and (B), were investigated in this work. Transition wavelengths, corresponding to the reciprocal of the wavenumber differences, are explicitly given in [19] as well as below in the text.

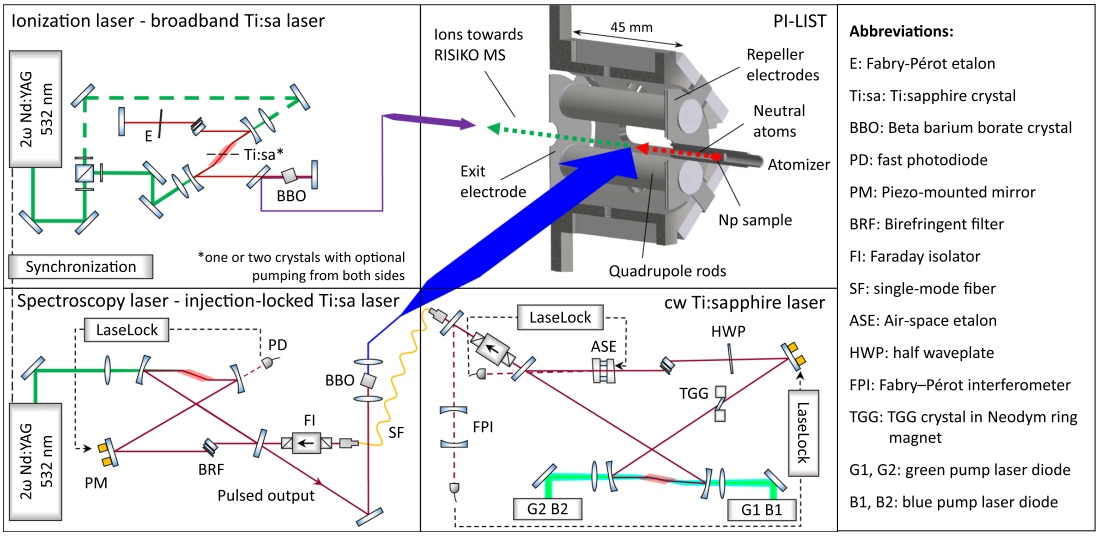

Fig. 1 Partial experimental sketch, including the pulsed broadband Ti:sapphire laser for the ionization, the pulsed injection-locked Ti:sa laser seeded by cw Ti:sapphire laser employed for spectroscopy, along with the PI-LIST ion source. Abbreviations are given in the legend on the right

(A) $0\,\mathrm{cm}^{-1} \rightarrow 25075.15\,\mathrm{cm}^{-1} \rightarrow 50813.6\,\mathrm{cm}^{-1}$
(B) $0\,\mathrm{cm}^{-1} \rightarrow 25277.64\,\mathrm{cm}^{-1} \rightarrow 50909.4\,\mathrm{cm}^{-1}$.

The ground state has an electron configuration $5f^4 6d 7s^2\ {}^6L_{11/2}$. For both first excited states, the detailed electron configuration is unknown, while the total angular momentum is known to be $J = 13/2$ for scheme (A) and $J = 9/2$ for scheme (B). The choice of the second step, in both cases leading to strong autoionizing levels just above the ionization potential of $\mathrm{IP_{Np}} = 50\,535.54(15)\ \mathrm{cm}^{-1}$ [19], took into account the presence of the daughter nuclide of ^{239}Np, i.e. ^{239}Pu, to guarantee for suitable elemental selectivity. The corresponding studies are detailed in a separate work [19]. The 398.80 nm and 395.61 nm for the first steps of schemes (A) and (B) were generated using the narrowband spectroscopy laser, namely, a pulsed injection-locked Ti:sapphire laser, arranged in a bow-tie configuration and delivering high power pulsed laser radiation with a bandwidth of about 20 MHz [20]. It was seeded by a custom-built direct diode-pumped cw Ti:sapphire laser [21,22]. To create the second harmonic, the laser light from the spectroscopy laser was focused into a BBO crystal placed outside the cavity for simple single-pass transmission. That resulted in an output power of about 100 mW. To enhance the spatial interaction volume with the effusing atomic beam, the laser beam of typical vertical height of 2 mm was expanded horizontally to approximately 2 cm in width in front of the PI-LIST, creating a large overlap area with the ionization laser beam of about 2 mm in diameter. A High Finesse WSU-30 wavelength meter was used for frequency measurements of the fundamental wavelengths. It was regularly calibrated to an ECDL, locked to the $F = 2 \rightarrow F' = 3$ transition in the D_2 line of ^{87}Rb near 780 nm via saturated absorption spectroscopy. A similar technique was used in high-resolution spectroscopy in Cf [6] and Pm [23]. The 388.52 nm for the ionizing step of the scheme (A) was generated using a standard Z-shaped Ti:sapphire laser with a spectral linewidth of 5 GHz, and a typical pulse length of 50 ns [24]. The laser light was frequency doubled by an intracavity frequency doubling process within a beta barium borate (BBO) crystal. That resulted in an output power of up to 1 W in the range of 360-400 nm. The 390.14 nm for the ionizing step of the scheme (B) was produced by a specific high-power Ti:sapphire laser equipped with two gain crystals delivering a laser power up to 3 W, while maintaining similar spectral, spatial, and temporal beam quality of a standard laser system. The lasers were pumped with 15 W, respective 30 W for the double crystal laser, of a Nd:YAG laser operating in frequency-doubled mode at 532 nm with a 10 kHz repetition rate.

3 High-resolution spectroscopy

The HFS of ^{237,239}Np and the isotope shift between these two isotopes were measured in the ground-state transitions of the two ionization schemes (A) and (B), as presented in Fig. 2. The nuclear spins of ^{237,239}Np are identical with $I = 5/2$. Because of the vector coupling of the angular momentum $\vec{J}$ of the atomic shell and this nuclear spin $\vec{I}$, according to $\vec{F} = \vec{J} + \vec{I}$, each one of the examined atomic states splits

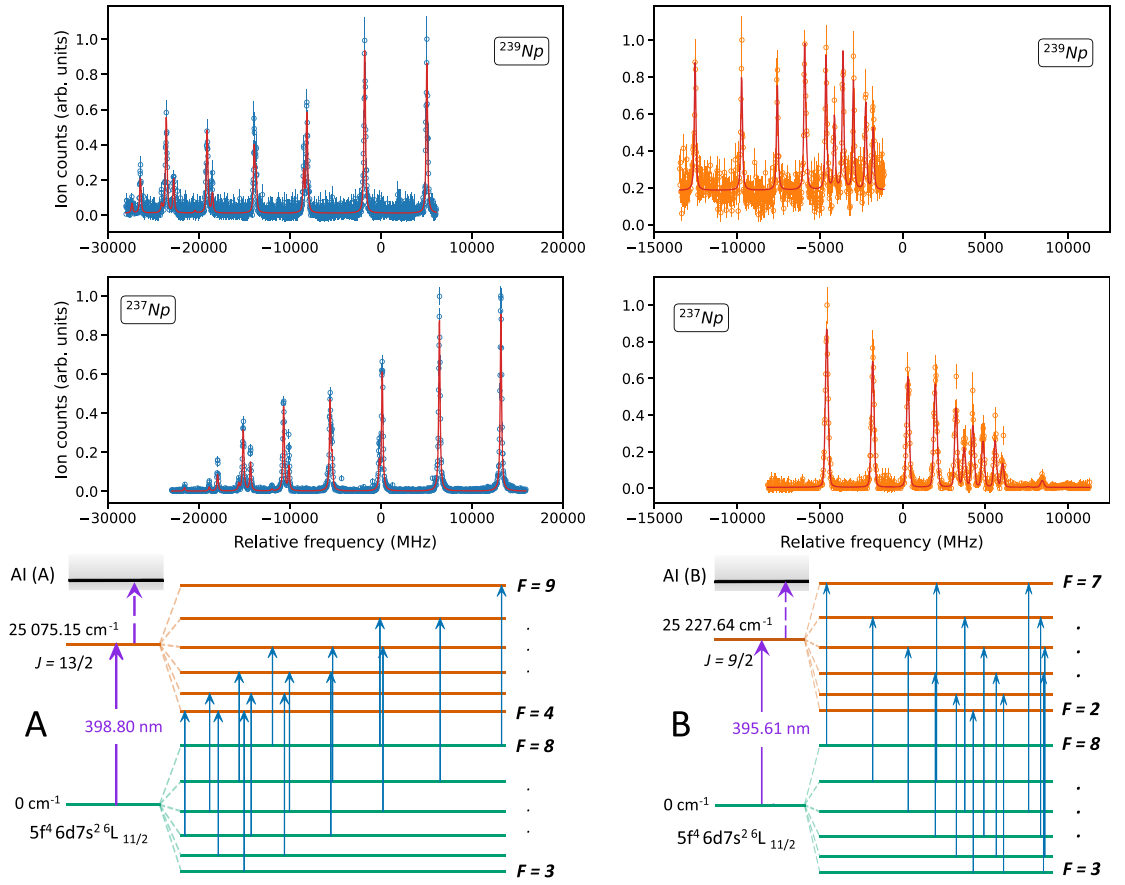

Fig. 2 Measured transitions for ^{237,239}Np. The hyperfine spectra in the ground state transition of scheme (**A**) at 399 nm on the left side and scheme (**B**) at 396 nm on the right. The hyperfine splitting of the atomic ground and respective first excited state are given below for ^{237}Np indicating the permitted hyperfine transitions by blue arrows. The Np ionization potential is $\mathrm{IP_{Np}} = 50\,535.54(15)\,\mathrm{cm}^{-1}$ [19]

into 6 HFS sub-levels with $|\ I - J\ | \leq F \leq I + J$. The energetic position of the hyperfine sub-levels is given by the HFS formula

$$\begin{aligned} \Delta E_{HFS} &= \Delta E_\mu + \Delta E_Q \\ &= \frac{\mathcal{A}C}{2} + \frac{\mathcal{B}}{4}\frac{\frac{3}{2}C(C+1) - 2I(I+1)J(J+1)}{I(2I-1)J(2J-1)}, \end{aligned} \tag{1}$$

where $C = F(F+1) - J(J+1) - I(I+1)$ [1].

This results in 15 permitted transitions between the ground and excited states, determined by the selection rules $\Delta F = 0, \pm 1$. For ^{239}Np, 10 lines were experimentally observed as well visible peaks in each scheme (A) and (B), whereas for ^{237}Np 13 and 11, respectively, were observed. The laser power of the spectroscopy laser was reduced to about 20 mW as it was tested to be a good compromise between efficiency and linewidth. The ionization laser was limited to about 450 mW to avoid background resulting from non-resonant ionization. The only exception was the measurement of ^{239}Np using scheme (B), where the laser power of the ionization laser was set to 3.5 W. This was necessary due to the slightly lower efficiency of this scheme and the limited amount of ^{239}Np in the sample. For the stronger transition at 398.80 nm in the scheme (A), a linewidth of approximately 190 MHz was recorded, whereas for the transition of 395.61 nm, it was about 120 MHz. Both linewidths could have been improved by further reducing the power in the spectroscopy laser, although this would have reduced statistics and impeded the observation of the smallest peaks.

The analysis of the spectra was performed using the SATLAS2 python package [25,26]. Line shapes were fitted with Voigt profiles and Racah coefficients were taken

Table 1 Extracted parameters for ^{237,239}Np isotopes for different atomic energy levels. The determined $\mathcal{A}_{exp}$ and $\mathcal{B}_{exp}$ parameters for ^{237}Np are compared with the previously reported values $\mathcal{A}_{lit}$ and $\mathcal{B}_{lit}$ from Ref. [15]

			^{237}Np				^{239}Np	
State	E (cm^{-1})	J	$\mathcal{A}_{exp}$	$\mathcal{B}_{exp}$	$\mathcal{A}_{lit}$	$\mathcal{B}_{lit}$	$\mathcal{A}_{exp}$	$\mathcal{B}_{exp}$
GS	0	11/2	776.08(20)	928(10)	778	645	785.59(39)	955(10)
FES$_A$	25 075.15	13/2	1470.09(18)	323(8)	1470	264	1487.43(34)	346(10)
FES$_B$	25 277.64	9/2	570.08(22)	-302(9)	–	–	577.01(47)	−311(11)

The errors of literature values were estimated by us to be in the order of 10 MHz for $\mathcal{A}$ and 300 MHz for $\mathcal{B}$ based on the 1 GHz linewidths, as discussed in the text. The HFS parameters are given in units of MHz

for initial line intensity settings. For the optimum match, the intensities were converted to free parameters after identification of the individual HFS components to account for contributions of optical hyperfine pumping and variations in the ion beam strength. The HFS parameters determined from the measured hyperfine spectra are summarized in Table 1. Three and two individual spectra per scheme were taken for ^{237}Np and ^{239}Np, respectively, and were jointly fitted with shared parameters of the ground state. The upper state parameters were also shared for the respective measurements of the same transition. A variation in the spin assignment from the expected values of 5/2 towards 3/2 or 7/2, respectively, for both isotopes was tested in the evaluation but did not lead to reasonable reproduction of either the HFS patterns or the extracted HFS parameters. Thus a nuclear spin of 5/2 was confirmed.

The obtained $\mathcal{A}$ parameters for ^{237}Np are in very good agreement with the values obtained by Fred et al. [15]. That is not the case for $\mathcal{B}$ parameters. However, a HFS simulation showed that for linewidths well above 1 GHz as accomplished by Fred et al., the finer structures of close-lying double peaks are not resolved. A simulated HFS structure with our parameters and that linewidth is almost indistinguishable from the HFS measured by Fred et al. explaining the large discrepancy in $\mathcal{B}$. Compared with each other, the HFS parameters of the ^{237,239}Np isotopes do almost not differ at all. This finding is well understood by the fact, that both isotopes share the same nuclear ground state configuration based upon the nuclear spin $I = 5/2^+$ and the similar Nilsson orbital [642]. A detailed discussion on this aspect is given in [27].

Regarding the nuclear ground state properties of Np, the nuclear moment was only known with reasonable precision for ^{237}Np so far. That nuclear magnetic dipole moment was determined using electron paramagnetic resonance to be μ_I = +3.14(4)μ_N, as recalibrated by Stone [28] from the original data of [29]. The electric quadrupole moment is Q_S = +3.886(6) eb as derived from the studies of muonic X-ray hyperfine structures [30]. With these values, the nuclear moments for ^{239}Np were determined from the extracted HFS parameters of this work using the relations

$$\mu_I = \frac{\mathcal{A}}{\mathcal{A}_{ref}} \frac{I}{I_{ref}} \mu_{I,ref} \tag{2}$$

$$Q_s = \frac{\mathcal{B}}{\mathcal{B}_{ref}} Q_{s,ref} \tag{3}$$

with ^{237}Np as reference isotope, giving μ_I = +3.18(4)μ_N and Q_S = +4.05(2) eb. The values were determined from the three individual $\mathcal{A}$ and $\mathcal{B}$ factors, respectively, using the properly weighted average. As expected, the results are almost identical to the nuclear moments of ^{237}Np, confirming the almost perfectly identical nuclear structure of both isotopes, as pointed out in [27].

Another spectroscopic parameter affected by nuclear structure is the isotope shift, which represents the frequency shift $\delta\nu$ in an atomic transition i between the two isotopes with mass numbers A and A′,

$$\delta\nu_i^{A,A'} = \nu_i^{A'} - \nu_i^{A}. \tag{4}$$

Values for the two ground state transitions studied were extracted from the measured spectra to be $\delta\nu^{237,239}_{399\,\mathrm{nm}}$ = −8 168(17) MHz and $\delta\nu^{237,239}_{396\,\mathrm{nm}}$ = −7 892(13) MHz. The lower transition frequency of ^{239}Np compared to ^{237}Np indicates that most likely an s-p transition takes place in both cases, in which the s electron is more tightly bound in the smaller nucleus, which is known to be ^{237}Np due to the almost identical nuclear moments. For very heavy nuclei with $A >$ 200 the isotope shift is predominantly caused by the change in the mean-squared charge radius $\delta\langle r^2\rangle = \delta\nu/F_{398/395}$ of the nucleus, while a mass shift effect, caused by the very small relative mass difference amounts to only a few ten MHz. The ratio is given by the electronic factor F of the corresponding atomic transition [1]. Due to the missing assignment for the two excited levels under study and, correspondingly, no suitable guess for the F-value, an extraction of the value of $\delta\langle r^2\rangle^{(237,239)}$ was not attempted. Furthermore, to our knowledge, there is no experimental or theoretical data on absolute charge radii of neptunium available. A future study, involving also additional isotopes on Np should thus aim for involving theoretical support on electronic factors as connection between atomic and nuclear parameters.

4 Conclusion and outlook

We conducted an investigation of the hyperfine spectra within two atomic ground state transitions of the neptunium isotopes ^{237}Np and ^{239}Np. This led to the precise determination of hyperfine parameters and isotope shifts. Furthermore, the magnetic dipole and electric quadrupole moments for the isotope ^{239}Np were determined with high accuracy for the first time, exhibiting a very weak and smooth development of nuclear shape. Through this work, we have laid a foundation for future high-resolution spectroscopic experiments at radioactive ion beam facilities targeting more exotic nuclei in the chain of Np isotopes and neighboring actinides, which are available only in on-line experiments. The PI-LIST ion source, which has recently undergone tests for online applications, holds promise for such studies [5]. Our findings are also valuable for RIMS measurements of neptunium contents in environmental samples by providing the necessary spectroscopic data for the prediction of line positions and hyperfine patterns from the determined nuclear moments and isotope shifts for the use of ^{239}Np as possible reference isotope for quantification.

Acknowledgements This work has received funding from the European Union's Horizon 2020 Research and Innovation Programme under grant agreement project number 861198 (LISA) Marie Sklodowska-Curie Innovative Training Network (ITN) and Federal Ministry of Education and Research (BMBF) under contract number 05P21UMFN3 and 02NUK075B (project SOLARIS).

Author contributions Conceptualization: MK, DS, FW, KW; Investigation: MK, MU-G, MS, DS, FW; formal analysis and visualization: MK; writing—original draft preparation: MK; writing—review and editing: MK, MU-G, FB, TR, DS, KW; funding acquisition: TR, KW; resources: FB; supervision: TR, KW.

Funding Open Access funding enabled and organized by Projekt DEAL.

Data Availibility Statement Data will be made available on reasonable request. [Author's comment: The datasets generated during and/or analysed during the current study are available from the corresponding author on reasonable request.]

Code Availibility Statement This manuscript has no associated code/software. [Author's comment: Code/Software sharing not applicable to this article as no code/software was generated or analysed during the current study.]

References

1. P. Campbell, I. Moore, M. Pearson, Progress Particle Nucl. Phys. **86**, 127 (2016)
2. W. Demtröder, *Laser Spectroscopy 2*, 5th edn. (Springer, Berlin, 2015). 978-3-662-44641-6
3. X. Yang, S. Wang, S. Wilkins, R.G. Ruiz, Progress Particle Nucl. Phys. **129**, 104005 (2023)
4. T. Kron, R. Beerwerth, S. Raeder, S. Fritzsche, R. Heinke, P. Schönberg, M. Trümper, K. Wendt, Phys. Rev. C **102**, 034307 (2020)
5. R. Heinke, M. Au, C. Bernerd, K. Chrysalidis, T.E. Cocolios, V.N. Fedosseev, I. Hendriks, A.A. Jaradat, M. Kaja, T. Kieck et al., Nuclear Instruments and Methods in Physics Research Section B: Beam Interactions with Materials and Atoms **541**, 8 (2023)
6. F. Weber, T.E. Albrecht-Schönzart, S.O. Allehabi, S. Berndt, M. Block, H. Dorrer, C.E. Düllmann, V.A. Dzuba, J.G. Ezold, V.V. Flambaum et al., Phys. Rev. C **107**, 034313 (2023)
7. E. McMillan, P.H. Abelson, Phys. Rev. **57**, 1185 (1940)
8. A.C. Wahl, G.T. Seaborg, Phys. Rev. **73**, 940 (1948)
9. M. Krachler, R. Alvarez-Sarandes, P. Souček, P. Carbol, Microchem. J. **117**, 225 (2014)
10. T. Beasley, J. Kelley, T. Maiti, L. Bond, J. Environ. Radioactivity **38**, 133 (1998)
11. H. Bosco, L. Hamann, N. Kneip, M. Raiwa, M. Weiss, K. Wendt, C. Walther, Science Advances **7** (2021)
12. J. Riegel, R. Deißenberger, G. Herrmann, S. Köhler, P. Sattelberger, N. Trautmann, H. Wendeler, F. Ames, H.J. Kluge, F. Scheerer et al., Appl. Phys. B Photophys. Laser Chem. **56**, 275 (1993)
13. S. Raeder, N. Stöbener, T. Gottwald, G. Passler, T. Reich, N. Trautmann, K. Wendt, Spectrochimica Acta Part B **66**, 242 (2011)
14. P. Thakur, G. Mulholland, Appl Radiation Isotopes **70**, 1747 (2012)
15. M. Fred, F.S. Tomkins, J.E. Blaise, P. Camus, J. Vergès, J Opt Soc Am **67**, 7 (1977)
16. R. Heinke, T. Kron, S. Raeder, T. Reich, P. Schönberg, M. Trümper, C. Weichhold, K. Wendt, Hyperfine Interactions **238** (2017)
17. S. Amayri, A. Jermolajev, T. Reich, Radiochimica Acta **99**, 349 (2011)
18. T. Kieck, H. Dorrer, C.E. Düllmann, V. Gadelshin, F. Schneider, K. Wendt, Nuclear Instruments and Methods in Physics Research Section A: Accelerators. Spectrometers Detectors Assoc Equipment **945**, 162602 (2019)
19. M. Kaja, D. Studer, F. Berg, S. Berndt, Ch.E. Düllmann, N. Kneip, T. Reich, M. Urquiza-González, K. Wendt, Euro Phys J D **78**, 50 (2024)
20. V. Sonnenschein, I.D. Moore, S. Raeder, M. Reponen, H. Tomita, K. Wendt, Laser Phys **27**, 085701 (2017)
21. V. Sonnenschein, H. Tomita, K. Kotaro, H. Koya, D. Studer, R. Terabayashi, F. Weber, K. Wendt, N. Nishizawa, T. Iguchi, Hyperfine Interactions **241**, 32 (2020)
22. V. Sonnenschein, M. Ohashi, H. Tomita, T. Iguchi, Nuclear Instruments and Methods in Physics Research Section B: Beam Interactions with Materials and Atoms **463**, 512 (2020)
23. D. Studer, J. Ulrich, S. Braccini, T.S. Carzaniga, R. Dressler, K. Eberhardt, R. Heinke, U. Köster, S. Raeder, K. Wendt, Euro. Phys. J. A **56**, 69 (2020)
24. S. Rothe, B.A. Marsh, C. Mattolat, V.N. Fedosseev, K. Wendt, J. Phys. **312**, 052020 (2011)
25. B. van den Borne, W. Gins, *Satlas2 – statistical analysis toolbox for laser spectroscopy, version 2*, https://iks-nm.github.io/satlas2/index.html, accessed: (2023)-10-23

26. W. Gins, R. de Groote, M. Bissell, C. Granados Buitrago, R. Ferrer, K. Lynch, G. Neyens, S. Sels, Comput. Phys. Commun. **222**, 286 (2018)
27. C. Günther, D.R. Parsignault, Nucl. Phys. A **104**, 588 (1967)
28. N. Stone, Atomic. Data Nucl. Data Tables **90**, 75 (2005)
29. W.B. Lewis, J.B. Mann, D.A. Liberman, D.T. Cromer, J. Chem. Phys. **53**, 809 (1970)
30. C. De Laat, A. Taal, W. Duinker, J. Konijn, J. Van Enschut, P. David, J. Hartfiel, H. Janszen, T. Mayer-Kuckuk, R. Von Mutius et al., Phys. Lett. B **189**, 7 (1987)

Conclusion and Outlook

This dissertation presents the development and application of the analytical techniques TOF-SIMS, RIMS and rL-SNMS for the study of (geo-)chemical interactions of Pu and Np materials in the context of long-term nuclear waste disposal in a DGR. The results have been published and included in this thesis in the form of five peer-reviewed publications, that span over a wide variety of topics and showcase the interdisciplinarity required for advancing modern analytical techniques.

Publication I describes the development and first application of rL-SNMS for the study of interactions between Pu and materials relevant for the safety case of a DGR. Based on the work of Erdmann et al. [57], the existing Ti:Sa laser system for RIMS measurements in the Nuclear Chemistry in Mainz was coupled to the commercial TOF-SIMS III and the selectivity of resonance ionization successfully applied for the post-ionization of sputtered neutral Pu from conducting and non-conducting samples. RL-SNMS was successfully used for the observation of the spatial distribution of Pu on hardened cement paste samples, as well as pyrite particles. Due to the selectivity of rL-SNMS, it was possible to isolate the Pu signal and exclude possible isobaric interferences , as well as to quantify the background of a measurement. This demonstrated the capabilities that rL-SNMS adds to traditional TOF-SIMS measurements by addressing its shortcomings.

Based on the results of publication I, in publication II the combined approach of TOF-SIMS and rL-SNMS was used for the study of the diffusion of Pu in the host rock system Opalinus Clay. Using both methods in combination, it was possible to resolve the composition of OPA at the micrometer scale and at the same time observe correlation and colocation of the minerals with Pu, therefore delivering important information about geochemical interactions. In particular, “hot spots” of Pu correlating with Fe and Ca were observed. This supports findings in literature, that identified the OPA mineral pyrite as being involved in the retention of Pu. By measuring the distribution of Pu along the interface between the sample and the Pu containing reservoir, it was possible to observe the diffusion profile of Pu in an OPA sample via TOF-SIMS and rL-SNMS. Traditionally, these profiles are accessed by abrasive peeling which not only is followed by time consuming analysis via classical radioanalytical techniques, but also destroys the sample in the process and makes it impossible to study which components of the host rock are involved in the retention. It was demonstrated that it is possible to model the diffusion profile of Pu obtained via TOF-SIMS and retrieve the apparent diffusion coefficient D_a. Such a parameter is required for the modelling of the long-term behaviour of the radioactive inventory of a DGR during its lifetime and evaluate the safety case. With a newly developed sample preparation technique that is tailored to

the strengths and weaknesses of TOF-SIMS and rL-SNMS, it is now possible to conduct diffusion studies at a larger scale and with faster turn-around times. While with abrasive peeling the retrieval of a diffusion Pu profile could take weeks, with TOF-SIMS and rL-SNMS results are available within one to two days. A custom workflow for the analysis of the TOF-SIMS and rL-SNMS datasets was developed that allows for quick analysis of diffusion profiles. Both the new diffusion setup and sample preparation technique, as well as the workflows implemented in computer codes for analysis, can be directly applied for future diffusion experiments. At the time of writing, already new experiments studying the diffusion of Np, as well as the influence of complexing organic ligands on the migration of Pu in OPA, are ongoing.

Publication III presents the results of the investigation into a novel three-step excitation scheme for RIMS and rL-SNMS measurements of Pu by Galindo-Uribarri et al. and its comparison with the three-step scheme by Grüning et al. usually applied in the Nuclear Chemistry Mainz. This involved the measurement of the previously unknown isotope shifts for the novel scheme of $^{238-240,244}$Pu, making it now possible to apply it to these isotopes and to retrieve accurate results in isotopic ratio measurements, whether for isotopic fingerprinting or the absolute quantification in environmental samples with an isotopic spike. However, during this investigation it was shown that the overall efficiency of a measurement does not only depend on the excitation scheme, but also heavily on the measurement setup. For example, it was discovered that for both schemes the last excitation step is not saturated on the RIMS setup for environmental samples and spectroscopic investigations in the Nuclear Chemistry. Therefore, not all analyte is photoionized and the efficiency and as a result the limit of detection of measurements could still be improved. This could be done by applying more laser power in this excitation step, or by testing different excitation schemes. The latter will be possible with the currently ongoing upgrade of the Ti:Sa laser system that features Ti:Sa laser with higher output powers as well as IC-SHG that will allow the application of modern two-step schemes. Additionally, the work identified pros and cons of the source region of RIMS setup. This knowledge would be a great basis for the design of a new system in the future.

Publication IV documents the development of new excitation schemes for RIMS and rL-SNMS measurements of Np as well as re-measurement of its ionization potential. This was the result of the collaborative effort between the Nuclear Chemistry and the LARISSA workgroup of the Institute of Physics at the Johannes Gutenberg-Universität Mainz to use ^{239}Np as an isotopic spike for the quantification of ^{237}Np via RIMS in environmental samples. After initial test measurements using an established three-step scheme in the Nuclear Chemistry had demonstrated the necessity for the development of more efficient excitation schemes, novel two-step schemes were developed at the RISIKO mass separator of the LARISSA workgroup. A special focus was put on the suppression of ^{239}Pu, the daughter of ^{239}Np, to allow the use of these schemes with ^{239}Np as a tracer despite its short half-life. Once the new laser system at the Nuclear Chemistry is set up, it will be possible to test

these new schemes and hopefully observe an increase in measurement efficiency. Furthermore, these schemes should also then allow to observe ^{237}Np in rL-SNMS measurements of diffusion samples. The new schemes are also a great basis for current efforts to use ^{235}Np or ^{236}Np as isotopic spikes for the quantification of ^{237}Np. Due to their longer half-life, both would be more suitable candidates as tracer compared to ^{239}Np. However, they require accelerator facilities and access to high-purity targets for their production and are not as easily available as ^{239}Np at the TRIGA research reactor Mainz. Additionally, ^{235}Np or ^{236}Np would require extensive separation to reach the purity necessary to be applied as isotopic spikes. With the new more efficient excitation schemes, the RISIKO mass separator could be used for their purification.

Publication V is the second publication that resulted from the collaborative efforts between the LARISSA workgroup and the Nuclear Chemistry. Here, the isotope shifts between ^{237}Np and ^{239}Np for the FES of two of the new two-step excitation schemes were measured. In addition, the hyperfine structure of the FES of both isotopes was investigated and literature results for ^{237}Np confirmed. For ^{239}Np, the magnetic dipole and electric quadrupole were reported for the first time. With the measurement of the isotope shift between ^{237}Np or ^{239}Np, it will be possible to use the two schemes in a new effort to use ^{239}Np as a tracer for the quantification of ^{237}Np in the Nuclear Chemistry. Furthermore, when other Np isotopes, such as ^{235}Np or ^{236}Np will be available as isotopic spikes in the future, the new and more efficient excitation schemes can be used for further investigations into the fundamental nuclear properties of Np and its isotopes.

In conclusion, this dissertation successfully showcases the application of the combined approach of TOF-SIMS and rL-SNMS for the study of Pu in the context of long-term nuclear waste disposal in a DGR and identifies the strengths and weaknesses of these techniques. Based on this work it will be possible to improve rL-SNMS measurements in the future and transfer the experiments conducted to other radionuclides, such as Np or Tc. The investigations into new excitation schemes for Pu and Np are the basis for improving rL-SNMS and RIMS measurements of these important actinides in the future, whether in the context of a DGR, for the quantification in environmental samples, fingerprinting in nuclear forensic studies or spectroscopic investigations for fundamental nuclear properties.

Appendix

Supporting information publication I

Analytical and Bioanalytical Chemistry
Electronic Supplementary Material

Development, characterization, and first application of a resonant laser secondary neutral mass spectrometry setup for the research of plutonium in the context of long-term nuclear waste storage

Daniela Schönenbach, Felix Berg, Markus Breckheimer, Daniel Hagenlocher, Pascal Schönberg, Raphael Haas, Samer Amayri, and Tobias Reich*
Department of Chemistry, Johannes Gutenberg University Mainz, 55099 Mainz, Germany
Corresponding author: Tobias Reich, Email: tobias.reich@uni-mainz.de

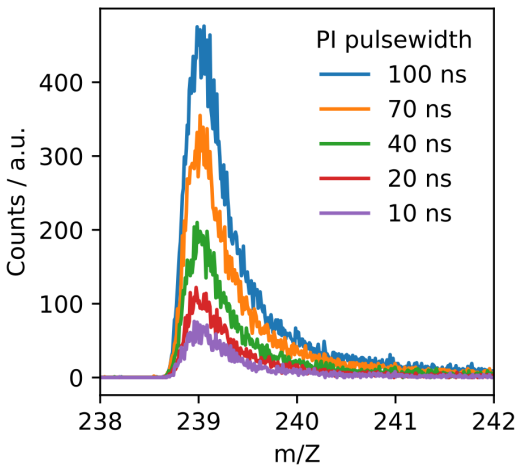

Figure S1: Laser-SNMS signal of electrodeposited ^{239}Pu on Ti foil for different primary ion (PI) pulse widths. Binning increment: 0.01

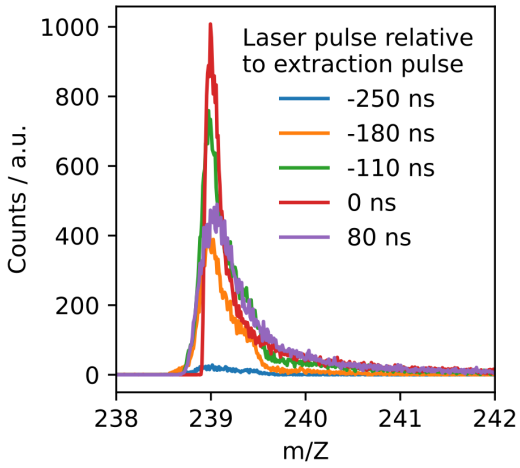

Figure S2: Laser-SNMS signal of electrodeposited ^{239}Pu on Ti foil for different laser delay timings relative to the start of the ion extraction, as observed via an external pick-up. Negative values indicate a laser pulse before the extraction. Binning increment: 0.01

Table S1: Operational parameters for the liquid metal ion gun for both secondary ion mass spectrometry and laser secondary neutral mass spectrometry at 2.5 mm distance between extractor and sample

Parameter	LMIG
Emission Current / µA	2
Energy / V	25000
Extractor / V	9000
Lens Source / V	3293
Lens Target / %	68.68
X Crossover / %	-17.3
Y Crossover / %	7.1
X Source / %	9.5
Y Source / %	-12.8

Table S2: Operational parameters for the liquid metal ion gun for both secondary ion mass spectrometry and laser secondary neutral mass spectrometry at 2.5 mm distance between extractor and sample

Parameter	Laser-SNMS; conducting	Laser-SNMS; non-conducting	SIMS
Extraction delay / ns	1650	1550	0/1165
Bias / V	+500	-40/-50	0
Analyzer energy / V	1000	1900	2000
Analyzer acceleration / V	9500	9900	9500
PI pulse width / ns	90	150	6.5-10
Laser timing / ns	-150 to 0	-85	-
Raster mode	Sawtooth	Random	Sawtooth/Random
Flood gun	No	Yes	Depending on sample

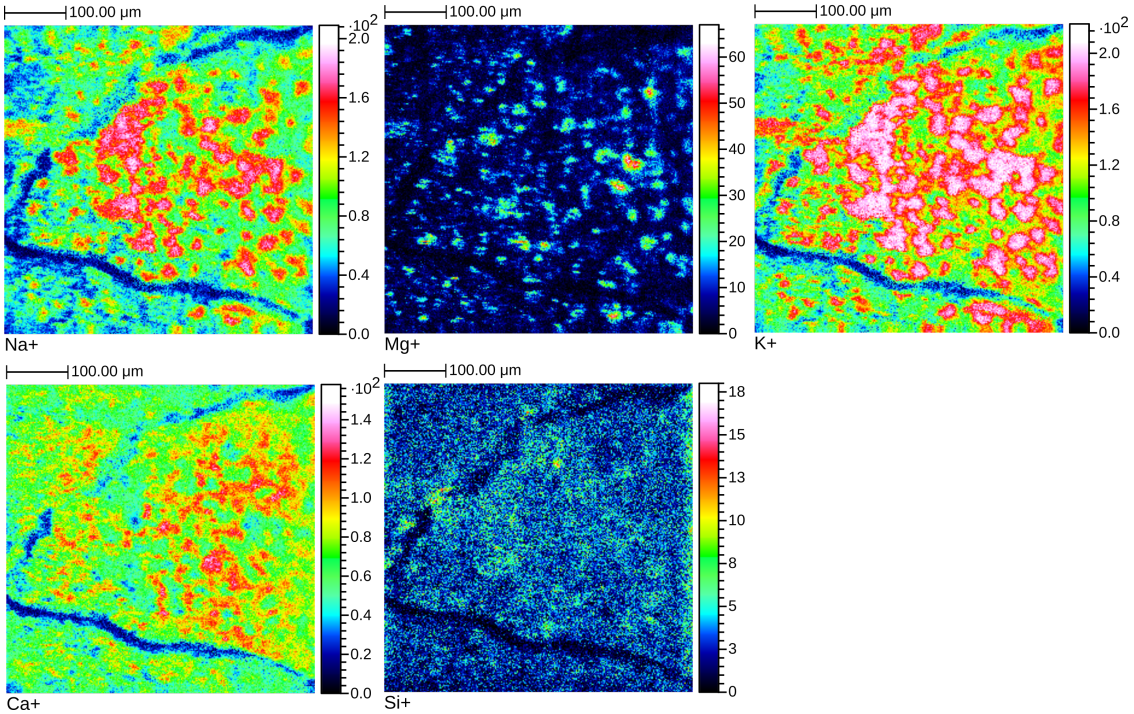

Figure S3: TOF-SIMS mass images for selected elements of the analyzed hardened cement paste thin section

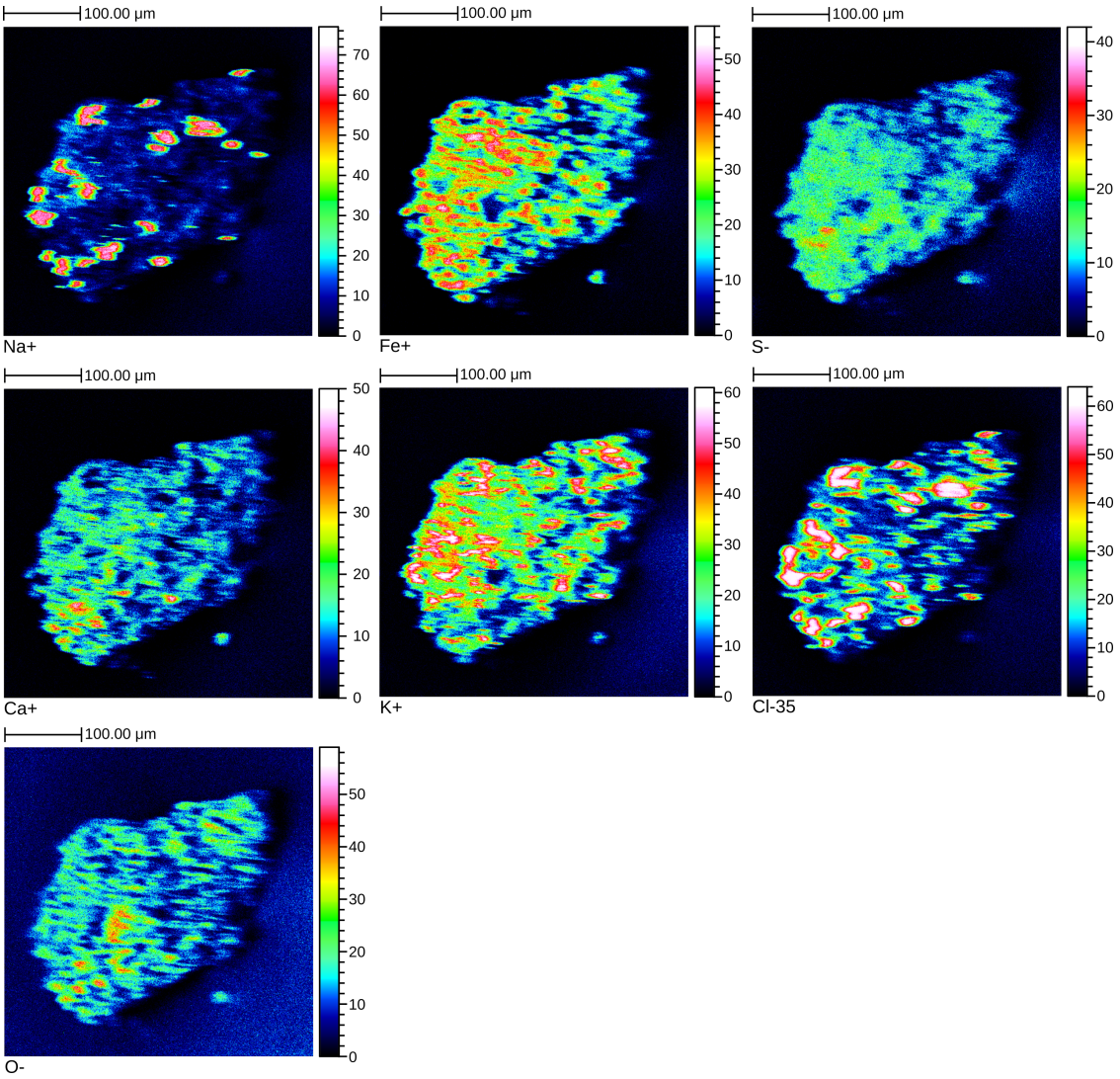

Figure S4: TOF-SIMS mass images for selected elements of the analyzed pyrite particle

Supporting information publication II

Felix Berg[a], Christopher Sirleaf[a], Janik Lohmann[a], Markus Breckheimer[a], Tobias Reich[a]
Johannes Gutenberg-Universität Mainz, Department of Chemistry - Nuclear Chemistry, 55099, Mainz, Germany

Table S1: Composition and ionic strength of OPA pore water used for the diffusion experiment. Prepared according Pearson et al. [1] without Sr^{2+} due to use for samples for XRF measurements and possible spectral interferences with the Pu signal.

Ion	concentration mol L^{-1}
Na^+	2.4×10^{-1}
K^+	1.6×10^{-3}
Mg^{2+}	1.7×10^{-2}
Ca^{2+}	2.6×10^{-2}
Cl^-	3.0×10^{-1}
SO_4^{2-}	1.4×10^{-2}
CO_3^{2-}/HCO_3^-	4.8×10^{-4}
Ionic strength	≈0.39

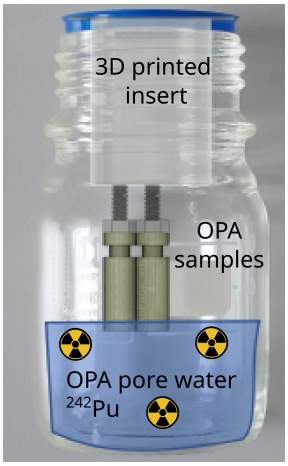

Figure S1: Schematic of the diffusion cell setup used in this study. The samples are placed in a custom designed 3D printed insert in a standard laboratory flask (100 mL laboratory bottle, narrow neck, with screw cap, VWR Interntional, Leuven, Belgium). The insert has positions for up to six samples while still allowing for pH measurement and sampling the solution.

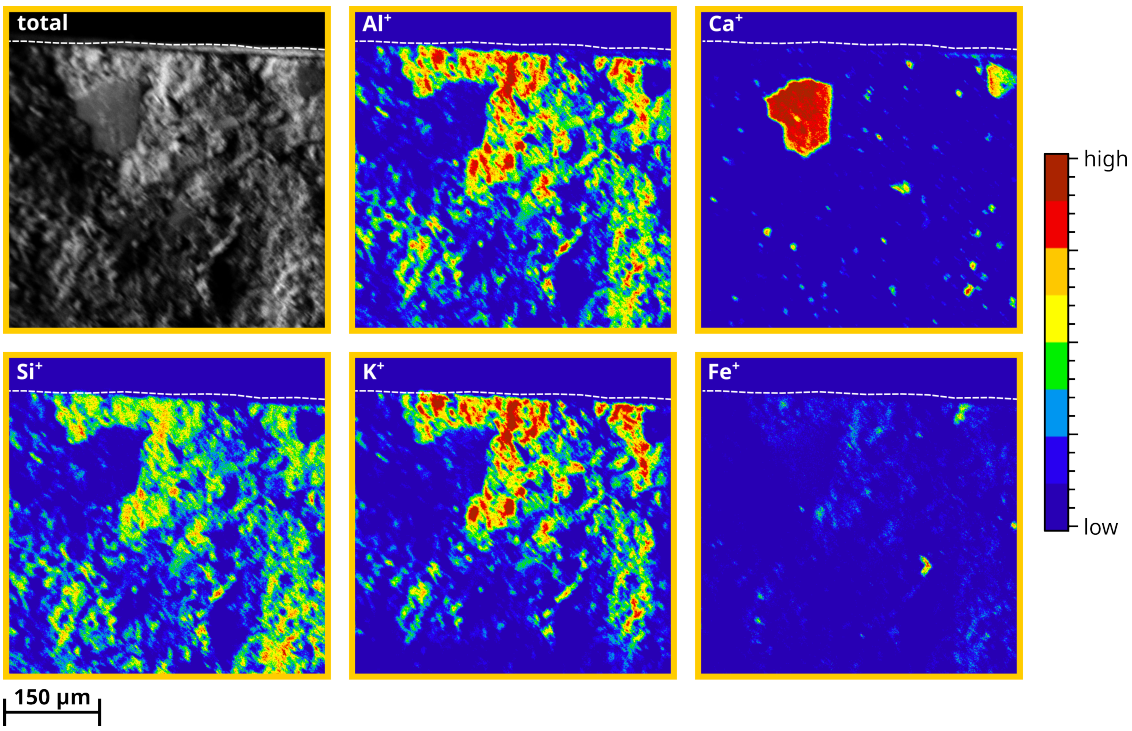

Figure S2: Distribution of various matrix elements as observed via TOF-SIMS for a OPA diffusion sample in contact with ^{242}Pu for 21 d. Al^+, Si^+ and K^+ are relatively homogeneously distributed and the overall signal intensity follows the topography of the sample. By contrast the signals for Ca^+ and Fe^+ are more localized.

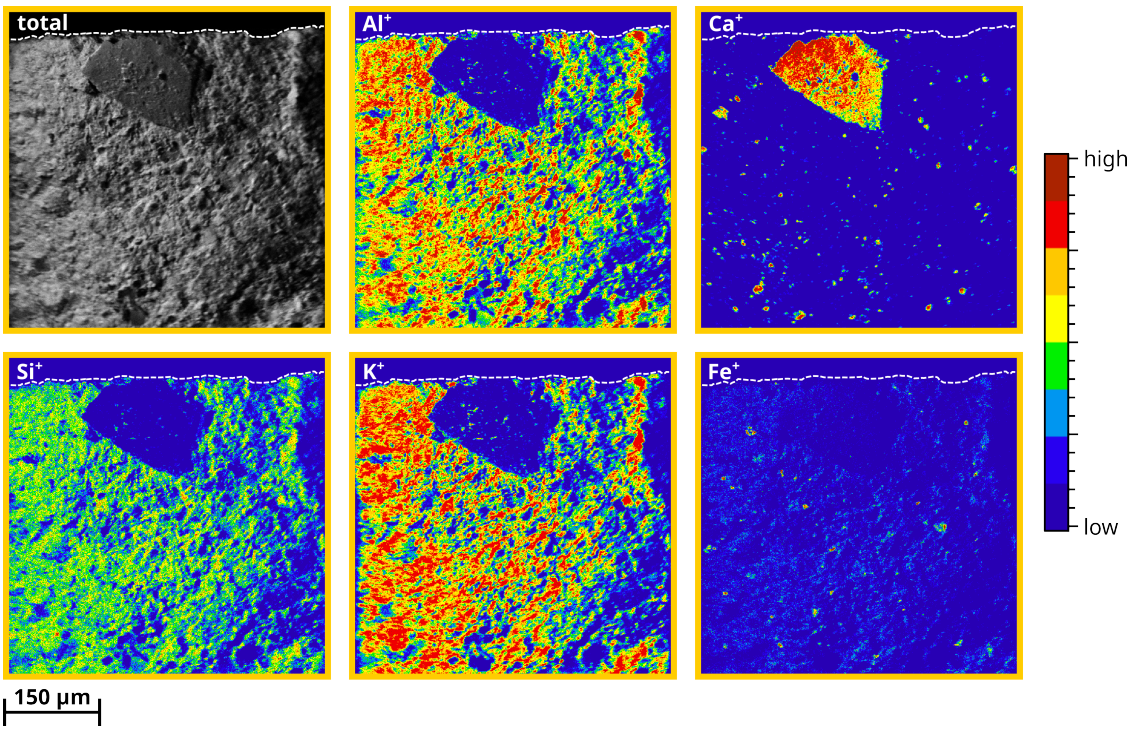

Figure S3: Distribution of various matrix elements as observed via TOF-SIMS for a OPA diffusion sample in contact with ^{242}Pu for 35 d. Al^+, Si^+ and K^+ are relatively homogeneously distributed and the overall signal intensity follows the topography of the sample. By contrast the signals for Ca^+ and Fe^+ are more localized.

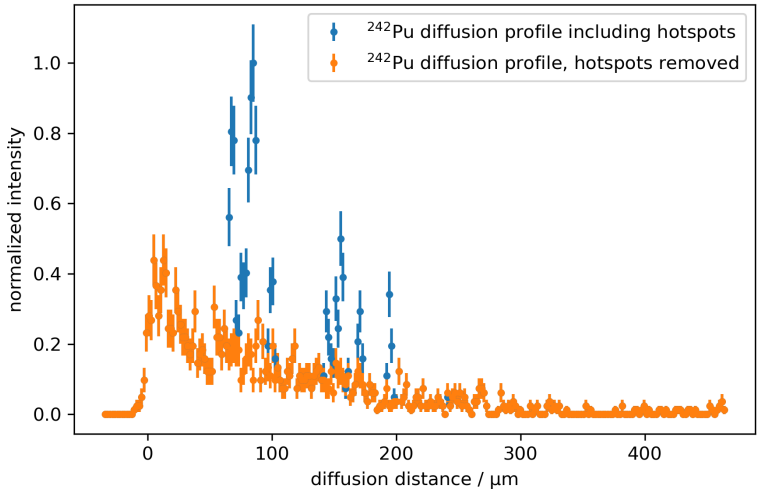

Figure S4: Comparison of a diffusion profile including and excluding 'hot spots'. The raw profile was extracted from the distribution of Pu obtained via TOF-SIMS (Pu^+ plus PuO^+) for an OPA sample after 35 d contact time. The profile was obtained by summing up the signals in each row from top to bottom in the distribution (compare Figure 5) for the respective masses. In blue, the profile includes the 'hot spots' which are the result of areas with increased intensity in the Pu distribution. For the profile shown in orange, the 'hot spots' were masked and excluded from the profile, resulting in a similar trend to profiles retrieved by abrasive peeling. The data has been binned with a binning increment of two. Errorbars are calculated as $\sigma = \sqrt{N}$ with N the number of events detected.

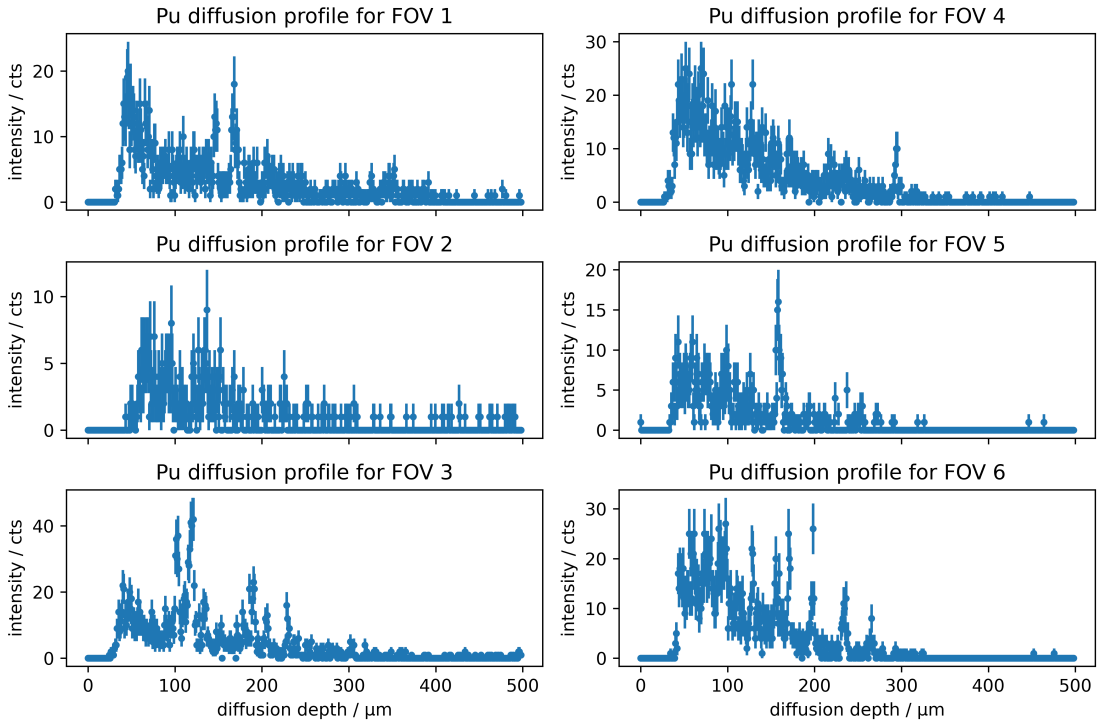

Figure S5: Overview of the six different diffusion profiles obtained from six different 500 µm^2 to 500 µm^2 field of views along the interface were the diffusion core was in contact with the Pu containing OPA-PW reservoir. Error bars are calculated as $\sigma = \sqrt{N}$ with N the number of events detected.

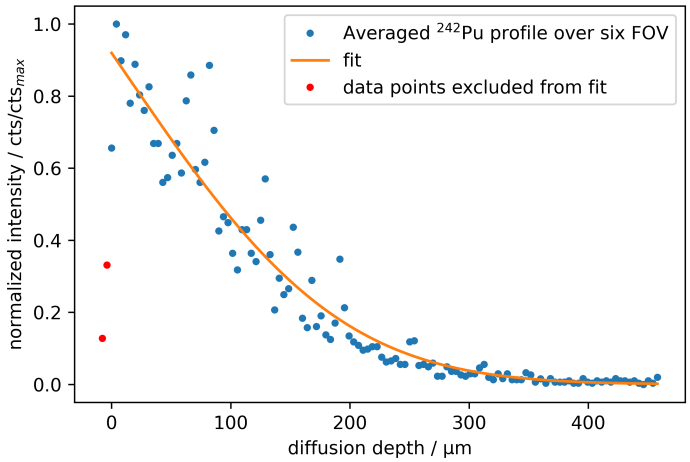

Figure S6: Fit of the averaged Pu diffusion profile for the second diffusion sample (35 d). A total of six separate 500 µm × 500 µm FOVs were measured via TOF-SIMS along the interface of the OPA diffusion core and the obtained profiles aligned and averaged. In addition, the averaged profile was binned with a binning increment of 4.

Table S2: Constants and fit parameters retrieved for the fit of an Pu diffusion profile (Figure S6) obtained by averaging over six FOVs measured by TOF-SIMS. The averaged profile was additionally binned with a binning increment of 4, which already changed the retrieved diffusion parameters D_e and α compared to the unbinned profile. However, within the margin of error, D_a is unaffected.

Parameter	Value
V / m^3	5×10^{-5}
S / m^2	1.96×10^{-5}
t / s	3 024 000
D_e / m^2 s^{-1}	$6.6(22) \times 10^{-12}$
α / -	1882(565)
D_a / m^2 s^{-1}	$3.5(16) \times 10^{-15}$

References

[1] F. Pearson, Opalinus clay experimental water: A1 Type, Version 980318, Tech. Rep. TM-44-98-07, Paul Scherrer Institut, Villigen PSI (1998).

List of Figures

Bibliography

1. IAEA. *Spent fuel and radioactive waste information system (SRIS)* Accessed 14th July 2025. Vienna. https://sris.iaea.org/home.
2. IAEA. *Status and trends in spent fuel and radioactive waste management Nuclear Energy Series* **NW-T-1.14 (Rev. 1).** ISBN: 978-92-0-130521-3. https://www.iaea.org/publications/14739/status-and-trends-in-spent-fuel-and-radioactive-waste-management (Vienna, 2022).
3. IAEA. *Power reactor information system (PRIS)* Accessed 14th July 2025. Vienna. https://pris.iaea.org/PRIS/home.aspx.
4. BGE. *Nuclear facilities in Germany "in operation"* tech. rep. Accessed 14th July 2025 (Apr. 2023). https://www.base.bund.de/SharedDocs/Downloads/BASE/EN/reports/kt/nuclear-facilities-operation.pdf.
5. BGE. *Radioactive waste - Current inventory* Accessed 14th July 2025. Bundesgesellschaft für Endlagerung. https://www.bge.de/en/radioactive-waste/current-inventory.
6. BGE. *Konrad on the home straight - Status of the completion of the repository Konrad* tech. rep. (Peine, June 2023).
7. Repository site selection act (Standortauswahlgesetz - StandAG). *Bundesgesetzblatt.* Accessed 14th July 2025, 1074–1102. http://www.bgbl.de/xaver/bgbl/start.xav?startbk=Bundesanzeiger_BGBl&jumpTo=bgbl117s1074.pdf (May 2017).
8. Krohn, J. *et al. Supporting the BASE in the process analysis of the site selection process (PaSta)* de. Tech. rep. (2024). https://www.oeko.de/fileadmin/oekodoc/pasta_abschlussbericht.pdf.
9. Judd, O. P., Davidson, J. W. & Trapp, T. J. *Evaluation of the total mass of spent fuel and plutonium generated by the U.S. and global nuclear reactors* tech. rep. LA-UR 93-0062 (Los Alamos National Laboratory, Dec. 1992).
10. Vondy, D. R., Lane, J. A. & Gresky, A. T. Production of ^{237}Np and ^{238}Pu in thermal power reactors. *Industrial & Engineering Chemistry Process Design and Development* **3,** 293–296. ISSN: 1541-5716 (Oct. 1964).
11. *Online database laser spectroscopy of radioactive isotopes - survey* Accessed 8th July 2025. https://www.ikp.tu-darmstadt.de/forschung_kernphysik/gruppen_kernphysik/experiment/ag_w_noertershaeuser/forschung_ag_w_noertershaeuser/exotische_kerne_ag_w_noertershaeuser/laserspektroskopie_uebersicht/index.en.jsp.

12. Grüning, C. *et al.* Resonance ionization mass spectrometry for ultratrace analysis of plutonium with a new solid state laser system. *International Journal of Mass Spectrometry* **235,** 171–178 (2004).
13. Thakur, P., Khaing, H. & Salminen-Paatero, S. Plutonium in the atmosphere: A global perspective. *Journal of Environmental Radioactivity,* 39–51 (Sept. 2017).
14. Hain, K. *et al.* Plutonium isotopes ($^{239\text{-}241}$Pu) dissolved in Pacific ocean waters detected by accelerator mass spectrometry: No effects of the Fukushima Accident observed. *Environmental Science & Technology* **51,** 2031–2037 (Jan. 2017).
15. Meusburger, K. *et al.* Plutonium aided reconstruction of caesium atmospheric fallout in European topsoils. *Scientific Reports* **10.** ISSN: 2045-2322 (July 2020).
16. Schönberg, P. *et al.* Application of resonance ionization mass spectrometry for ultratrace analysis of technetium. *Analytical Chemistry* **89,** 9077–9082 (July 2017).
17. Galindo-Uribarri, A., Liu, Y., Romero Romero, E. & Stracener, D. W. High efficiency laser resonance ionization of plutonium. *Scientific Reports* **11,** 1–11. ISSN: 2045-2322 (Dec. 2021).
18. Berg, F. & Reich, T. Investigating a novel three-step excitation scheme for the ultra-trace analysis of plutonium via RIMS. *Analytical and Bioanalytical Chemistry* (Aug. 2025).
19. Bellido, L. F., Robinson, V. J. & Sims, H. E. Production of ^{235}Np and ^{236}Pu for environmental applications. *Radiochimica Acta* **64,** 11–14 (Jan. 1994).
20. Dmittiev, S. *et al.* High-purity radionuclide production: material, construction, target chemistry for ^{26}Al, ^{97}Ru, ^{178}W, ^{235}Np, ^{236,237}Pu. *Nuclear Instruments and Methods in Physics Research Section A: Accelerators, Spectrometers, Detectors and Associated Equipment* **397,** 125–130. ISSN: 0168-9002 (Sept. 1997).
21. Raeder, S. *et al.* Determination of a three-step excitation and ionization scheme for resonance ionization and ultratrace analysis of ^{237}Np. *Spectrochimica Acta part B: Atomic Spectroscopy* **66,** 242–247 (Feb. 2011).
22. Stöbener, N. *Element speciation of neptunium in the ultra-trace regime* PhD thesis (Johannes Gutenberg-Universität Mainz, 2013).
23. Holz, B. *Laserspectroscopic investigations of ^{237}Np and ^{239}Np* MA thesis (Technische Hochschule Mittelhessen Campus Gießen, Aug. 2020).
24. Nagra. *The site for the deep geological repository - Nagra's proposal* tech. rep. (Sept. 2022).
25. NEA. *Clay Club Catalogue of Characteristics of Argillaceous Rocks* tech. rep. (Paris, 2022).

26. NEA. *Self-sealing of fractures in argillaceous formations in the context of geological disposal of radioactive waste* tech. rep. (Paris, 2010).
27. Kneuker, T., Dohrmann, R. & Jaeggi, D. Compositional-structural characterization of the Opalinus Clay and Passwang Formation: New insights from Rietveld refinement (Mont Terri URL, Switzerland). *Applied Clay Science* **242** (Sept. 2023).
28. Nagra. *Project Opalinuston - Synthesis of the geoscientific results* tech. rep. NTB 02-03 (Wettingen, Dec. 2002).
29. Berg, F., Sirleaf, C., Lohmann, J., Breckheimer, M. & Reich, T. Investigation of plutonium diffusion profiles in Opalinus Clay rock via TOF-SIMS and rL-SNMS. *Applied Geochemistry* **183,** 106332 (Mar. 2025).
30. Pearson, F. *et al.* Mont Terri project-Geochemistry of water in the Opalinus Clay formation at the Mont Terri Rock Laboratory. *Berichte des BWG, Serie Geologie* **5** (2003).
31. Pearson, F. *Opalinus Clay experimental water: A1 Type, Version 980318* tech. rep. TM-44-98-07 (Paul Scherrer Institut, Villigen PSI, 1998).
32. LLC, A. S. *The Geochemist's Workbench Community Edition* `https://community.gwb.com`.
33. Madé, B. *et al.* Recent developments in ThermoChimie–A thermodynamic database used in radioactive waste management. *Applied Geochemistry* **180,** 106273 (Jan. 2025).
34. Wu, T., Amayri, S., Drebert, J., van Loon, L. R. & Reich, T. Neptunium(V) sorption and diffusion in Opalinus Clay. *Environmental Science & Technology* **43,** 6567–6571 (July 2009).
35. Joseph, C., Schmeide, K. & Bernhard, G. Sorption of uranium(VI) onto Opalinus Clay in the absence and presence of humic acid in Opalinus Clay pore water. *Chemical Geology* **284,** 240–250 (May 2011).
36. Joseph, C. *et al.* Diffusion of U(VI) in Opalinus Clay: Influence of temperature and humic acid. *Geochimica et Cosmochimica Acta* **109,** 74–89. ISSN: 0016-7037 (Feb. 2013).
37. Kautenburger, R., Brix, K. & Hein, C. Insights into the retention behaviour of europium(III) and uranium(VI) onto Opalinus Clay influenced by pore water composition, temperature, pH and organic compounds. *Applied Geochemistry* **109,** 104404. ISSN: 0883-2927 (Aug. 2019).
38. Maes, N. *et al.* EURAD state-of-the-art report on the understanding of radionuclide retention and transport in clay and crystalline rocks. *Frontiers in Nuclear Engineering* **3,** 1417827 (Nov. 2024).

39. Kaplan, U., Amayri, S., Drebert, J., Grolimund, D. & Reich, T. Plutonium mobility and reactivity in a heterogeneous clay rock barrier accented by synchrotron-based microscopic chemical imaging. *Scientific Reports* **14,** 1–11. ISSN: 2045-2322 (Feb. 2024).

40. Fröhlich, D. *et al.* Speciation of Np(V) uptake by Opalinus Clay using synchrotron microbeam techniques. *Analytical and Bioanalytical Chemistry* **404,** 2151–2162 (Aug. 2012).

41. Wigger, C. & Van Loon, L. R. Importance of interlayer equivalent pores for anion diffusion in clay-rich sedimentary rocks. *Environmental Science & Technology* **51,** 1998–2006. ISSN: 1520-5851 (Feb. 2017).

42. Glaus, M. *et al.* Cation diffusion in the electrical double layer enhances the mass transfer rates for Sr^{2+}, Co^{2+} and Zn^{2+} in compacted illite. *Geochimica et Cosmochimica Acta* **165,** 376–388. ISSN: 0016-7037 (Sept. 2015).

43. Yaroshchuk, A. E. & Van Loon, L. R. Improved interpretation of in-diffusion measurements with confined swelling clays. *Journal of Contaminant Hydrology* **97,** 67–74 (Jan. 2008).

44. Schönenbach, D. *et al.* Development, characterization, and first application of a resonant laser secondary neutral mass spectrometry setup for the research of plutonium in the context of long-term nuclear waste storage. *Analytical and Bioanalytical Chemistry* **413,** 3987–3997 (May 2021).

45. Kaja, M. *et al.* Resonant laser ionization of neptunium: investigation on excitation schemes and the first ionization potential. *The European Physical Journal D* **78,** 1–9. ISSN: 1434-6079 (May 2024).

46. Studer, D. *Probing atomic and nuclear structure properties of promethium by laser spectroscopy* PhD thesis (Johannes Gutenberg-Universität Mainz, June 2020).

47. A. Kramida, Yu. Ralchenko, J. Reader & NIST ASD Team. NIST Atomic Spectra Database (ver. 5.12), [Online]. Available: https://physics.nist.gov/asd, Accessed 2025, July 10th. National Institute of Standards and Technology, Gaithersburg, MD. 2024.

48. Kneip, N. *et al.* Highly selective two-step laser ionization schemes for the analysis of actinide mixtures. *Hyperfine Interactions* **241,** 1–7. ISSN: 1572-9540 (Mar. 2020).

49. Berg, F. *Characteriziation and application of laser-SNMS for the analysis of plutonium* diploma thesis. 2018.

50. Schönberg, P. *Setup and characterization of a laser-SNMS system for the spatially resolved ultra-trace analysis of radionuclides in the environment* PhD thesis (Johannes Gutenberg-Universität Mainz, 2020).

51. Schönenbach, D. *Spatially resolved ultra-trace analysis via secondary ion mass spectrometry and laser-secondary neutral mass spectrometry* PhD thesis (Johannes Gutenberg-Universität Mainz, 2020).

52. Sigmund, P. in *Sputtering by Particle Bombardment I* (ed Behrisch, R.) 284 (Springer, Berlin, Heidelberg, 1981). ISBN: 978-3-540-38514-1.

53. Benninghoven, A., Hagenhoff, B. & Niehuis, E. Surface MS: probing real-world samples. *Analytical chemistry* **65,** 630A–640A (July 1993).

54. Muramoto, S. *et al.* ToF-SIMS Analysis of adsorbed proteins: Principal component analysis of the primary ion species effect on the protein fragmentation patterns. *The Journal of Physical Chemistry C* **115,** 24247–24255. ISSN: 1932-7455 (Nov. 2011).

55. Shon, H. K., Yoon, S., Moon, J. H. & Lee, T. G. Improved mass resolution and mass accuracy in TOF-SIMS spectra and images using argon gas cluster ion beams. *Biointerphases* **11,** 02A321. ISSN: 1934-8630 (Feb. 2016).

56. Sämfors, S., Ewing, A. G. & Fletcher, J. S. Benefits of NaCl addition for time-of-flight secondary ion mass spectrometry analysis including the discrimination of diacylglyceride and triacylglyceride ions. *Rapid Communications in Mass Spectrometry* **32,** 1473–1480. ISSN: 1097-0231 (July 2018).

57. Erdmann, N., Kratz, J.-V., Trautmann, N. & Passler, G. Resonance ionization mass spectrometry of ion beam sputtered neutrals for element- and isotope-selective analysis of plutonium in micro-particles. *Anal Bioanal Chem* **395,** 1911–1918 (Nov. 2009).

58. Bosco, H. *et al.* New horizons in microparticle forensics: Actinide imaging and detection of ^{238}Pu and ^{242m}Am in hot particles. *Science Advances* **7,** eabj1175 (Oct. 2021).